



**VIBRATION ANALYSIS OF COMMERCIAL
THERMAL BARRIER COATINGS**

THESIS

Lindell E. Pearson, Captain, USAF

AFIT/GAE/ENY/08-J05

**DEPARTMENT OF THE AIR FORCE
AIR UNIVERSITY**

AIR FORCE INSTITUTE OF TECHNOLOGY

Wright-Patterson Air Force Base, Ohio

APPROVED FOR PUBLIC RELEASE; DISTRIBUTION UNLIMITED

The views expressed in this thesis are those of the author and do not reflect the official policy or position of the United States Air Force, Department of Defense, or the United States Government.

AFIT/GAE/ENY/08-J05

VIBRATION ANALYSIS OF COMMERCIAL THERMAL
BARRIER COATINGS

THESIS

Presented to the Faculty

Department of Aeronautics and Astronautics

Graduate School of Engineering and Management

Air Force Institute of Technology

Air University

Air Education and Training Command

In Partial Fulfillment of the Requirements for the

Degree of Master of Science

Lindell E. Pearson, BS

Captain, USAF

June 2008

APPROVED FOR PUBLIC RELEASE; DISTRIBUTION UNLIMITED

Abstract

Thermal barrier coatings (TBCs) are currently used in turbine engine components to protect substrate material from being exposed to high temperatures and corrosion. These coatings also have the potential to reduce stress in critical engine parts which could increase the life cycle of these parts. The fact that these coatings are already qualified for use in turbine engines makes it worth investigating their damping properties. The problem with TBCs is that they are difficult to characterize as they display nonlinear properties. This research utilizes an experimental and finite element procedure to characterize these coatings. A scanning electron microscope (SEM) was also employed to observe the microstructure contribution to the damping properties.

This program utilizes a testing method which employs a test setup that attempts to eliminate any external factors which may add any unwanted damping. The major contributions of this research are: a comparison of the material properties of two different thermal barrier coatings, magnesium aluminate spinel and yttria stabilized zirconia; the confirmation that sweep rate does not cause data recorded in the log decrement method to coincide with data recorded with the half-power bandwidth method; and SEM images that confirm the damping properties of plasma sprayed thermal barrier coatings are directly related to the crack structure of a coating on a microstructural level.

To my wife, thank you so much.

Acknowledgments

There are several people who have helped me in creating this body of work. They have taught me how to look at things in new ways and helped me grow as an engineer. I first have to thank my advisor, Dr. Anthony Palazotto. He has guided me every step of the way, helped me out of some bad situations and has inspired me with his endless enthusiasm. I also have to thank Major Shad Reed. There was never a question he wouldn't answer, a meeting he couldn't attend or a minute he couldn't spare. He spent several hours guiding me through the experimental and computational process.

The experimental part of this research was conducted entirely at the Turbine Engine Fatigue Facility at the Air Force Research Laboratory. The success of this research would not have been possible without the individuals at that lab. Specifically, I would like to thank Dr. Tommy George, Lt Josh Mark and Mr. Brian Runyon. Lt Mark brought me up to speed on the VibrationVIEW software that was so important in this research. Another individual involved in this research who provided invaluable assistance is Mr. John Justice. He answered any and all questions I had regarding testing.

Finally, I would like to thank Dr. Andy Rosenberger, Dr. Mike Cinibulk, Mr. Scott Apt and Mr. Kevin Shiveley at the Materials and Manufacturing Directorate of the Air Force Research Lab. The knowledge and professionalism these individuals displayed was truly outstanding. I wouldn't have captured one reliable SEM image without their help and guidance.

Lindell E. Pearson

Table of Contents

	Page
Abstract.....	iv
Dedication.....	v
Acknowledgments.....	vi
List of Figures.....	ix
List of Tables.....	xiv
I. Introduction.....	15
Fatigue.....	15
Damping.....	16
Hard Coatings.....	17
Application.....	18
Plasma Spray.....	18
Electron Beam Evaporation—Physical Vapor Deposition (EB-PVD).....	19
Microstructure.....	20
Bond Coat.....	23
Characterization.....	24
Frequency Domain Technique.....	24
Air Damping.....	28
Boundary Conditions.....	28
Finite Element.....	31
Objective.....	31
II. Experimental Technique and Setup.....	33
Setup.....	33
Specimens.....	40
Experimental Procedure.....	45
Scanning Electron Microscope (SEM).....	52
III. Finite Element Application.....	56
Motivation.....	56
Technique.....	57

IV. Results and Discussion	69
Bare Beam Results	70
Homogenous Coatings.....	76
History Effects.	76
Sweep Rate.....	81
Input Sweeps on Fully Coated Beams.	87
Material Properties through Finite Element Analysis	90
Generating Curves to Determine Material Properties.....	90
Apply Experimental Data to Finite Element Model.	98
Material Properties.....	105
Comparison of Results to Reed’s Results	111
Coating Material Comparison	114
Scanning Electron Microscope Analysis.....	118
Mag Spinel before Deformation.	119
Mag Spinel after Deformation near Beam Center.	124
Mag Spinel after Deformation away from Center.	126
Mag Spinel Compared to Previous Studies.	128
YSZ before Deformation.	129
YSZ after Deformation near Beam Center.	133
YSZ after Deformation near Beam Center.	135
YSZ Compared to Previous Studies.	136
V. Conclusions and Recommendations	138
Conclusions	138
Recommendations	141
Appendix A: VibrationVIEW Setup Procedure.....	144
Appendix B: YSZ Material Property Curves.....	157
Apply Experimental Data to Finite Element Model.	160
Bibliography	167

List of Figures

	Page
Figure 1: Schematic of the Air Plasma Spray Process.....	19
Figure 2: Example of Splat Structure of Plasma Sprayed Mag Spinel	21
Figure 3: Microstructure of YSZ Applied Via EB-PVD	22
Figure 4: Illustration of Nonlinear Characteristic	25
Figure 5: Half-Power Bandwidth Method	26
Figure 6: Composite Curve from Sweep Up and Sweep Down	27
Figure 7: Moment Due to Electromagnetic Excitation	30
Figure 8: Vacuum Chamber.....	33
Figure 9: Upper Node Beam Support	34
Figure 10: Lower Node Beam Support.....	35
Figure 11: Electromagnet with Cooling Tubes and Thermocouple.....	36
Figure 12: Beam Support Setup.....	37
Figure 13: Experimental Setup	40
Figure 14: SEM Image of Mag Spinel and Bond Coat on Titanium	42
Figure 15: Beam Dimensions.....	43
Figure 16: Cycles Build Up FRFs for Mag Spinel	47
Figure 17: Flow Chart for Input Voltage Sweeps.....	50
Figure 18: Diagram of SEM Specimen Cutout.....	53
Figure 19: Completed Specimen for SEM.....	55

	Page
Figure 20: Bare Beam Modulus Iteration	57
Figure 21: ANSYS Untested Beam and Detail Image.....	58
Figure 22: Determine Moduli Values for Polynomial Relationships	60
Figure 23: Reference at Interface.....	61
Figure 24: Polynomial Progression.....	62
Figure 25: Measured Data in Relation to Finite Element Data.....	64
Figure 26: Bare Beam Loss Factor	66
Figure 27: Material Properties in Relation to Strain.....	67
Figure 28: Bare Titanium Bar in Vacuum Sweep Down FRF.....	71
Figure 29: Bare Titanium Bar in Vacuum Sweep Up FRF.....	71
Figure 30: Bare Beam Loss Factor In a Vacuum Using Free Decay.....	72
Figure 31: Titanium Beam Loss Factor in Vacuum.....	75
Figure 32: Titanium Beam Resonant Frequency in Vacuum.....	75
Figure 33: Resonant Frequency Change due to Cycle Buildup for Mag Spinel Beams..	77
Figure 34: Mag Spinel Response to Input with Cycle Buildup	78
Figure 35: YSZ Resonant Frequency Change	80
Figure 36: YSZ Response Magnitude Change.....	81
Figure 37: Sweep Rate Comparison for Coating Modulus.....	83
Figure 38: Sweep Rate Comparison for Loss Factor.....	83
Figure 39: Sweep Rate Effect on Coating Modulus with Initial 5 Hz/min Sweep	85
Figure 40: Sweep Rate Effect on Loss Factor with Initial 5 Hz/min Sweep	86
Figure 41: Chosen Sweep Rate Compared to Other Rates	86
Figure 42: Sine Sweep of Titanium Bar Coated with Mag Spinel and Bond Coat	88

	Page
Figure 43: Sine Sweeps of Titanium Bar Covered with YSZ and Bond Coat.....	89
Figure 44: ANSYS Generated Beam with Coating	92
Figure 45: Storage Modulus Relationship to Frequency	95
Figure 46: Mode Shape Relationship to Coating Storage Modulus	96
Figure 47: Normalized Reference Strain Relation to Coating Storage Modulus.....	97
Figure 48: Strain Energy Ratio Relation to Coating Storage Modulus	97
Figure 49: Experimental Data Resonant Frequency Associated with Max Velocity	98
Figure 50: Mag Spinel Coating Modulus vs. Beam Measured Velocity at L/2.....	99
Figure 51: Strain Energy Ratio vs. Measured Velocity at L/2.....	100
Figure 52: Coating Loss Factor in Response to Response Amplitude at L/2	101
Figure 53: Mode Shape Response to Beam Response at L/2	102
Figure 54: Scaling Factor.....	103
Figure 55: Normalized Reference Strain Response to L/2 Measured Velocity.....	104
Figure 56: Reference Strain Response to L/2 Measured Velocity.....	104
Figure 57: Coating Modulus Change Due to Strain for Mag Spinel	105
Figure 58: Loss Factor Change Due to Strain for Mag Spinel	106
Figure 59: Loss Modulus Change Due to Strain of Mag Spinel.....	107
Figure 60: Coating Modulus Change Due to Strain for YSZ	108
Figure 61: Loss Factor Change Due to Strain for YSZ	109
Figure 62: Loss Modulus Change Due to Strain for YSZ	110
Figure 63: Reported Coating Modulus Calculated Via Forced and Free Response	111
Figure 64: Reported Loss Factor Calculated Via Forced and Free Response	112
Figure 65: Comparison of Coating Modulus Values	113

	Page
Figure 66: Comparison of Loss Factor Values	113
Figure 67: Comparison of Loss Modulus Values	114
Figure 68: Material Comparison of Coating Modulus.....	115
Figure 69: Material Comparison of Loss Factor.....	116
Figure 70: Material Comparison of Loss Modulus.....	117
Figure 71: Untested Mag Spinel SEM SE and BSE Images 200x Magnification	120
Figure 72: Untested Mag Spinel SEM SE and BSE Images 247x Magnification	121
Figure 73: Untested Mag Spinel SEM SE and BSE Images 385x Magnification	122
Figure 74: Untested Mag Spinel SEM SE Image 1500x Magnification.....	124
Figure 75: Tested Mag Spinel SEM SE Image Near Center 1603x Magnification.....	126
Figure 76: Tested Mag Spinel SEM SE Image Away From Center 1542x Mag.....	127
Figure 77: Previously Captured Mag Spinel 1500x Mag	128
Figure 78: Untested YSZ SEM SE and BSE Images 200x Magnification	130
Figure 79: Untested YSZ SEM SE and BSE Images 367x Magnification	131
Figure 80: Untested YSZ SEM SE Image 1601x Magnification.....	132
Figure 81: Tested YSZ SE Image Near Beam Center 1834x Magnification.....	134
Figure 82: Tested YSZ SE Image Away from Beam Center 1834x Magnification	135
Figure 83: Image of YSZ with 3 um Scale	136
Figure 84: Additional Image of YSZ with 3 um Scale	137
Figure 85: Figure of Bond Coat and YSZ Coating.....	137
Figure 86: Test Setup Screen Shot.....	144
Figure 87: Test Settings Profile Tab Screen Shot.....	145
Figure 88: Test Settings Schedule Tab Screen Shot	147

	Page
Figure 89: Options for VibrationVIEW Schedule	148
Figure 90: Test Settings Sweep Tab Screen Shot	149
Figure 91: Test Settings Resonance Tab Screen Shot	151
Figure 92: Sweep Down Test Screen Shot	152
Figure 93: Resonant Frequency Selection Screen	153
Figure 94: Resonant Frequency Selection Screen Cycles and Amplitude.....	154
Figure 95: Resonant Frequency Selection Screen Phase Tracking.....	155
Figure 96: Phase Tracking with Cycle Build-Up.....	156
Figure 97: YSZ Storage Modulus Relationship to Frequency.....	157
Figure 98: YSZ Mode Shape Relationship to Coating Storage Modulus.....	158
Figure 99: YSZ Normalized Reference Strain Relation to Coating Storage Modulus ..	159
Figure 100: YSZ Strain Energy Ratio Relation to Coating Storage Modulus.....	160
Figure 101: YSZ Coating Modulus vs. Beam Measured Velocity at L/2.....	161
Figure 102: YSZ Strain Energy Ratio vs. Measured Velocity at L/2	162
Figure 103: YSZ Coating Loss Factor in Response to Response Amplitude at L/2.....	163
Figure 104: YSZ Mode Shape Response to Beam Response at L/2.....	164
Figure 105: YSZ Scaling Factor	164
Figure 106: YSZ Normalized Reference Strain Response to L/2 Measured Velocity ..	165
Figure 107: YSZ Reference Strain Response to L/2 Measured Velocity	166

List of Tables

	Page
Table 1: Measured Material Values.....	44
Table 2: Cycle Buildup Schedule	47
Table 3: Input Voltages.....	49
Table 4: Responses of Six Beams.....	90
Table 5: Bare Beam and Magnet Material Properties.....	91
Table 6: Material Properties for Ceramic Hard Coatings Used in FEA	93
Table 7: Finite Element Results.....	94
Table 8: Finite Element Results at Reference Location.....	94

VIBRATION ANALYSIS OF COMMERCIAL THERMAL BARRIER COATINGS

I. Introduction

Fatigue

Repeated cyclic loading that results in structural failure without the structure being subjected to anywhere near its ultimate stress is called fatigue. The characteristic of this type of failure is the formation and propagation of microscopic cracks during each load cycle (Grady, 1999). Of interest to the United States military is the type of fatigue known as High Cycle Fatigue (HCF). This type of fatigue occurs when the stresses in a material fall within the elastic range and the loading range is greater than 10,000 cycles (Grady, 1999).

Over a 14 year period, 1982-1996, 56% of all Class A engine failures were attributed to High Cycle Fatigue (HCF) (Garrison, 2000). In a turbine engine, the parts most commonly subjected to HCF are the compressor and turbine section blades (Carter, 2005). The factors that contribute to this type of fatigue are aerodynamic excitation, mechanical vibration, airfoil flutter and acoustic fatigue (Cowles, 1996). With engine technology advancing at an astounding rate, it is now more important than ever to address

the HCF issue as parts are being called upon to handle more and more extreme loading conditions.

Damping

One of the factors that lead to fatigue, aerodynamic excitation, causes the blades in a turbine or compressor to vibrate. The airflow which is typically affected by the path of the air going around other blades and vanes can cause this vibration. A nearly unavoidable (due to components being operated at a wide range of frequencies) condition is when the blades are caused to vibrate at or near a resonant frequency (Blackwell, Palazotto, George, and Cross, 2007; Ivancic and Palazotto, 2005; Limarga, Duong, Gregori, and Clarke, 2007). While a designer has to try to eliminate the component operating at or near the resonant frequency for long periods of time, a part usually has to operate at its resonant frequency for a small period of time. In order to attenuate the response while the part goes through this frequency, it is necessary to damp the material to reduce the stress on the part.

Damping occurs when energy is dissipated and causes the response of a mechanical system to die out (Inman, 2001). This can be accomplished by active or passive means. In the past dampers or pads have been applied in order to try to damp the response (Limarga et al., 2007). Instead of attaching something to the blade, it would be convenient to have the source of damping integrated into the blade itself. A coating applied during the manufacturing process is a very attractive option for engine designers.

A successfully integrated coating will reduce the magnitude of vibration in the part. This reduction could significantly extend the service life by preventing or significantly postponing component failure (Ivancic and Palazotto, 2005).

Hard Coatings

Hard ceramic coatings have been used in turbine engines for years as Thermal Barrier Coatings (TBC). These coatings have been used to protect engine parts, such as turbine blades, from extremely high temperatures and from corrosion (Strangman, 1985). Additionally, work has been reported since 1973 highlighting the use of these coatings as having beneficial damping properties (Cross, Lull, Newman, and Cavanagh, 1973). One of the reasons for being popular as a damping device is that TBCs offer consistent damping over a wide range of temperatures (Patsias, Tassini, and Stanway, 2004).

One of the issues associated with these ceramic coatings is the fact that they exhibit nonlinear behavior (Blackwell et al., 2007; Patsias et al., 2004; Reed, 2007). The response of a component coated with a ceramic will vary with different strain amplitudes, thus the input excitation levels will have a direct affect on the damping characteristic of the material. The nonlinear behavior can be attributed to the coating internal friction which dissipates the energy (Blackwell et al., 2007; Patsias et al., 2004). How to deal with this nonlinear behavior explicitly will be discussed in a subsequent section.

Two different coatings which have been extensively researched are discussed in this study: magnesium aluminate spinel (Blackwell, 2004; Ivancic, 2003; Reed, 2007)

and yttria stabilized zirconia (YSZ) (Lauwagie, Lambrinou, Patsias, Heylen, and Vleugels, 2008; Limarga et al., 2007; Patsias et al., 2004; Strangman, 1985; Tassini et al., 2005). The main attraction of these TBCs as damping coatings is that they are already used in aircraft engines as thermal barriers and could easily be incorporated into existing engine designs. This isn't to say that these materials are the best damping coatings but because they are qualified for use in an engine they are accepted by both the government and civilian customers and by the manufacturers. A major issue in applying these coatings is ensuring that a consistent coating is applied every time (Bajan, Froning, Reynolds, and Ruggiero, 2008).

Application

In order to get these coatings onto a part, it is necessary to properly apply the coating to achieve ideal results. As will be shown, the application process has an effect on the microstructure which, in turn, has an effect on the characteristics of the coating. Two preferred methods at the moment are plasma spraying and electron beam evaporation—physical vapor deposition (EB-PVD).

Plasma Spray.

Plasma spray coating is the act of coating an object using high temperature ionized gas plasma to melt a coating material and spray the material on the substrate of the part to be coated. Typically a gas mixture (usually nitrogen, hydrogen, argon or helium) is passed through a high frequency electrical current which ionizes the gas to a

plasma state. The powdered coating material is melted by this high temperature plasma. The high velocity of this plasma acts as the accelerator to drive the molten powder to the surface to be coated as in Figure 1 (Blackwell et al., 2007; Strangman, 1985). Once the material impacts the surface, the molten material cools extremely quickly and establishes a bond. The solidified particles are called splats and they form the microstructure of the coating (Kroupa and Plesek, 2002). Factors that must be considered in the plasma spray process are particle size, degree of melting, plasma gas composition, spray angle, atmosphere (vacuum or standard atmosphere) and distance from gun to substrate.

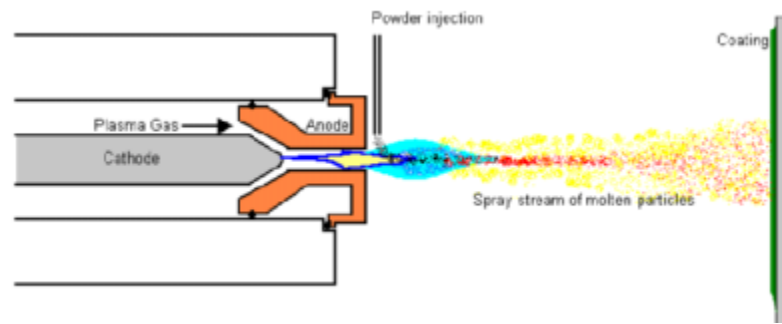


Figure 1: Schematic of the Air Plasma Spray Process (Ivancic, 2003)

Electron Beam Evaporation—Physical Vapor Deposition (EB-PVD).

In the electron beam-physical vapor deposition technique, a technique not investigated in this study, the coating material is vaporized and then condensed onto a substrate. The coating material is vaporized via a high power electron beam and is introduced into a high vacuum containing the part to be covered. The part to be coated is raised to temperatures up to, and in excess of, 1,000°C. As a result of the coating

material condensing on the substrate, the coating microstructure is arranged in uniform columns (Strangman, 1985; Tassini et al., 2005).

Microstructure.

The microstructure of plasma sprayed material consists of several layers of “splats” that are thin pancake like structures formed when the molten particles impact the surface of the material (Tassini et al., 2005). Early research noted that plasma sprayed YSZ had a distinct morphology of vertical cracks, horizontal cracks and a regular distribution of irregular pores (Coasack, Pawlowski, Schneiderbanger, and Sturlese, 1994; Pawlowski, Didier, and Fauchais, 1985). More recent research have defined these features (Kroupa and Plesek, 2002)(Tassini et al., 2005). Figure 2 is an SEM image captured by the author that shows the splat structure of a mag spinel coating along with the four defects common to plasma sprayed material: large irregular pores outside of the splats, small pores within the splats, “intersplat” cracks between the splats and perpendicular “intrasplat” cracks within the splats themselves (Kroupa and Plesek, 2002; Tassini et al., 2005). The resulting microstructure is roughly 10% to 15% porous (Kroupa and Plesek, 2002; Strangman, 1985). In a 1989 paper, Torvik discusses friction damping for layered materials along material interfaces. His conclusion is that significant energy dissipation could be achieved by friction along material interfaces (Torvik, 1989). The network of splats and the internal friction that results from the sliding of the splat surfaces along the microcracks is thought to be the mechanism which makes TBCs effective dampers (Kroupa and Plesek, 2002; Patsias et al., 2004; Tassini et al., 2005).

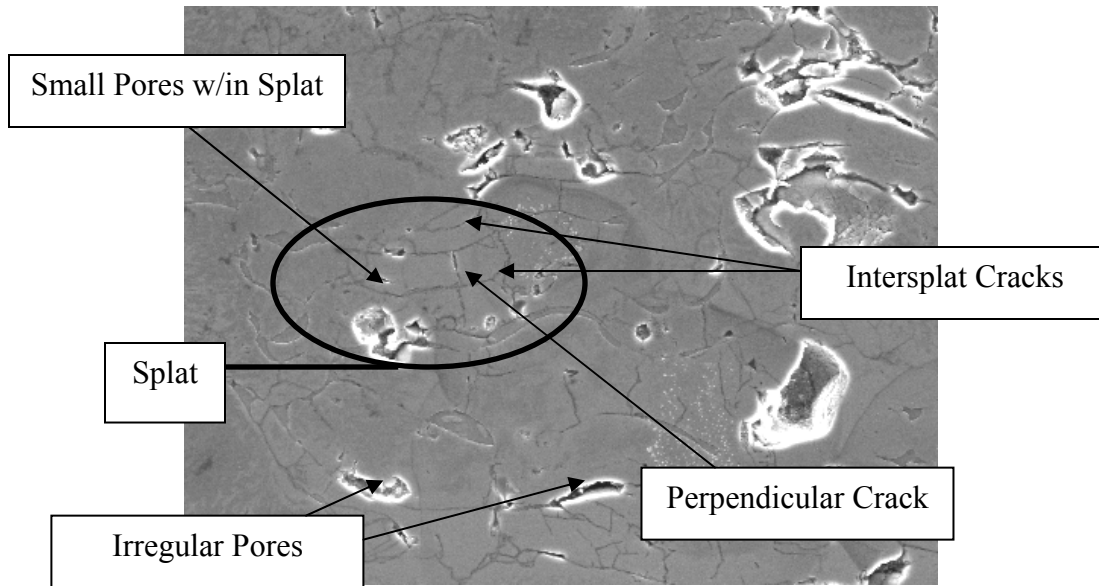


Figure 2: Example of Splat Structure of Plasma Sprayed Mag Spinel

The microstructure of these sprayed on hard coatings can reduce the Young's Modulus by 2 to 20 times (Kroupa and Plesek, 2002) due to the large number of microcracks. This reduction helps to minimize the stresses seen in the layer for given strains. The interfaces created by the porosity and the microcracks accommodate expansion and contraction of the material. The interfaces allow the material to slide over itself and dissipate energy through friction (Kroupa and Plesek, 2002; Tassini et al., 2005).

In Reed's dissertation, mag spinel exhibited a strain hardening response with cycle accumulation (Reed, 2007). It is assumed that microcracks develop during this process as the material is subjected to repeated deformation. As microcracks develop as cycles accumulate and the response of the material decreases it could be stated that the frictional energy dissipation is increased as more interfaces are developed to

accommodate this mechanism. Therefore, a high cycle test should be conducted to determine the material's stress and strain dependence on cycle accumulation.

The columnar microstructure of the EB-PVD (Figure 3) process reduces stresses and strains in much the same way as the plasma spray process. The interfaces created by this process allow for the material to run over itself and which creates friction. This energy dissipation mechanism is the same as for the plasma spray process. The resultant microstructure is considered much less porous than that for plasma spray and therefore doesn't have as high of modulus numbers as the same material applied via plasma spray (Tassini et al., 2005).

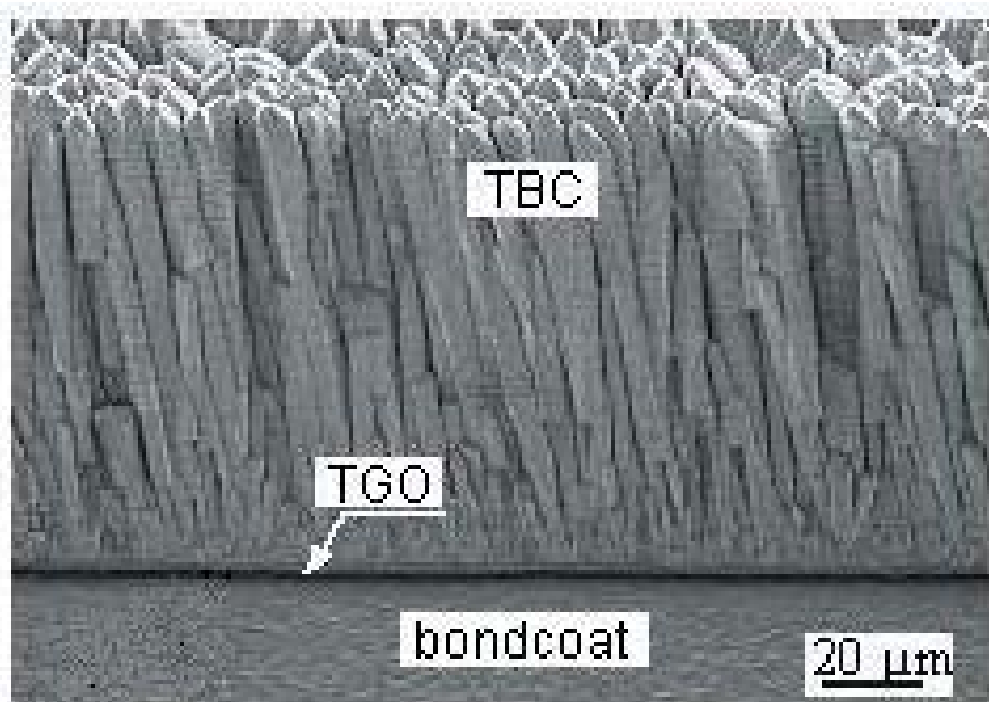


Figure 3: Microstructure of YSZ Applied Via EB-PVD (Tassini et al., 2005)

The main difference in the two types of application processes, besides the resulting microstructure, is that the material being coated is subjected to different

temperature requirements during application. In the plasma spray case the substrate is subjected to temperatures in the 100°C to 300°C (Strangman, 1985). This low temperature is ideal for parts, such as turbine engine compressor blades, whose microstructures can be altered by extreme temperatures. On the other hand, the temperatures reached by materials being coated by the EB-PVD method exceed temperatures of 1000°C. This is ideal for parts that are designed for use at high temperature, such as nickel based superalloys used in turbine engine blades. For parts operating in the compressor section, which can be made out of titanium, it is necessary to use the lower temperature process. Therefore, the plasma spray coating technique would be ideal for titanium compressor blades and will be used in this study. Although an EB-PVD coated specimen will not be covered in this report, it is recommended that a material that is capable of being coating using this process be investigated.

Bond Coat.

When an item is plasma sprayed, the primary feature which causes the ceramic to adhere to the metal substrate is mechanical interlocking. To ensure that this interlocking is as strong as possible, it is a common practice to apply a thin layer of bond coat. This bond coat adheres to the substrate material via a mechanical interlocking. In many cases this bond coat is a NiCrAlY material. This material will be used as the bond coat in this study. This bond coat is applied in such a manner that a high roughness is obtained. This roughness allows the ceramic to adhere more effectively to the substrate. This allows the cracks that are produced by the plasma spray process to be confined to the coating and not cause the bond to the substrate to weaken (Strangman, 1985).

Characterization

The problem with characterizing a hard coating is that it behaves in a nonlinear manner. Care must be taken as this nonlinear property requires different testing methods than traditionally used to determine the damping characteristics of a material. A frequency domain technique will be utilized to determine damping in this work. This technique, as opposed to a time domain technique, generates data which are more easily processed and interpreted.

Frequency Domain Technique.

In a frequency domain technique, a sinusoidal input signal, in the form of a voltage, is generated and applied to a system (in this study applied to an electromagnet) with the system's response (in this study the response of a beam) recorded as a function of frequency. This method can be performed by generating a forcing function, of the form $F = A \sin \Omega t$, and recording the system response as a sine sweep is performed across a range of frequencies. Where A is the voltage magnitude, t is time and Ω is the frequency of the forcing function.

In the case of a linear system, the response to the input will vary in magnitude as the input voltage magnitude and forcing function frequency vary. The resonant frequency of the response should be constant for all voltages. That is not the case for nonlinear materials, such as hard ceramic coating TBCs. In the case of the TBCs mag spinel and YSZ, a nonlinear softening characteristic is observed as input magnitude increases. This means that with increasing input voltage not only does the magnitude of

the response increase; the maximum frequency of the response decreases (Figure 4). The physical system which produces these results for this study will be further discussed in Chapter II. It is important that this feature be recognized early in testing so the proper sweep direction can be performed. In the case of softening, the proper direction is from high frequency to low frequency. This sweep direction will identify the peak of the curve even if there is a jump as the sweep goes over the resonant peak. If the sweep is performed from low to high frequency the maximum response of the signal will not be identified.

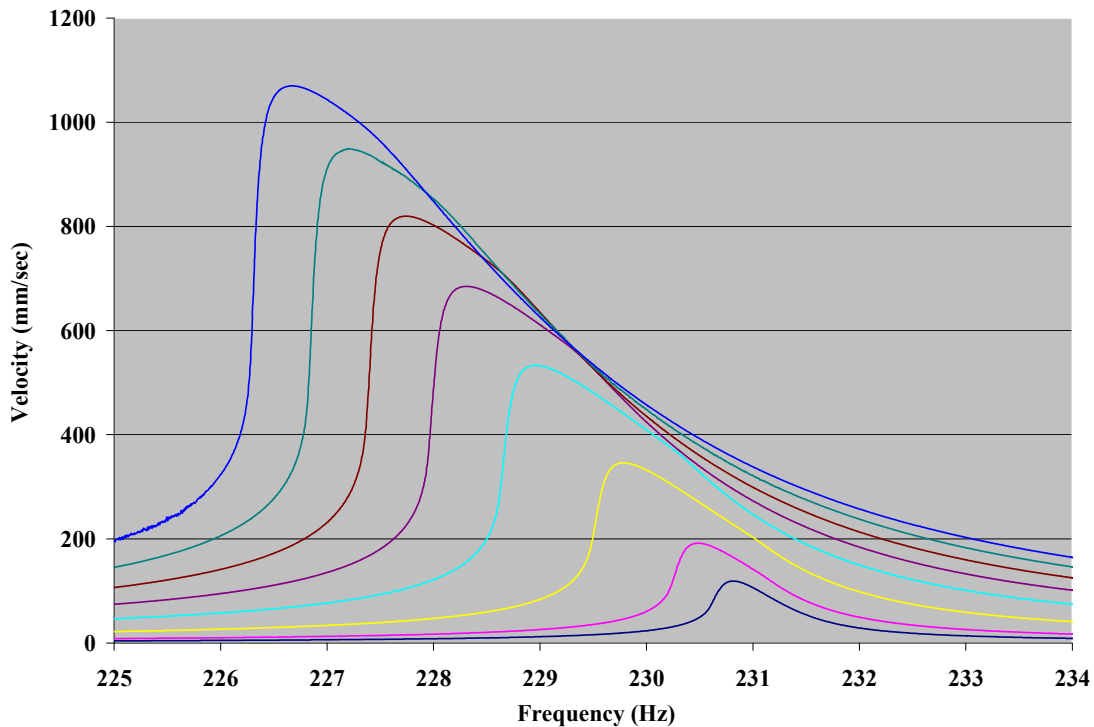


Figure 4: Illustration of Nonlinear Characteristic

As Reed described in his dissertation, a common way to generate damping data is to use the half-bandwidth method (Figure 5) (Reed, 2007). In this method, the maximum

amplitude, X_{\max} , of the response is recorded as well as the corresponding beam frequency, ω . Also recorded are the frequencies that are 0.707x times the maximum amplitude. The damping ratio, ζ , which is a value used to characterize damping in a system, can be found using the following equation.

$$\frac{\omega_2^2 - \omega_1^2}{\omega_3^2} = 4\zeta\sqrt{1 - \zeta^2} \quad (1)$$

For small damping ratio values the relationship can be simplified and assumed by:

$$\zeta = \frac{\omega_2 - \omega_1}{2\omega_3} \quad (2)$$

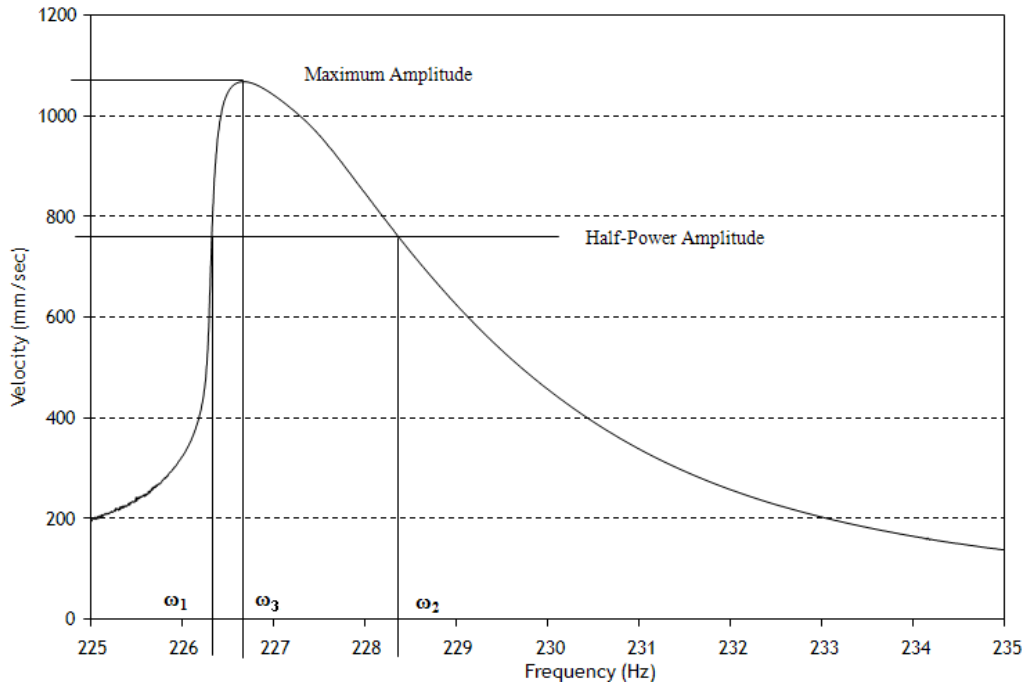


Figure 5: Half-Power Bandwidth Method

The half bandwidth method is intended to characterize linear systems. For non-linear systems, this method will generate damping values which are higher than the true values. This is because the nonlinear forced response curve, in addition to shifting to a

lower frequency, leans in the direction of the lower frequency. The sine sweep cannot physically sweep backwards so, instead of measuring the values of the curve, the data drops down to the next lowest value. This can be seen in Figure 6 where an actual up sweep and a down sweep have been superimposed on one another. The jump mentioned in a previous paragraph can be seen in this figure. Thus, the true $\omega_2 - \omega_1$ ($\Delta\omega$) value is actually less than is calculated by the generated curve.

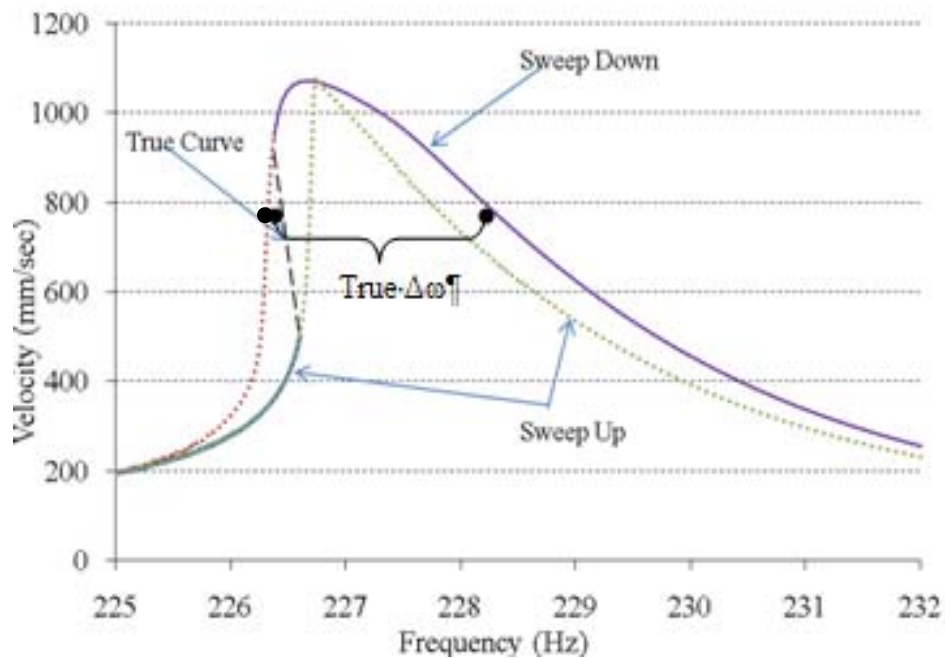


Figure 6: Composite Curve from Sweep Up and Sweep Down

Another useful value for characterizing damping properties, the loss factor of the material, η , is related to the damping ratio in the following manner (Reed, 2007).

$$\eta = 2\zeta \quad (3)$$

Another commonly used relationship is relating loss factor to the quality factor, Q :

$$\eta = 1/Q \quad (4)$$

It should be noted that as damping increases the loss factor, η , increases in value and the quality factor, Q , decreases. Therefore, for an investigation in damping a high η value and a low Q value are desired. An ideal system, completely undamped, would have η values equal to zero and Q values equal to infinity.

A consideration that must be accounted for in the recording of the forced response data is the rate of sweep. If the rate of sweep is too high it may be possible that the $\Delta\omega$ value would be too large. If the rate of sweep is too low, valuable time may be wasted. Therefore, a reasonable sweep rate must be utilized to record useful data. This parameter will be investigated in this research.

Air Damping.

Due to the small values associated with determining the loss factor and damping ratio, it is necessary to eliminate any unwanted damping associated with the system. Air adds a significant amount of damping and has been shown to obscure the true damping ratio. Allen, Lee, and Reed have all performed damping experiments and have determined that the use of a vacuum chamber leads to significantly more reliable results (Allen, 2005; Lee, 2006; Reed, 2007).

Boundary Conditions.

Boundary conditions imposed on a part being investigated have been shown to have an adverse affect on the generated results. Hoover wrote that traditional boundary conditions, cantilever in particular, have a profound impact on the recording of the natural frequency, damping and fatigue of a specimen (Hoover, 2004). In this traditional free-fixed cantilever setup, variations in clamp pressure or alignment can distort the data

which would be important in accurately describing the damping properties of the material (Runyon, George, Cross, Drew, and Jones, 2004).

An alternative to the cantilever setup is the use of a free-free setup. Various publications have reported the use of free-free setups as producing more reliable data (Hoover, 2004; Lauwagie et al., 2008; Reed, 2007; Runyon et al., 2004). The setups are all usually supported in one or more locations by a thin wire and are excited by external means with data collection also executed in a non-contacting fashion. In the experiments run by Runyon, Reed, and Hoover, which will be ran in a modified form for this effort, the specimen was excited by an electromagnet which produced a moment about the node of the first mode shape for a free-free beam. The beam has rare earth magnets attached to the beam at the lower node. The moment is produced by an alternating sinusoidal signal that causes the polarity of the electromagnet to switch from positive to negative. The rare-earth magnets react to the switching polarity which produces a moment about the lower node of the beam (Figure 7).

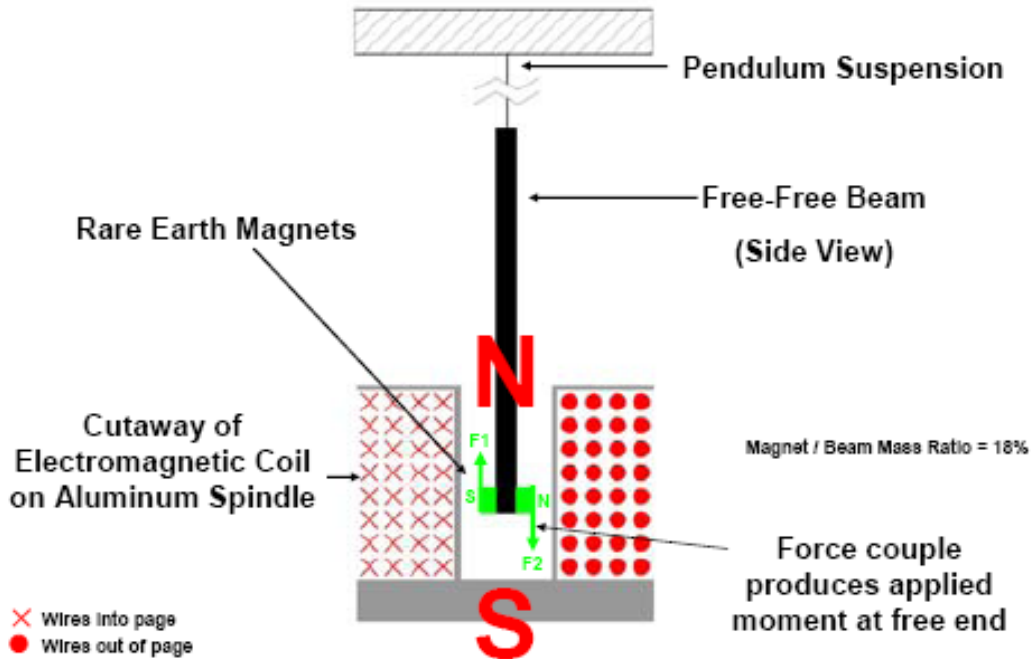


Figure 7: Moment Due to Electromagnetic Excitation (Hoover, 2004)

The displacement at the center of the beam is backed out by measuring the velocity at the center of the beam along with the frequency of the beam using the relationship:

$$\delta = \frac{V}{\omega} \quad (5)$$

where

δ = displacement (m)

V = measured velocity (m/sec)

ω = frequency (rad/sec)

The entire reason the specimen is tested within a vacuum chamber, in a free-free setup, with no attached measurement devices, is to reduce the amount of external factors affecting the damping of the system. The desired result is to record the true damping of the beam alone.

Finite Element.

With the damping material exhibiting nonlinear behavior it is necessary to employ finite element methods to determine the coating material behavior over a range of strains. This is done by characterizing a bare beam in a finite element model and then characterizing a coated beam in a finite element model. This method allows one to back out the properties of the coated beam over a range of frequencies and strains (Reed, 2007).

Objective

In this study, the elastic modulus and loss factor will be evaluated for magnesium aluminate spinel with a NiCrAlY bond coating on top of a titanium beam. The actual evaluation will not attempt to split the coating into top coat and bond coat parts but will be for the combination of the two materials. This will be accomplished through the use of a free-free boundary condition test setup inside a vacuum using a Laser Doppler Vibrometer (LDV) for data measurement. The use of these conditions will allow for a more reliable representation of the material characteristics. A coating consisting of yttria stabilized zirconia (YSZ), with a NiCrAlY bond coat, will also be evaluated to determine whether or not the two coatings display similar material characteristics.

In order to check the material's response to cyclic loading, 4 million cycles will be ran with sine sweeps performed, according to a set schedule defined in a subsequent chapter, along the way to determine the dependence of resonant frequency on cycle

count. Four million cycles was chosen because it was reported that was sufficient to break in the materials (Reed, 2007). Once 4 million cycles have been reached, a series of sine sweeps from high frequency to low frequency (based on the resonant frequency of the beam) will be performed with varying, increasing input voltage magnitudes. The data recorded from these sweeps include maximum velocity at the center of the beam, resonant frequency, displacement at the center of the beam, loss factor of the beam and coating calculated using the half-power method. This information will be used in conjunction with a simple finite element model, to determine the actual damping characteristics of the material. The data that will be determined using the finite element method will be the mode shape at the center of the beam, the normalized reference strain at the center of the beam, the coating modulus of the beam and the strain energy ratio of the beam. In the finite element model, the bond coat and the coating will be homogenized into one coating. The values calculated using the finite element model and the experimental method will be used to relate coating modulus, coating loss factor and coating loss modulus to the actual strain at the center of the beam.

Finally, a scanning electron microscope (SEM) will be employed to study the microstructure of the coating to determine what physical changes take place on a microscopic level. The samples that will be compared are a specimen that has undergone 4 million cycles and a specimen that has not undergone any testing. This should shed some light on the physical damping mechanics of the coating.

II. Experimental Technique and Setup

Setup

As discussed in the introduction, and following the experimental setup of Reed, it was decided to use a vacuum chamber to conduct the experiment in order to reduce unwanted air damping. The entire experimental portion of this research was conducted at the AFRL/RZTS Turbine Engine Test Facility in Dayton, Ohio. The size of this vacuum chamber measures 0.94 m x 0.69 m x 0.66m. The vacuum chamber, shown in Figure 8, was able to achieve pressures of 25 mm Hg.



Figure 8: Vacuum Chamber

As was previously discussed, the test was carried out with a free-free boundary condition so as to reduce system energy dissipation. This was achieved by using a low gauge

monofilament wire connected to the beam via the upper node of the first bending mode and the lower node of the first bending mode. A small half tube was glued to the upper node to allow the monofilament to pass through (Figure 9).

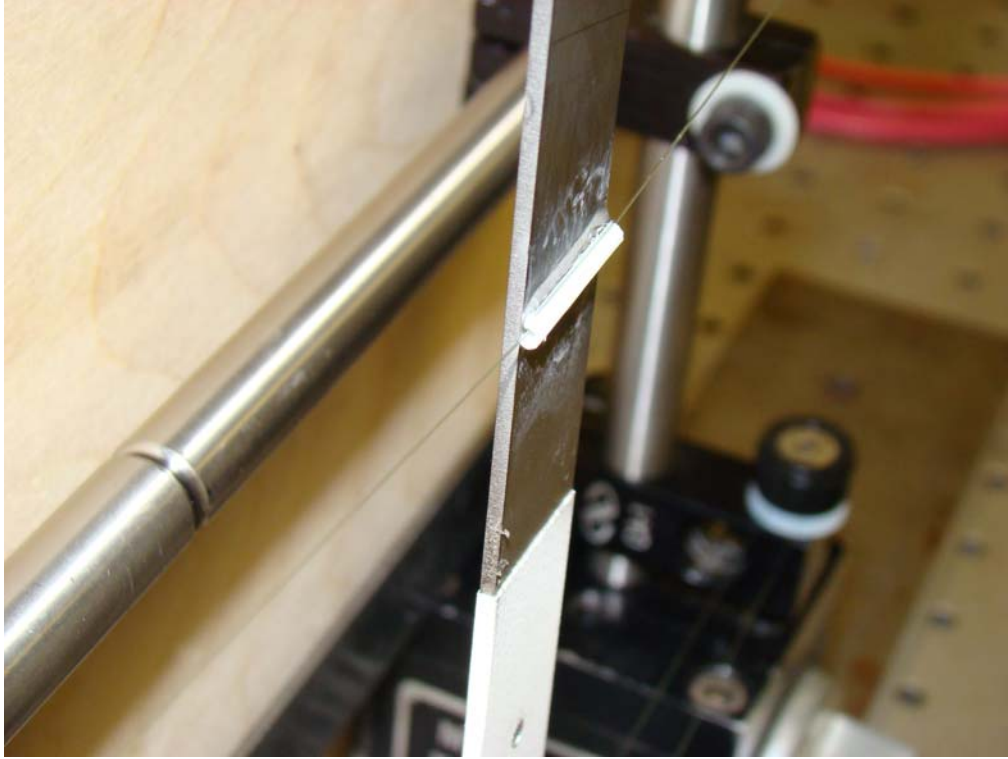


Figure 9: Upper Node Beam Support

This setup allowed the beam to rotate freely around the upper node. A modification from Reed's experiment was to shorten the upper and lower strings significantly and decrease the angle made by the upper strings with the horizon. This helped to avoid the string natural frequency coinciding with the beam natural frequency and possibly adding any unwanted noise to the data. The lower strings were horizontal and attached to the lower node of the beam sandwiched between magnets. Four magnets per side, two glued to the

beam and two held on via magnetism, were used to excite the beam first bending mode (Figure 10 and Figure 11).

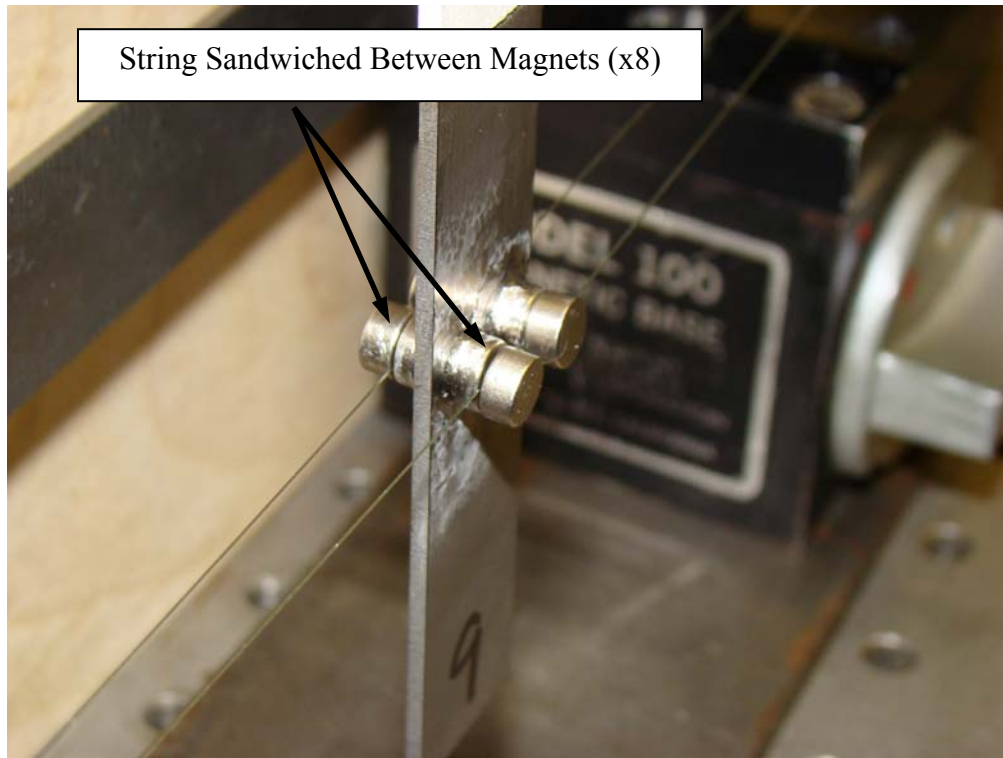


Figure 10: Lower Node Beam Support

The lower node setup was used for two reasons. First, it connected the lower node to the string without using any adhesive. Second, by using eight total magnets at the lower node, it was possible to generate a larger beam response to the electromagnet. This setup may have added damping but the increased beam response was needed. The string ends were attached to the support structure via pressure by clamping them between a screw and a piece of metal. The reasoning behind attaching the strings to the node lines was to reduce any pendulum motion. With this type of setup, the beam is free to rotate about the strings and the beam dynamics are minimally impacted (Figure 12).

In order to excite the beam a custom built water cooled electromagnet designed for a similar experiment was used (Runyon et al., 2004). The outer diameter of the magnet was 9 cm and the inner diameter was 3.75 cm, the height of the magnet was 7.5 cm. The magnet was constructed of 12 gauge wire and it is estimated that 650 turns were used in its' construction (Reed, 2007). Integrated into the electromagnet were water-cooling tubes and a thermocouple (Figure 11). The cooling tubes allowed the magnet to run at high voltages for long periods of time. The temperature could be monitored continuously via the embedded thermocouple. The two devices integrated into the electromagnet were important as they helped maintain a consistent temperature in the 40°C range. If the magnet became too hot the electromagnetic properties could have changed and altered the experiment.

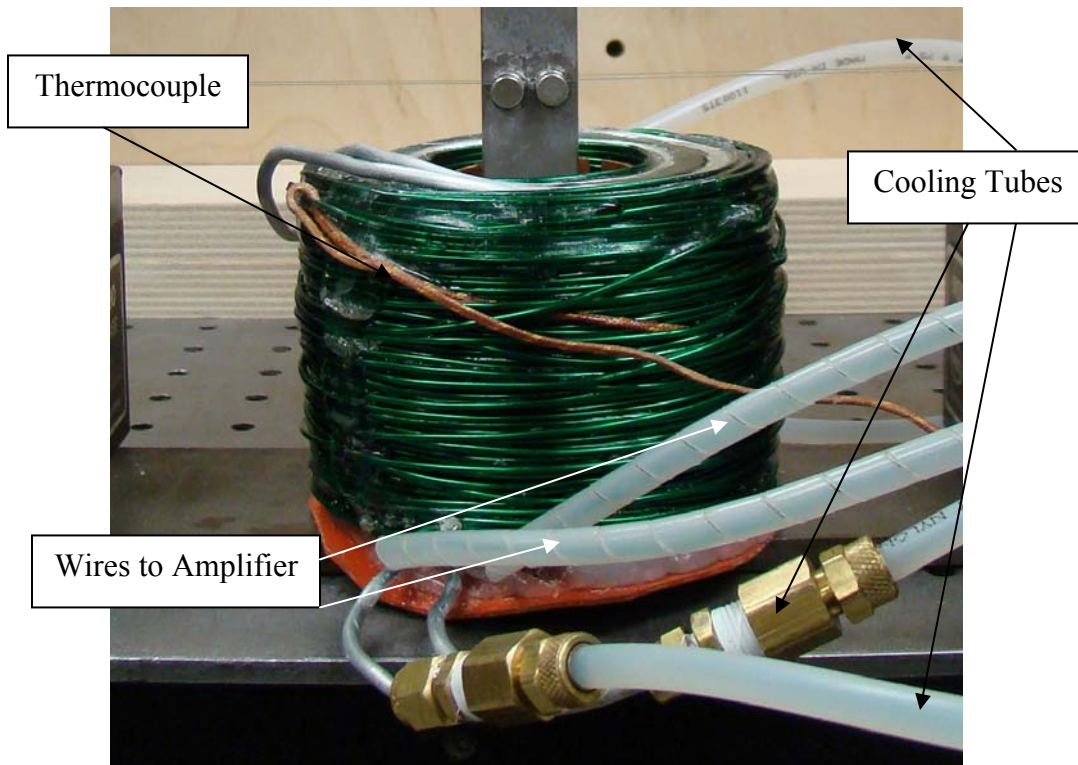


Figure 11: Electromagnet with Cooling Tubes and Thermocouple

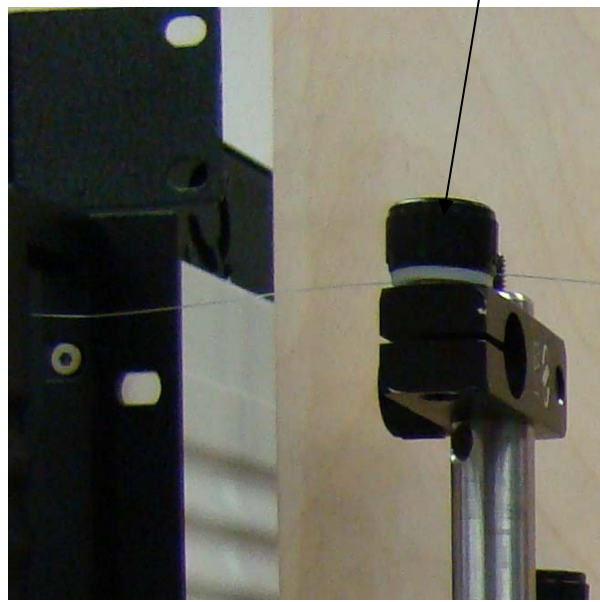
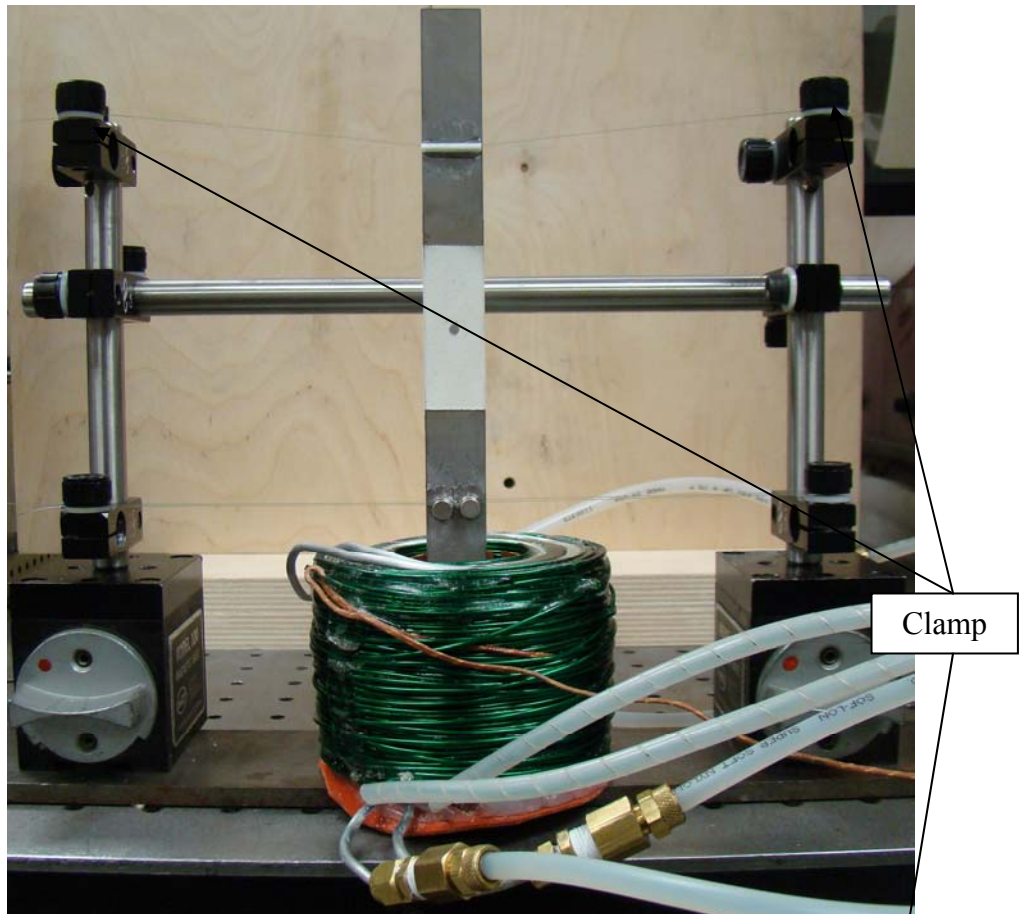


Figure 12: Beam Support Setup

The distance the rare earth magnets were above the electromagnet played a significant role in the response of the beam. It was not possible to reach the desired excitation by adjusting the drive voltage alone. If the magnets on the beam were too close to the electromagnet, too large of a response could be generated and the magnets could possibly break off of the beam. If the magnets were too far, it wouldn't be possible to generate a large enough response. This variable had to be fine tuned by trial and error to get the desired response. The final distance was approximately 25.4 mm.

The electromagnet was driven by the VibrationVIEW 8500 software and hardware system. This system hardware produced a sinusoidal signal that was amplified by a MB Dynamics SL600VCF Power Amplifier. The VibrationVIEW software allowed the user to program a wide array of test setups for desired input voltages. With a constant input voltage, the software could be swept from high to low frequency recording data at a specified sweep rate (Hz/min). The software also allowed the user to vary the input magnitude from sweep to sweep and to accumulate cycles in a predetermined routine. When building up cycles, it was possible to make a sine sweep at the user's choosing to determine the resonant frequency and then use phase tracking to stay at resonance. When "Phase Tracking" is enabled, the controller will automatically adjust the output frequency to keep the phase shift between the selected channels at the selected phase difference, and will hold that phase even if the resonance frequency changes over time. Usually this phase difference is either +90 degrees or -90 degrees, but any phase value may be entered, as desired (*VibrationVIEW*2007). Phase tracking is the relative difference in the expected phase response of the test specimen and the actual response of the test

specimen. Another feature which was utilized in this experiment was the ability to control the beam response to maintain a constant strain. This was accomplished by setting a velocity value which was recorded and monitored through the LDV via the software. The voltage was generated by the VibrationVIEW software and was sent through the amplifier producing a magnetic couple (Figure 7).

VibrationVIEW hardware and software was connected to a single point Polytech OFV-303 Laser Doppler Vibrometer (LDV) which could capture velocities up to 10 m/sec. The LDV information was received through the VibrationVIEW software and was internally processed. The LDV helped generate output data consisting of frequency vs. time, velocity vs. frequency, velocity vs. time and transmissibility vs. frequency data. In VibrationVIEW, transmissibility is a relationship that gives the value of actual response as a percentage of desired response. This value can be over 1 when a resonant response is achieved. Figure 13 shows the experimental equipment setup used to determine the coating material properties.

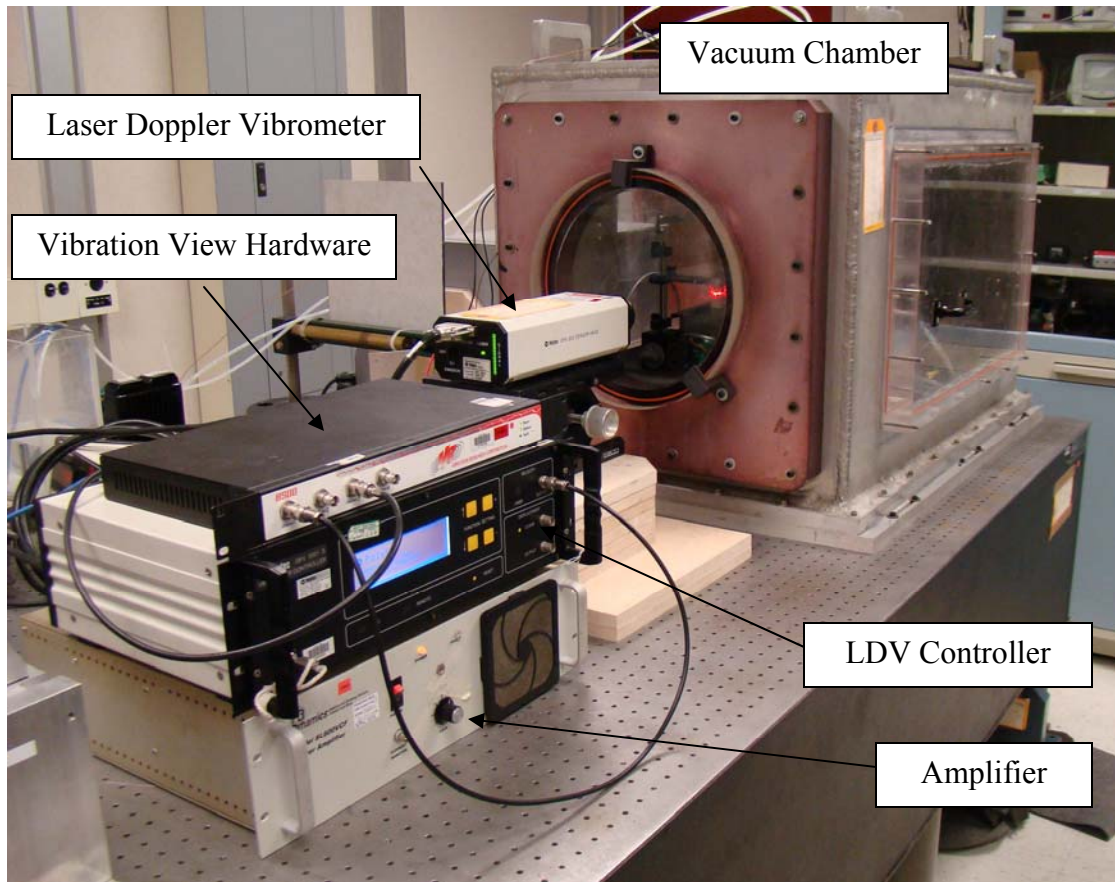


Figure 13: Experimental Setup

Specimens

Twenty-six beam specimens were cut by Kerf Waterjet in Dayton, OH. All specimens were cut from a single sheet of 1.6 mm thick Ti-6Al-4V. The beams were all waterjet cut in the same orientation so no questions could be raised concerning the variations due to how the sheet was rolled. The beams were cut to measure 19.05 mm x 203.2 mm x 1.6 mm. There were four categories of beams. The first group was

uncoated. There were eleven beams in this group but only one was used in the experiment. The other ten beams were unintentionally cut by the waterjet operator. The other three groups all had a coating covering the center 25% of the beam over both faces. Five specimens were in each group. The first group was coated with 0.0762 mm (3 mils) of NiCrAlY Bond Coat. The next group had the .0762 mm bond coat covered by 0.1778 mm (7 mils) of magnesium aluminate spinel. The final group had the same coating thicknesses as the mag spinel but the top material was yttria stabilized zirconia (YSZ).

The beams were coated by APS Materials Inc., Dayton, OH. All 15 beams that received a coating were completely masked except for the middle 25% of the beam. A plasma spray machine was used by an operator to coat the beams. The bond coat was the first layer applied to the beams. All beams were on the table at the same time when a 0.0762 mm thick bond coat layer was applied. Once the desired thickness was achieved, ten of the fifteen samples were taken off the table. Five of those samples would receive a coating of YSZ. The five beams remaining on the table were coated with mag spinel to a thickness of 0.1778 mm and then removed from the plasma spray area. Five samples with the bond coat already applied were then placed back on the table and coated with 0.1778mm of YSZ. The resulting thicknesses were measured by hand using a caliper by the plasma spray technician. The accuracy of the caliper is unknown as the technician made all of the measurements while coating the beams. As no measurements (weight, thickness) were made of all the samples with just bond coat, it was not feasible to try to determine the characteristics of the beams with both bond coat and top coat. The decision was made to combine the two materials into a homogenous material. The idea

being that the thickness of the bond coat is so rough and random it would not be possible to determine the characteristics of either material without making several assumptions. Figure 14 shows an SEM image which confirms this. The lower light color is the titanium, the thin lighter color above the titanium is the bond coat and the dark material above the bond coat is the mag spinel.

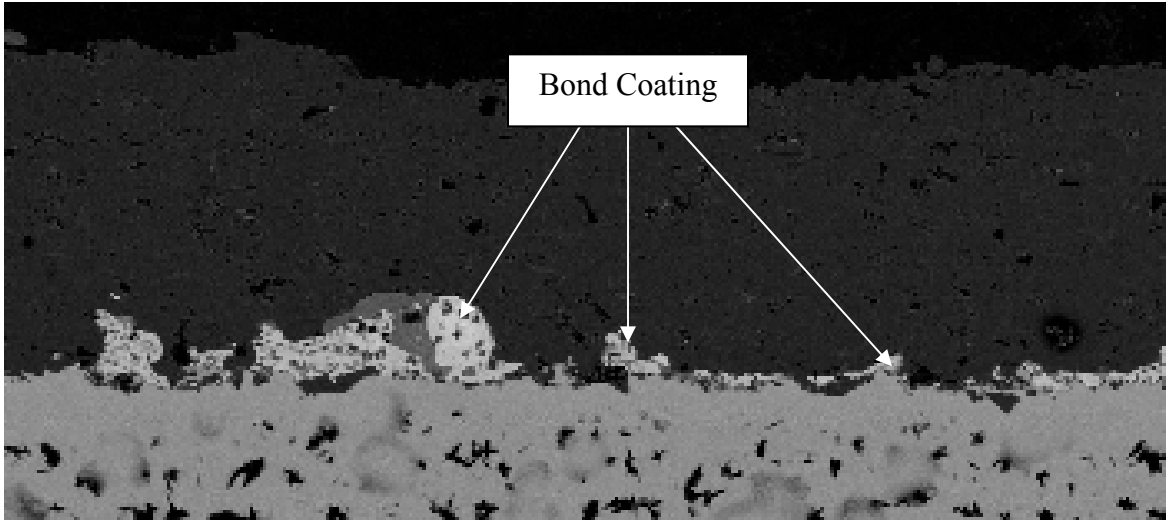


Figure 14: SEM Image of Mag Spinel and Bond Coat on Titanium

The actual as-sprayed values of thickness are shown in Table 1. These thickness values reflect the total thickness of the coating on both sides of the beam combined. The densities were calculated by weighing each beam on a scale and calculating the volumes of the bars before and after coating using the relationship:

$$\rho = \frac{Mass}{Volume} \quad (6)$$

The volume of each bar was calculated by measuring and averaging five points in the width direction, W , five points in the thickness direction, t_b , and two points in the

length direction, L . For the coating, three measurements were taken and averaged for the combined titanium plus coating thickness, t_t , three for the width, W , and two for the length, L_c . The reported coating thickness, t_c , reflects the value for each side of the beam and was calculated by dividing the difference of t_t and t_b by two. It is absolutely necessary to measure these dimensions with a scale and caliper that has a high degree of accuracy. Accuracy is very important as the coatings are such a small percentage of the total mass of the system, especially the bond coat. The standard deviation for the bond coat thickness was 0.006 mm while the values for the Bond+Mag Spinel coating and Bond+YSZ coating were 0.008 mm and 0.007 mm, respectively. These values indicate a relatively uniform spray thickness. In reality, the surface of these coatings resembles a series of peaks and valleys. The caliper used to measure these thicknesses measured the highest peak or peaks. As can be seen in Figure 14, the highest peak for the bond coat is the only thickness that approaches the desired .0762 mm thickness. When calculating the density of bond coat this could lead to a density calculation for the NiCrAlY that is too low. In reality the bond coat is probably much denser.

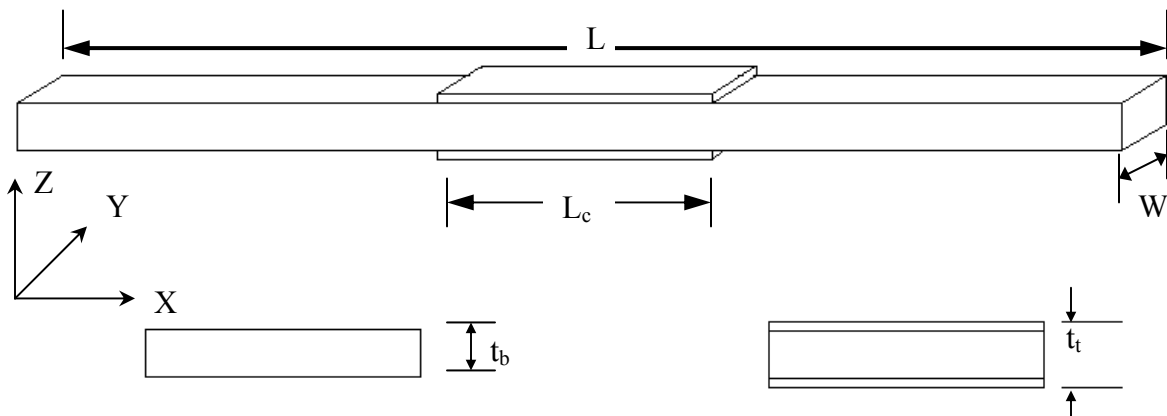


Figure 15: Beam Dimensions

Table 1: Measured Material Values

Specimen	Thickness, t_c (mm)	Width (mm)	Length, L_c (mm)	Mass (g)	Density, ρ_c (g/cm ³)
Bond Coat Only					
1	0.0485	19.18	51.05	0.118	1.27
5	0.0478	19.13	51.66	0.072	0.80
6	0.0631	19.11	50.67	0.127	1.06
7	0.0552	19.08	51.36	0.144	1.43
8	0.0578	19.09	50.65	0.134	1.27
Bond+Mag Spinel					
2	0.268	19.35	50.83	1.453	2.681
3	0.256	19.30	51.33	1.447	2.774
4	0.250	19.35	51.31	1.302	2.552
9	0.256	19.34	52.07	1.491	2.822
15	0.267	19.33	52.30	1.551	2.800
Bond+YSZ					
10	0.274	19.37	52.20	2.420	4.235
11	0.261	19.32	52.68	2.355	4.326
12	0.282	19.35	51.87	2.309	3.979
13	0.272	19.53	52.25	2.451	4.177
14	0.273	19.39	52.53	2.388	4.165

Experimental Procedure

The forced response test was conducted to determine the system loss factor for the bare beam and for the coated beams. The system loss factor being the loss factor for the beam plus coating plus attached magnets and supports. The other two loss factors considered are the bare beam loss factor which is the loss factor for the bare beam plus the magnets and supports and the coating loss factor which is the loss factor for the coating alone. The bare titanium beam system was considered linear because the resonant frequency did not increase or decrease as input voltage was varied. The bare beam was not put through the break in process described later in this section.

Once the coated beam has been placed in the vacuum chamber and the pressure has stabilized by remaining constant for 5 minutes, the forced response of the beam can be determined and data collection (utilizing the half-bandwidth method) can be carried out. It is necessary to conduct a quick (10 Hz/min) sine sweep from high frequency to low frequency and from low frequency to high frequency over a wide frequency range, 40 Hertz, to identify the approximate frequency of resonance and to determine whether or not strain softening or strain hardening is occurring. This sweep large sweep range also enables the user to determine the beginning and ending frequencies (10 Hz apart) for the sine sweeps. If specimens are similar, previous papers should just serve as a guide to determine a sweep range as the frequency varies from test to test and specimen to specimen. If the resonant peak is not identified in the first sweep adjust the sweep frequency range as necessary. This sweep is conducted at a high voltage (8 Volts) to

ensure an easily identifiable response is achieved. It is noted that this is a large input. The response of the coated beam was approximately $890\mu\epsilon$. The bare beam could not undergo this voltage without damaging the test setup and was swept at no higher than 1 Volt. As it is only a quick sweep to determine the location of the resonant peak, it is assumed a large input has no significant effect on the material properties of the beam. Once the resonant frequency is determined, and hardening or softening observed (to determine if an up or down sweep is needed for the test), the cycle accumulation process can begin.

The magnitude of the input voltage for the sine sweeps during the break in cycles was determined from previous experiments (Reed, 2007). To determine how the resonant response of the beam varies as cycles accumulate, it is necessary to set up a schedule of cycles with pauses at set intervals where a down sine sweep can be conducted at a slow sweep rate (2 Hz/min) to determine the resonant frequency change (Table 2). This helps to track how the material changes with use. A stiffness increase in the material is expected to occur during the cycle buildup, which is indicated by an increase in resonant frequency (Figure 16). The VibrationVIEW software allows the user to determine when the cycle buildup process pauses to run the sweeps. The procedure is explicitly defined in Appendix A. The schedule was setup with sine sweeps conducted more frequently early in the test (half the sweeps accomplished in first 25% of test) as it was observed in previous works that the material went through the most changes early in the break in process (Reed, 2007). It should be noted that each 5 minute sweep consisted of roughly 68,000 cycles. These cycles were not included in the overall cycle count.

Table 2: Cycle Buildup Schedule

Cycles (N)	Sweep	Cycles (N)	Sweep	Cycles (N)	Sweep
0	1	350000	11	1950000	21
25000	2	450000	12	2200000	22
50000	3	550000	13	2450000	23
75000	4	650000	14	2700000	24
100000	5	750000	15	2950000	25
125000	6	950000	16	3200000	26
150000	7	1150000	17	3450000	27
200000	8	1350000	18	3700000	28
250000	9	1550000	19	3950000	29
300000	10	1750000	20	--	--

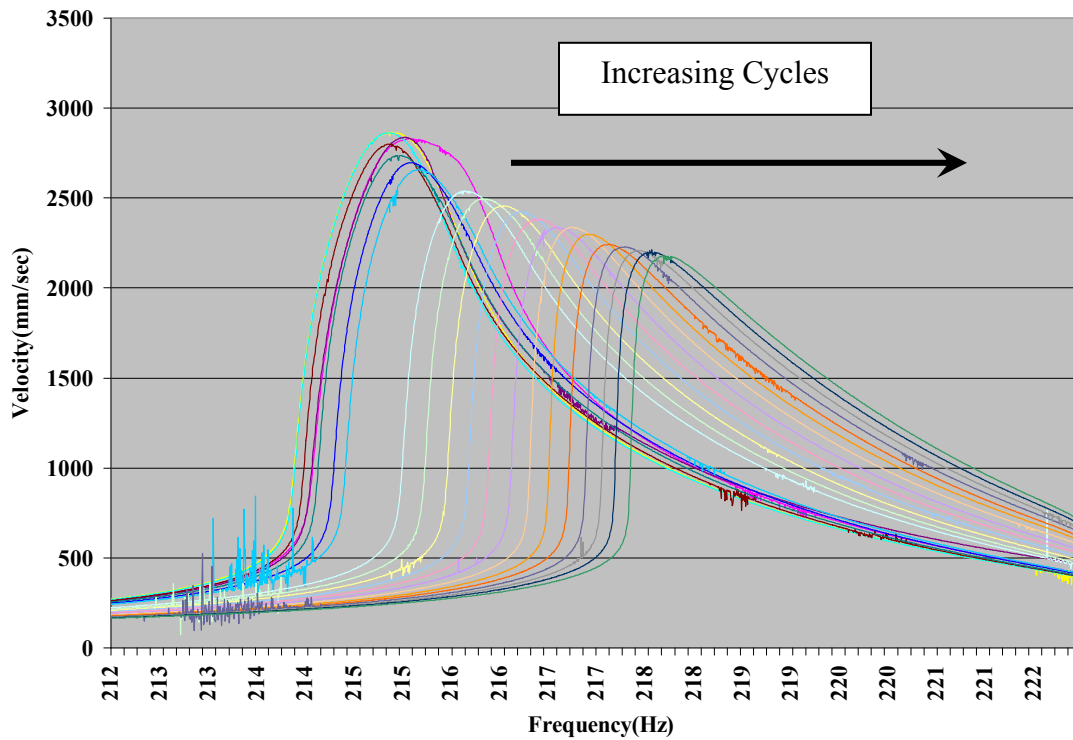


Figure 16: Cycles Build Up FRFs for Mag Spinel

To allow the cycles to build up at a set strain, a velocity is identified that should be exhibited by the beam and recorded via the Laser Doppler Vibrometer (LDV). This

velocity allows a pseudo constant strain to be applied to the beam as determined through finite elements, discussed in a subsequent chapter, and the displacement-velocity relationship discussed for equation five in chapter one. The beams coated with mag spinel were broken in during the cycle build up by maintaining a velocity at the center of the beam of 2.2 m/sec. The beams coated with YSZ were broken in by maintaining a velocity of 1.3 m/sec. The difference in velocities can be explained by the fact that the YSZ could not be excited to as high of a velocity as the mag spinel. The reason this is a pseudo constant strain is because as the cycles begin to accumulate the natural frequency of the beam will increase while the velocity is constant. It is assumed the shift is not so significant from beginning to end to have a major impact on the applied strain. The peak strain range, as measured at the center of the beam, for the mag spinel ranged from $874\mu\epsilon$ to $905\mu\epsilon$. The yield stress for Ti-6Al-4V is 980 MPa (*MatWeb material property data* .2008) which corresponds to a strain value of $8900\mu\epsilon$. This indicates that the titanium is never near the yield stress for the titanium beam and therefore no permanent deformation is assumed to have taken place in the titanium.

Once four million cycles have been reached and the resonant frequency of the beam has more or less become stable, the response to variable input voltage, or various strain levels, portion of the test can be conducted. This portion of the experiment is where the resonant frequency, ω_o , and its related maximum velocity, V_{max} , associated with a certain input voltage will be generated. These two values will be used to determine the system loss factor, η_{sys} , as well as the bare beam loss factor, η_{bare} , via the

half-power bandwidth method. The displacement at the center of the beam, δ , can also be determined by using Equation 5.

To begin, the sweeps were conducted from high frequency to low frequency as the beams exhibit strain softening due to the coatings. It should be noted that the materials exhibit strain hardening with cycle accumulation but the materials exhibit strain softening with input voltage increase. The sweep rate was chosen so as to be a slower rate (2 Hz/min) than Reed (3 Hz/min) (Reed, 2007). The routine would sweep through a 10 Hertz range around resonance for mode 1 at the lowest desired input voltage and then after a complete sweep at that level automatically go to the next highest input voltage value and do the sweep again. This process was repeated, uninterrupted, over the 18 different input voltages shown in Table 3. Each sweep produced a resonant frequency and a maximum velocity associated with that frequency. The loss factor and the displacement associated with each voltage could be determined indirectly using those two values and the values that could be calculated in relation to them. Figure 17 shows how to generate one input voltage sweep.

Table 3: Input Voltages

Sweep	Voltage (V)	Sweep	Voltage (V)
1	0.05	10	2.00
2	0.10	11	2.25
3	0.25	12	2.50
4	0.50	13	3.00
5	0.75	14	4.00
6	1.00	15	5.00
7	1.25	16	6.00
8	1.50	17	7.00
9	1.75	18	8.00

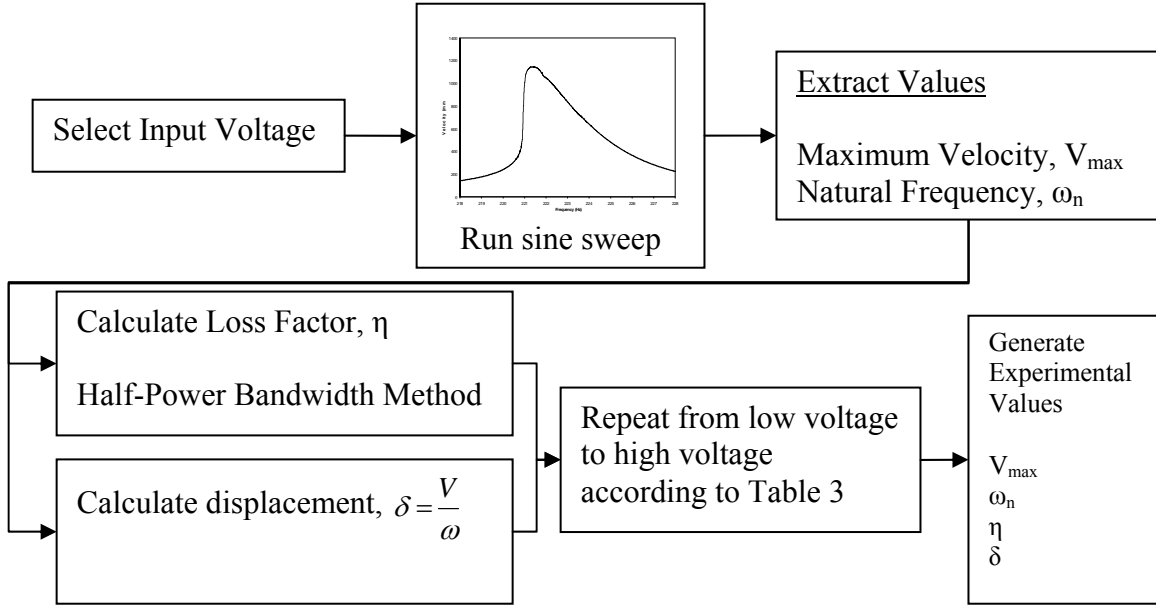


Figure 17: Flow Chart for Input Voltage Sweeps

It should be noted that the curves generated by the sine sweeps were a series of 2000 points recorded every 0.005 Hertz. As a result of how these values were recorded, exact frequency values were not available for the two $0.707V_{\max}$ values needed to utilize the half-power bandwidth method of determining loss factor. Therefore, it was necessary to employ the TREND function in Microsoft Excel. This was a linear interpolation that helped determine the frequency at $0.707V_{\max}$.

This input sweep test was performed for the bare beam and the coated beams. The bare beam could not undergo the same input voltages. This was due to the absence of an applied damping material and the use of vacuum conditions. The maximum voltage the beam was subjected to was 1 Volt. Voltages higher than this value could excite an

extremely large velocity response and deflection and cause the magnets to come off of the beam.

One bare beam was tested so the resonant frequency and loss factor could be determined. These values will be used to determine the coating loss factor in a subsequent section. Three beams coated with mag spinel and NiCrAlY and three beams coated with YSZ and NiCrAlY were tested.

The other test that was conducted was a sweep rate test. This test followed the processes described for the input test but for several different sweep rates. This test was only carried out on one beam.

To reiterate, the following steps were conducted on each coated specimen:

1. The resonant frequency of the beam was identified, as well as a hardening or softening characteristic, by doing an initial quick sweep (10 Hz/min) from high frequency to low frequency and from low frequency to high frequency over a range of 40 Hertz using an input voltage of 8 Volts.
2. An appropriate input voltage of 2.2 Volts was determined.
3. The beam was subjected to the cycle build up schedule, with corresponding sine sweeps, shown in Table 2.
4. Natural frequency and maximum velocity were recorded after each sweep.
5. Once the cycle build up schedule was completed 18 input voltage sweeps were conducted in accordance to Table 3.
6. After each sweep the resonant frequency and velocity associated with that natural frequency was recorded.

7. Loss factor and the displacement at the center of the beam associated with a voltage input can be indirectly calculated, using the half-power bandwidth method, by using the previously recorded natural frequency and velocity values.

Scanning Electron Microscope (SEM)

In order to do a thorough evaluation on the microstructure of the coated specimens it was necessary to examine the samples under a scanning electron microscope (SEM). There were two objectives in examining the samples under the SEM.

1. To determine the microstructure before deformation
2. To determine any changes of the microstructure after deformation

The purpose of these examinations was to determine whether or not the assumed damping property of movement along the splat boundaries as a damping mechanism was valid (Strangman, 1985). In order to do this, the boundaries between splats and the vertical boundaries within cracks should be examined. A widening of cracks and an increase in the number of cracks would confirm that Strangman's observation that the coatings increase in damping as more boundaries are formed (Strangman, 1985).

There were two samples of the YSZ and mag spinel , respectively. One sample of each coating that was untested was observed to get a before deformation picture. One sample was taken of each coated beam that had been subjected to cyclic loading.

To prepare the specimens for observation under the FEI Quanta 600 F SEM (located in the AFRL Materials and Manufacturing Directorate) with secondary electron

(SE) and back scanning electron (BSE) capability, it was necessary to dissect the beams in a way that would allow for the observation of stress variation from the point of maximum stress (in the center of the beam) to a point of lesser stress. It was decided to cut the beams with a diamond bladed saw at the center of the beam, down the length of the beam (Figure 18). This type of cut would allow for the observation of the cross section of the beam in an area of high stress and in an area of lower stress.

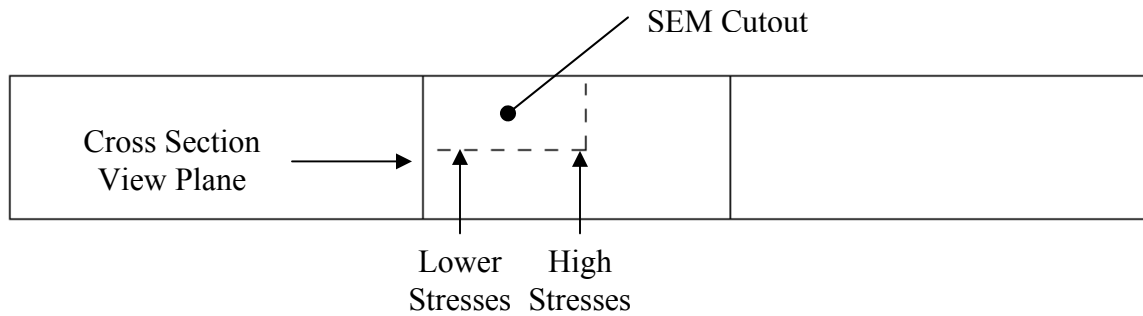


Figure 18: Diagram of SEM Specimen Cutout

Next the samples which were thin rectangles approximately 10mm X 10mm X 0.026mm in size were put into a hot press so the specimens could be placed in a mount so they could be viewed under the SEM. This hot press put the specimens in a mount in such an orientation that the cross section could be observed. The resulting specimen resembles a small hockey puck.

Once the specimens were in the mount it was necessary to grind the surface of the puck to prepare for the polishing process. This helped take off any of the mounting material that may have gotten onto the surface of the specimen that was to be viewed in the SEM. This also helped to remove any defects that occurred during the sawing of the specimen. This was accomplished by rubbing the specimen on a series of four different grit

sandpapers from coarse to fine. Each specimen was rubbed approximately 5-10 times in one direction over sandpaper beginning at a 240 grit sandpaper and then going to a 320 grit, a 400 grit and a 600 grit. Each specimen was rotated by 90° when switching grit so as to remove any grooves made in the previous step.

The next step was the actual polishing step. First, an Allied High Tech Products, Inc, 8-inch, Goldlabel Polishing Cloth was used on a polishing wheel at 200 rpm for each specimen surface. A 6 micron polycrystalline diamond suspension water based solution was placed on the pad. Each specimen surface was applied to this pad for approximately 4 minutes. Next, a Buehler Texmet 2500 8-inch polishing cloth was put on the polishing wheel. The wheel was set a 200 rpm and a 1 micron polycrystalline diamond suspension water based solution was used for the each specimen surface. This process was also done for approximately 4 minutes. These two polishing steps resulted in an extremely clean finish on the surface of the specimens. The next step in preparation is to etch the specimen surface to allow the microstructure of the ceramic to be seen. The specimens were placed in a Vibromat 400-VPS-366. In each machine was a Buehler 12-inch microcloth and an Allied High Tech 0.05 micron Colloidal Silica Suspension. This machine vibrated in such a manner as to move the specimens around in the solution on the cloth for 16 hours. After the specimens were taken out of the Vibromat they were cleaned off to ensure the solution did not cause any additional, unwanted, etching of the material which damaged the microstructure.

The final preparation process is to make the specimens conductive enough to use in the SEM. The first step was to apply silver paste on the surface of the mounts around,

but not touching the specimen. This step would not be necessary if a conductive mounting material was used. The next step is to run single sided copper tape from the silver material on the upper surface down the side of the mount. A dab of silver paste should be used to connect the top of the copper wire to the silver paste on the surface of the mount. Once this has been accomplished the specimens are placed in a Palladium-Gold Sputter Coater for approximately 2 minutes for a coating of roughly 6 microns.

The specimen is now ready to be used in the SEM. A holder which accepts the specimen and mounts is used to place the specimen in the SEM. It is important that the screw used to hold the specimen in place be tightened on the copper tape to ensure maximum conductivity. The specimen is finished and ready to be placed in the SEM. Figure 19 shows the completed SEM specimen.

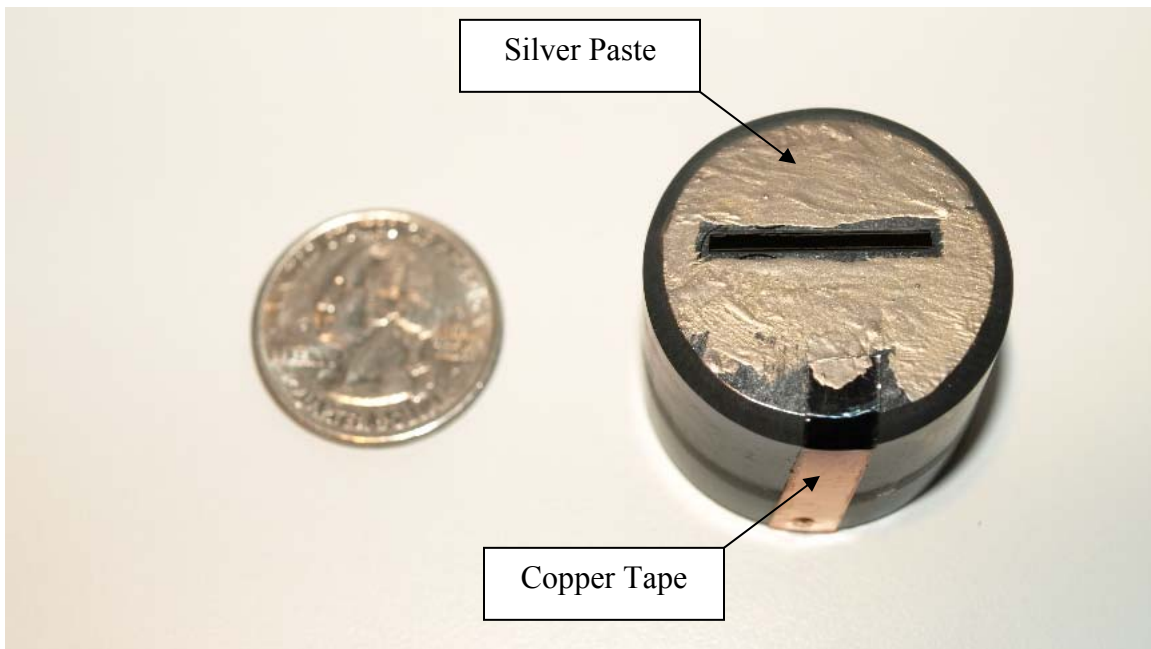


Figure 19: Completed Specimen for SEM

III. Finite Element Application

Motivation

In Reed's dissertation and paper on the evaluation of hard coatings, a method was utilized in which a finite element (FE) model was used to help determine the material properties of a partially coated beam with nonlinear behavior (Reed, 2007). This method will be used in an identical fashion in this work. If the beams were fully coated and the materials linear it would be possible to use Euler-Bernoulli beam theory to determine the mode shape of the beam.

This finite element analysis will not study the characteristics of both the bond coat and ceramic hard coat separately. In the same way the magnets and glue combination were homogenized, the bond coat and ceramic hard coat will be homogenized. When dealing with thicknesses on such a small scale, such as the bond coat, it is difficult to get the ratios for the analysis FE just right. With the bond coat being a very rough surface, it is also difficult to model accurately. Therefore all analysis will be done using a bond coat, ceramic combination. Figure 14 shows this random nature of the bond coat. The large thickness of the ceramic coating relative to the bond coating leads one to conclude that the bond coat doesn't contribute significantly to the material properties of the coating combination.

Technique

To determine the material properties of the coating it was necessary to use both experimental data and finite element data. First the assumption was made that the bare titanium beam performed linearly. This meant that the data from the first mode shape of the beam produced via experimentation could be matched up with the finite element model data. This was important so that the added mass and stiffness associated with gluing on the magnets and the upper support structure could be accounted for in the modeling of the coating. In order to construct a model of an equivalent beam, a set density, calculated using physically measured data, was used in the FE modal analysis while the modulus of the beam, E_b , was changed in an iterative fashion using the ANSYS finite element software modal analysis behavior (Reed, 2007). This iteration (Figure 20) was carried out until the resonant frequency of the beam in the lab matched the frequency of the FE modeled beam to within a thousandth of a Hertz. The beam model is shown in Figure 21 and is comprised of 5632 3-D 8 node elements. The element size at the point of interest (beam center with respect to both length and width) was 1.27 mm X 1.27 mm X 0.8 mm.

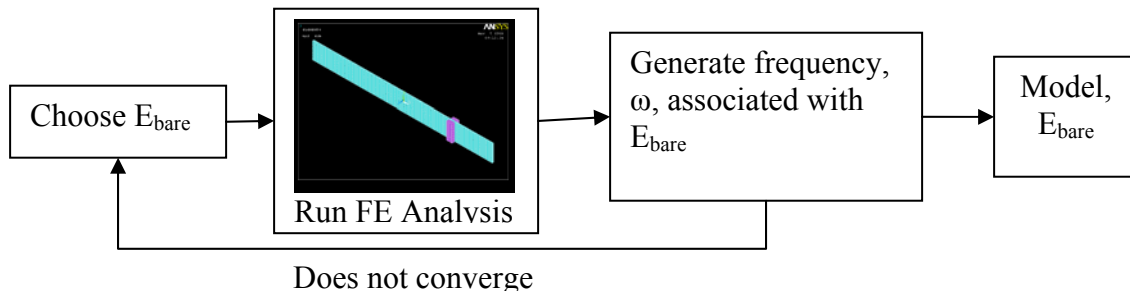


Figure 20: Bare Beam Modulus Iteration

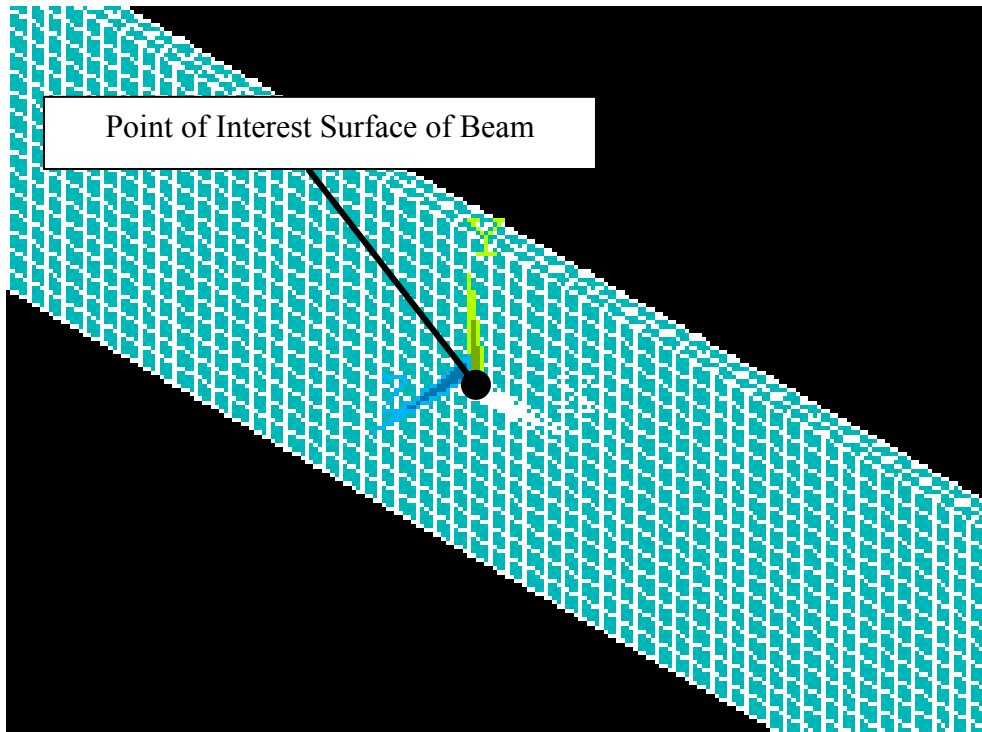
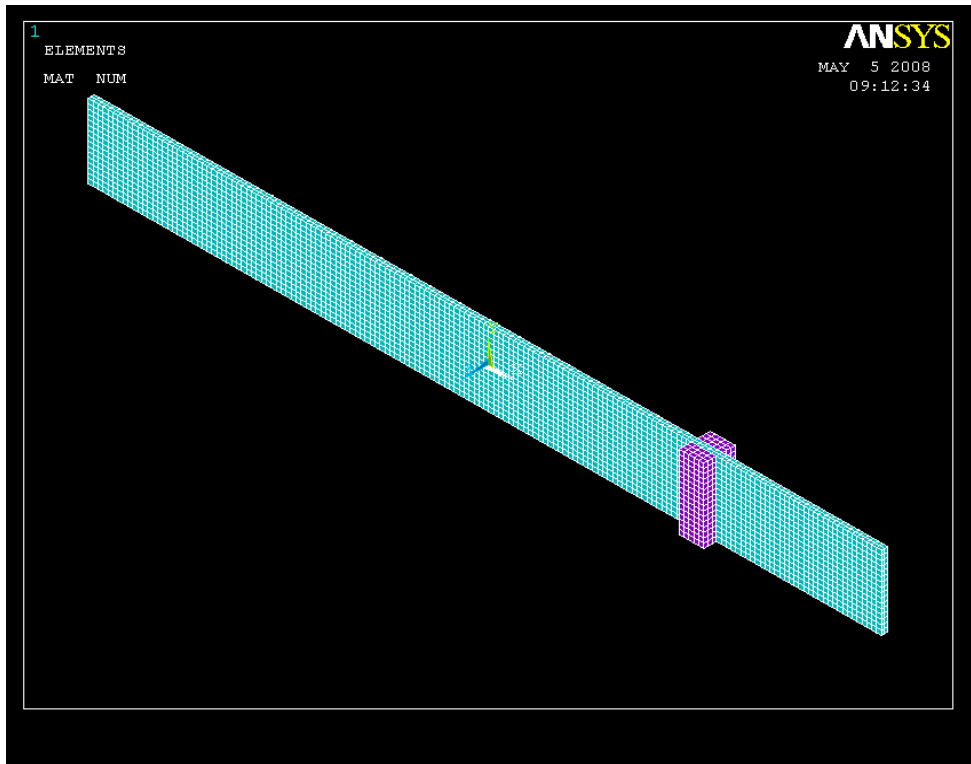


Figure 21: ANSYS Untested Beam and Detail Image

The coating modulus, E_c , could be determined in a similar iterative fashion as the bare beam modulus but, because the coating exhibits nonlinear traits it is necessary to evaluate the finite element model over a wide range of strains and natural frequencies (Reed, 2007).

To do this, it is necessary to evaluate a beam coated with the homogenous mixture of bond coat and top coat for a certain coating modulus value. Forty GPa was chosen as the system modulus for mag spinel as it was the initial value chosen in previous research (Reed, 2007). When the modulus is input into the FE model and modal solution is performed, ANSYS produces several useful values including: mode shape, frequency, normalized reference strain and strain energy. The mode shape, X , was normalized to unity using the maximum beam deflection which occurs at the beam center and calculated through the eigenvector-eigenvalue analysis via ANSYS. The normalized reference strain, $\tilde{\epsilon}$, is the non-dimensional strain calculated at the center of the beam. As done in previous research, these values are determined at the interface between the coating and the titanium substrate. The reference location is shown in Figure 23. Strain energy is calculated in the finite element program by multiplying stress and strain of each element and integrating those values over the entire volume of the model. The strain energy of the system takes into account both the beam and the coating. The strain energy of the coating just takes into account those values associated with the coating. The strain energy ratio (SER) is the ratio of the coating strain energy to the entire system strain energy. This model is comprised of 10640 elements which will be discussed in more detail in a subsequent section.

The first value of importance in this analysis is frequency. The experiment involving various input voltage produces values which fall within a range of resonant frequencies. It is important that the modulus value that is input into the FE model produce a frequency value within the experimentally generated resonant frequency range. If this is the case, all the values output by ANSYS related to that modulus value can be recorded. In this report six modulus values produced data for the mag spinel coating and five modulus values produced data for the YSZ coating. This iteration was done manually by observing the FE results and adjusting the modulus input accordingly. This recorded data will be used to generate a relationship between the experimental natural frequencies and the finite element values of modulus, mode shape, normalized reference strain and strain energy. The process is shown in Figure 22.

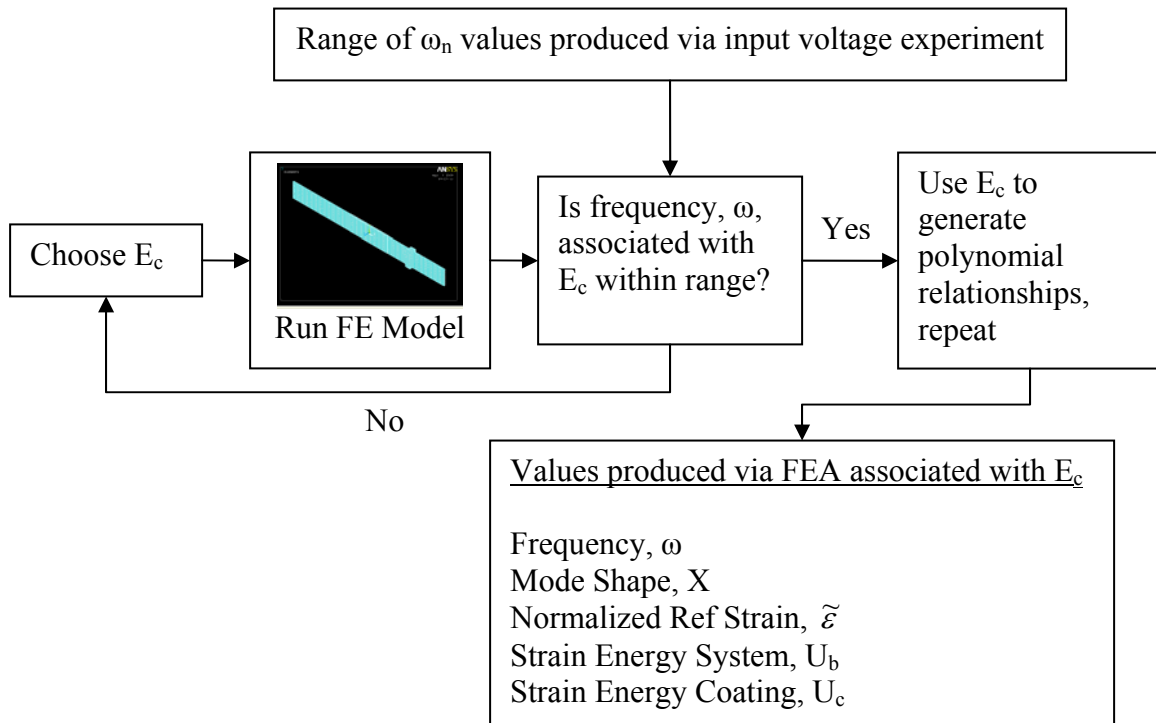


Figure 22: Determine Moduli Values for Polynomial Relationships

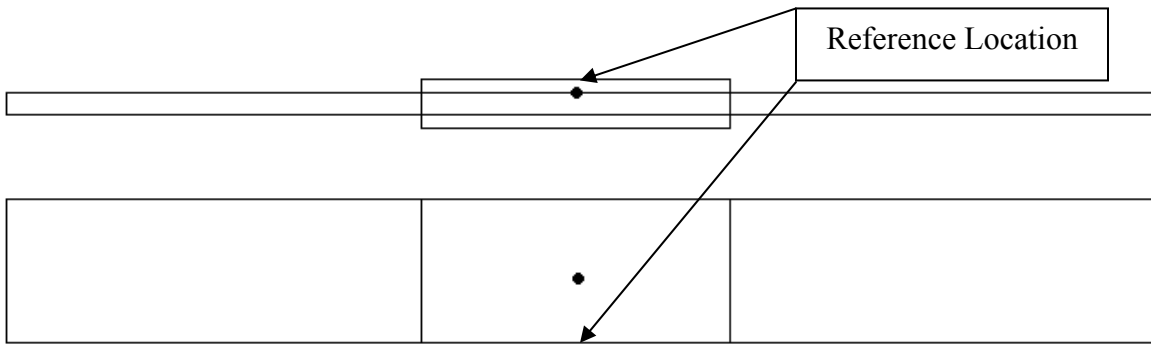


Figure 23: Reference at Interface

After the correct coating modulus values have been determined, it is possible to generate four polynomial relationships. These relationships are: coating modulus vs. frequency; coating modulus vs. SER; coating modulus vs. normalized reference strain; and coating modulus vs. normalized displacement at the center of the beam. For each value of coating modulus used in the FE model, one point will be able to be used for each relationship mentioned. Once all the points have been plotted, a polynomial curve fit should be performed on the points to generate equations. These equations will be used in the next step to relate FE data to experimental data. The equations were produced using the trendline function in Microsoft Excel. A higher order polynomial, 4th or 5th, equation could have been utilized in this test, but the use of a polynomial of that high of a degree would have led to data that would have been poorly conditioned. Therefore it was decided to use second order equations. Figure 24 shows the steps taken to generate the four equations used in the upcoming section.

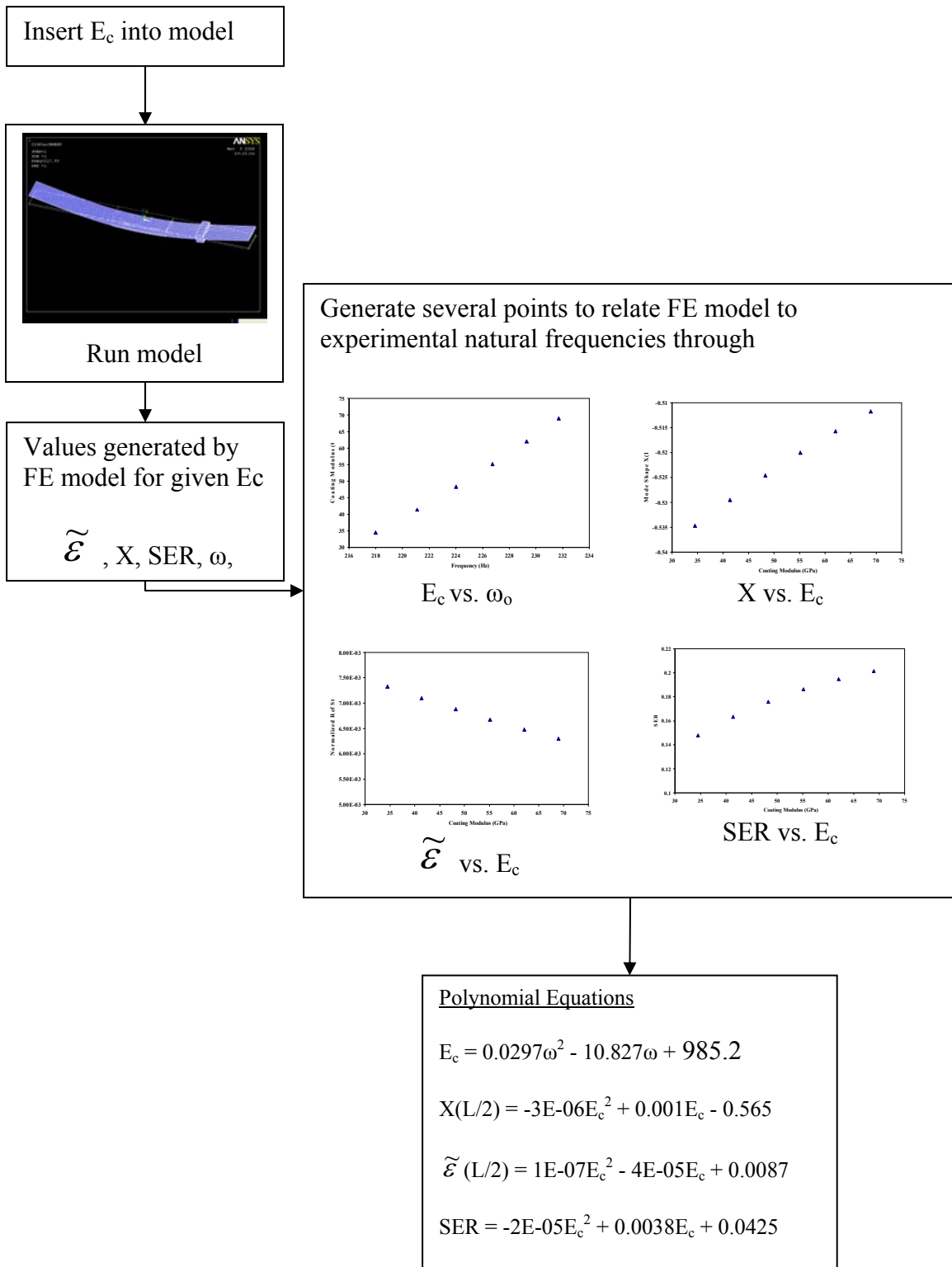


Figure 24: Polynomial Progression

Once the four second order polynomial equations have been generated, it is possible to generate material property data that is a product of experimental and finite element data. The first step is to use the data points that were generated experimentally by the input voltage test. Each of these 18 points is a resonant frequency at a maximum velocity. The next step is to insert the frequency value of each of these points into the equation which relates coating modulus to frequency. This step results in 18 coating modulus values that are directly related to experimental velocity. With this relationship established, the 18 resultant modulus values can each be directly applied to the remaining equations produced in the previous step. This results in 18 values of SER, normalized reference strain and beam displacement that can be related to experimental velocity. The process is shown in the chart in Figure 25.

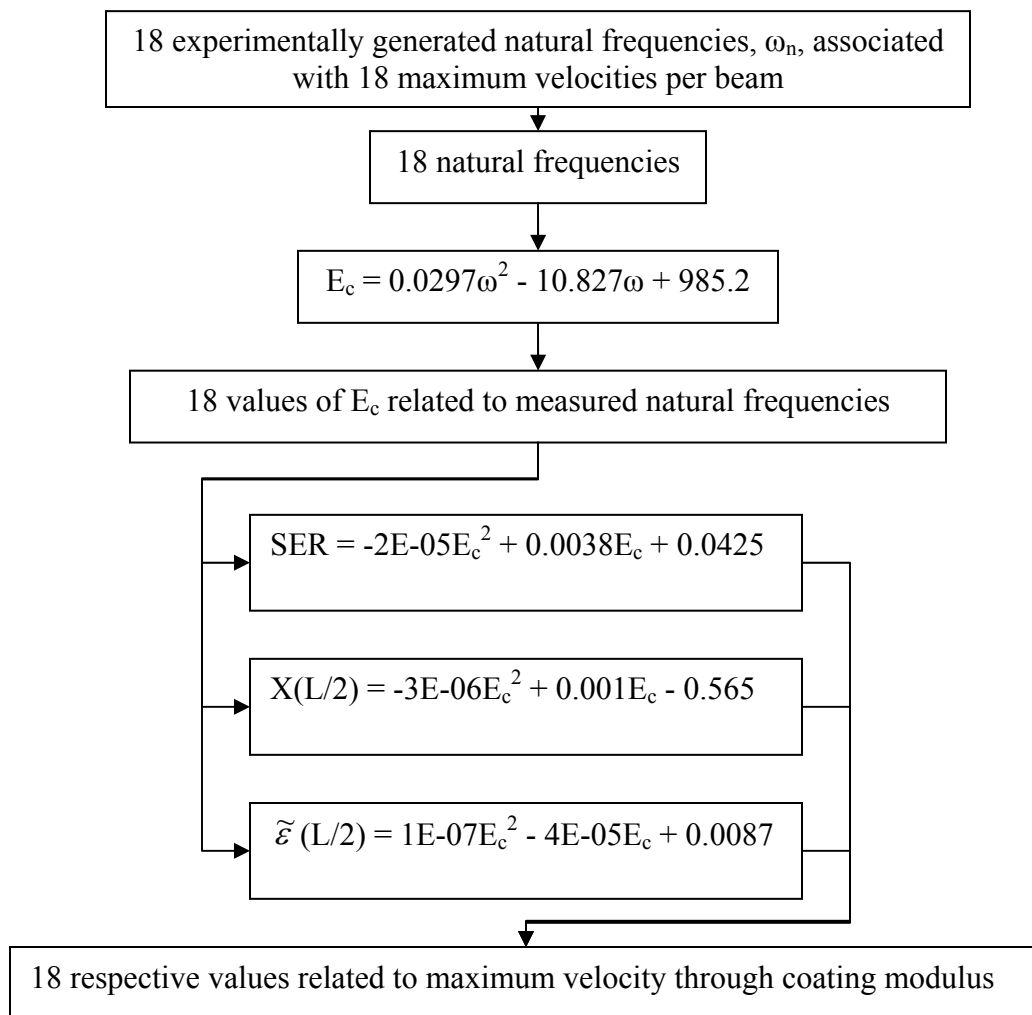


Figure 25: Measured Data in Relation to Finite Element Data

Now that each value of experimentally measured velocity is related to a particular value of SER, coating modulus, normalized reference strain and mode shape it is possible to determine how the material properties vary due to actual strain. This is done by first determining a scaling factor, λ . The scaling factor is a value that is multiplied by a finite element value and results in a physical value. Two values that have already been calculated and are related by the scaling factor are mode shape, X, (FE produced) and

displacement, δ (experimentally produced). 18 points (the velocities and related resonant frequencies for each voltage input) have been generated for each beam experimentally, via the input voltage test, and each value can be related to the FE model using the expression:

$$\lambda = \frac{\delta}{X} \quad (7)$$

It should be noted that to obtain the correct scaling factor it is necessary to have the correct units of displacement and mode shape. It is important that the frequency term used to calculate the displacement value, δ , is multiplied by 2π if frequency is in Hertz (Equation 5).

Once 18 scaling factors have been determined, they can be used to relate the normalized reference strain to the actual reference strain. This strain is considered a reference strain as it is determined in reference to the point located between the coating and titanium beam. The 18 scaling factors can be multiplied by the 18 normalized reference strains generated through the FE model using the relationship:

$$\varepsilon = \lambda \tilde{\varepsilon} \quad (8)$$

At this point, the physical strain is related to the measured velocity. But one more step needs to be taken so that all the material properties can be related to strain.

The last value that needs to be determined is the loss factor associated with the coating, η_{coat} . The first value that is needed to determine the coating loss factor is the strain energy ratio (SER), which has been determined previously. Two other factors that have been determined and that can be used in calculating the coating loss factor, via experimentation, are the system loss factor, η_{sys} , and the bare beam loss factor, η_{bare} . At

low to moderate strain values (up to approximately 1000 $\mu\epsilon$), the bare beam loss factor was determined to be constant, .0008, at all strain values (Figure 26).

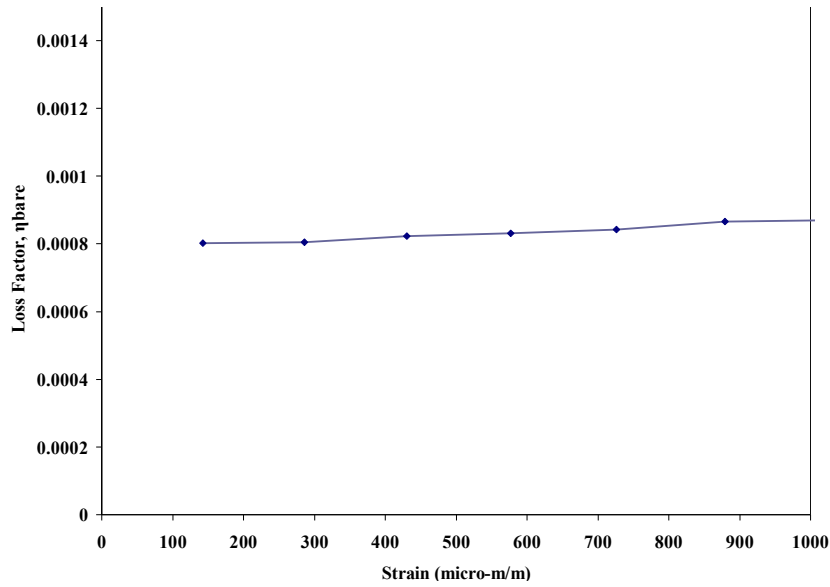


Figure 26: Bare Beam Loss Factor

The assumption of a constant value is needed to determine a coating loss factor. The reason for this assumption is that at a given strain value there must be a system loss factor value and a bare beam loss factor value. Since the bare beam loss factor is assumed constant at all strain values, any system loss factor value can be related to bare beam loss factor regardless of strain. Therefore, Equation 9 can be utilized to determine the coating loss factor (Torvik, 2007). Each value of SER, system loss factor and bare beam loss are related for a common strain value and in turn the coating loss factor is also related to that strain value.

$$\eta_{coat} = \frac{\eta_{sys}(SER + 1) - \eta_{bare}}{SER} \quad (9)$$

Now that each coating loss factor, coating modulus, and strain are related to the same maximum velocity values it is possible to put all the material properties into terms related to strain as is shown in Figure 27. This Figure is an example shows how the values of coating modulus and loss factor are finally compared to strain using two relationships which had been determined in previous steps.

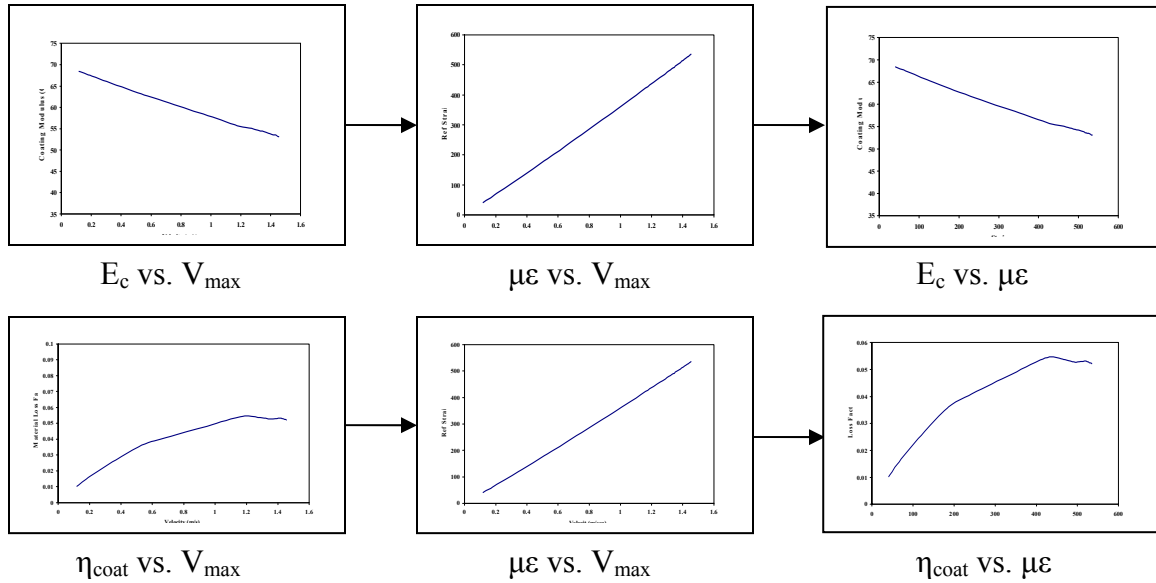


Figure 27: Material Properties in Relation to Strain

defined to be the coating modulus multiplied by the loss factor.

$$E_2 = E_{coat}\eta_{coat} \quad (10)$$

This process has been done to a number of beams in order to determine the material properties. In Chapter IV, the relationships for the actual modeled beam will be shown along with results.

It is important to note here that at least two sources of error may have been introduced into the test. The first source of error came when designing the finite element

model. Damping was not explicitly included as an input. The following equation shows the typical relationship between: displacement as a function of time, U ; damping, C ; stiffness, K ; and mass, M .

$$M\ddot{U} + C\dot{U} + KU = 0 \quad (11)$$

In the finite element model for this test the damping value, C , was neglected. At this point in the characterization of the ceramic coating it is hoped that this test setup will help to determine the damping associated with the TBCs. In the future the results generated from this test could lead to an iterative solution of the damping characteristic which could be related to the experimental loss factor value, η , via the relationship shown in Equation 3. We would like frequency as a byproduct of a damping ratio. The only way damping can be included into the model would be to use the FE program NASTRAN. Unlike most finite element software, this software is capable of utilizing nonlinear damping properties.

Another source of error comes from the fact that the beam finite element properties have been calculated with respect to the interface between the coating and the titanium. These results have been related to experimental data. The problem with relating the FE data to the experimental data is that the LDV measures the velocity at the coating surface and not the velocity at the interface of the coating and the titanium. It is likely that the velocities at these two points would vary, if only by a small amount. As these velocity measurements lead to displacement measurements, and because the displacement calculations are used throughout the analysis, a small error in velocity could be compounded as the displacement values are used in other calculations.

IV. Results and Discussion

The purpose of this section is to tie together the results generated in the experimental phase of the project with the results of the finite element portion of the project. The results that have been generated should characterize the homogenized coatings of magnesium aluminate spinel and yttria stabilized zirconia (YSZ). The coatings were homogenized for the reasons presented in a previous chapter. This section will progress from the bare beam data results to the results for the homogenized coatings. The discussion will also include the experimental results, followed by the finite element results and will conclude with the characterization of the material properties of the two coatings. After that the mag spinel results will be compared to the results generated by Reed behavior (Reed, 2007). Next, the results of mag spinel and YSZ will be compared to each other to determine if the coatings exhibit similar characteristics. Finally, the microstructure of the two coatings will be examined.

Bare Beam Results

The establishment of the bare beam characteristics is important in setting a foundation for the proceeding analysis. Both down sweep (sine sweep from high to low frequency) and up sweep (sine sweep from low to high frequency) are shown to illustrate the importance of sweep direction. Looking at Figure 28, which utilize down sweeps, one sees the curves growing larger and the maximum frequency getting lower as input voltage is increased. This corresponds to an increase in loss factor. In Figure 29, which show up sweeps, the figures are all roughly the same shape and display a more gradual frequency loss. That shows that the sweep direction has a significant impact on the results, and the titanium beam displays nonlinear behavior. This behavior is more than likely a result of the test setup, as titanium is assumed to be a linear material.

Figure 28 illustrates a source of error that is a result of using the half-power method. As the recorded data indicates a slight softening, the curves produced via experimentation are not symmetrical about the resonant frequency. The curves should be narrower (have less damping), especially the ones generated at the higher input voltages, than the curves that were produced. Therefore, loss factor values generated via Figure 31 are not a constant value and increase at higher input voltages. The true loss factor should have a relatively constant value for all input voltages.

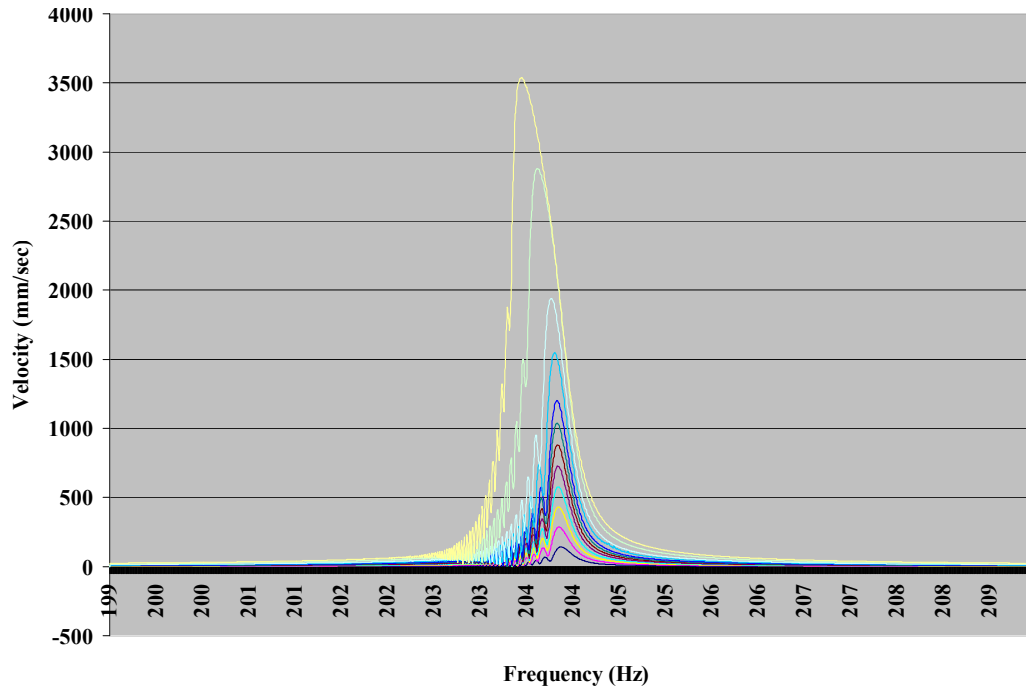


Figure 28: Bare Titanium Bar in Vacuum Sweep Down FRF

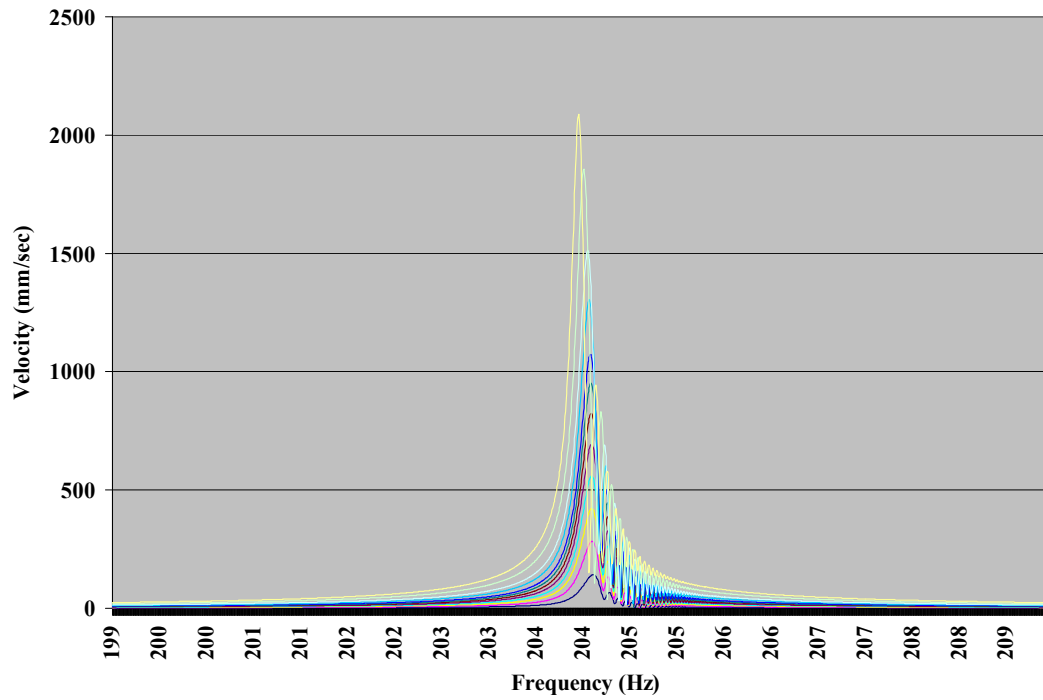


Figure 29: Bare Titanium Bar in Vacuum Sweep Up FRF

It was reported that a significantly reduced loss factor for a bare beam, as well as a relatively constant loss factor, could be obtained by measuring the beam response inside of a vacuum when tested using the free decay test method (Reed, 2007). In the dissertation the beginning loss factor was significantly lower (250%) inside the vacuum than at atmosphere. Additionally, the loss factor remained at a constant value at all velocities inside of the vacuum (Figure 30). The beam in this study behaved more like the beam outside of the vacuum in the previous study. This could be an indication that the test setup introduces some nonlinear traits. It could also indicate that since the half power bandwidth method is intended for linear systems that the log decrement method is more suitable for this study.

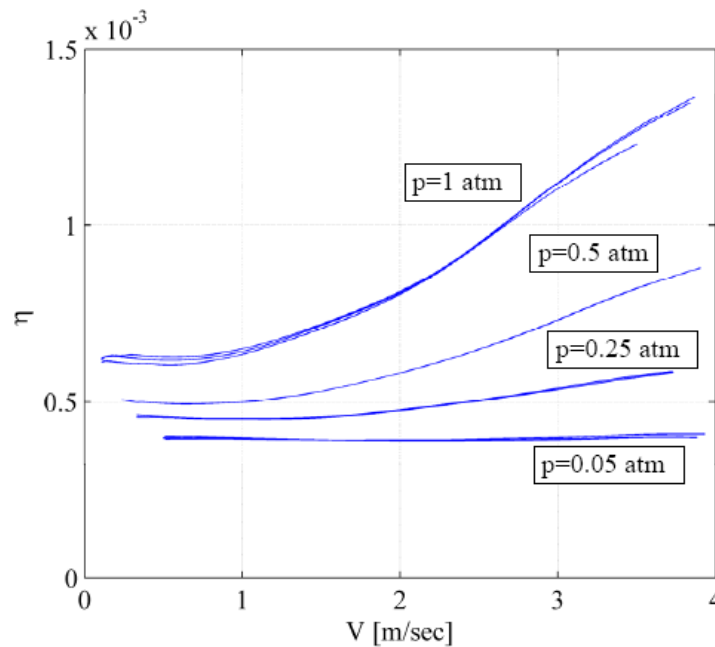


Figure 30: Bare Beam Loss Factor In a Vacuum Using Free Decay (Reed, 2007)

The vacuum in this study kept the value of bare beam loss factor relatively constant up to a strain of $1000\mu\epsilon$ and then the loss factor value began to increase (Figure 31). This

indicates that air damping is a factor, if only at high strains, even in a vacuum chamber. This could be a source of error.

Figure 31 and Figure 32 display the results that were used in the characterization of the bare beam for this study. These Figures show how the titanium beam behaves in the vacuum when measured using the half-bandwidth method. The beam displays the characteristic of a system that increases damping as strain increases. This was not the case with Reed's beam in the vacuum. In that study the strain had no effect on the damping for the beam inside the vacuum chamber. The Figures also indicate larger damping values compared with the dissertation. The loss factor value reported in that beam at $500\mu\epsilon$ was 0.0004 while the loss factor in this beam in a vacuum at the same strain was 0.0008 (Figure 31), which is twice the damping (Reed, 2007). This discrepancy may be a result of the vacuum having a small leak. This low damping value of 0.0008 is a good indicator that the true damping values of the coating can be determined. Another assumption for this study is that the titanium beam behaves in a linear fashion. While there is some apparent softening it will be assumed the beam is linear for the remainder of the calculations as the beam maintains a relatively constant frequency at all velocities (Figure 32). This assumption is especially accurate for velocities up to 1.5 m/sec. The importance of this assumption will be apparent when the finite element model is generated.

Since the value of the bare beam loss factor was determined using the half-bandwidth linear method and the value in a previous study was determined using a free decay method, it was decided to determine what the percent difference in coating loss

factor would be between using the values generated using the two methods. The free decay method determined a constant value of 0.0004 while half-bandwidth method determined a semi-constant, as seen in Figure 31, value of 0.0008. Because a titanium beam in a vacuum should have a loss factor approaching zero for all strains it was decided that the free decay method of measuring bare beam loss factor data should be used. The reason being, the loss factor calculated via the free decay method is half that of the value calculated using the half-power method. The difference may be primarily due to the half-power method being a linear method and the data being nonlinear. A calculation has been carried out to determine the coating loss factor at each bare beam loss factor value. This calculation was done for each value of bare beam loss factor computed using the two methods using the equation:

$$\eta_{coat} = \frac{\eta_{sys}(SER + 1) - \eta_{bare}}{SER} \quad (9)$$

The result of the calculation was that the loss factor for the coating alone is, on average, 5.6% higher when using the free decay bare beam data. This difference may be due to a small leak in the vacuum chamber. The reported vacuum pressure in the previous report was 20 mm Hg while the usual pressure for this report was 25 mm Hg. The difference in the data shows that the free decay method may be better suited for determining the bare beam loss factor.

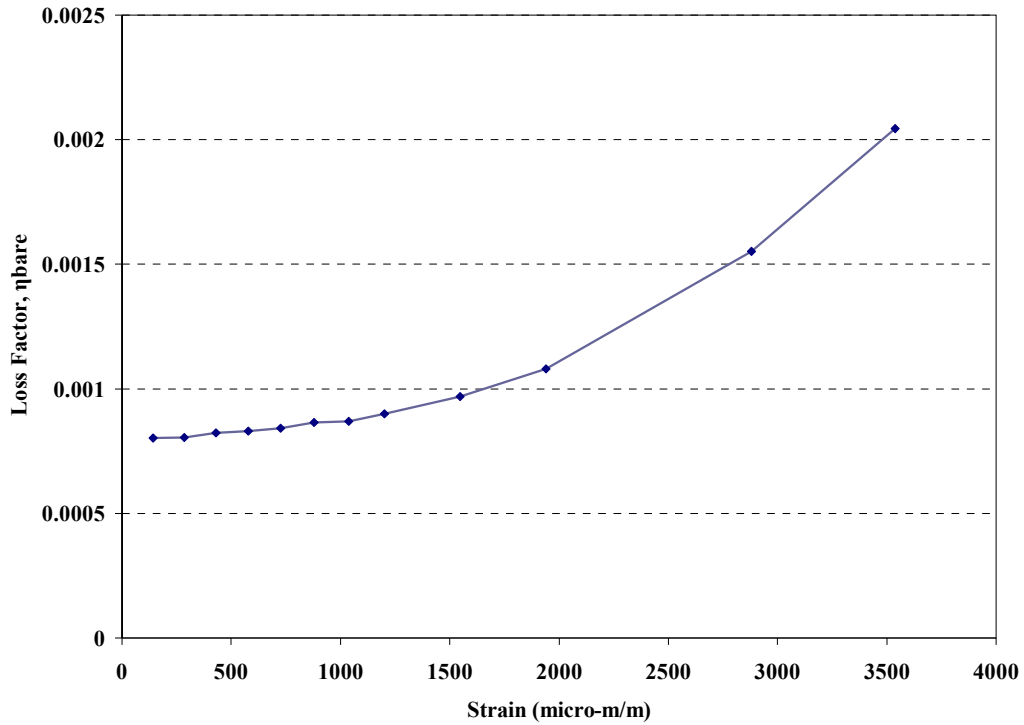


Figure 31: Titanium Beam Loss Factor in Vacuum

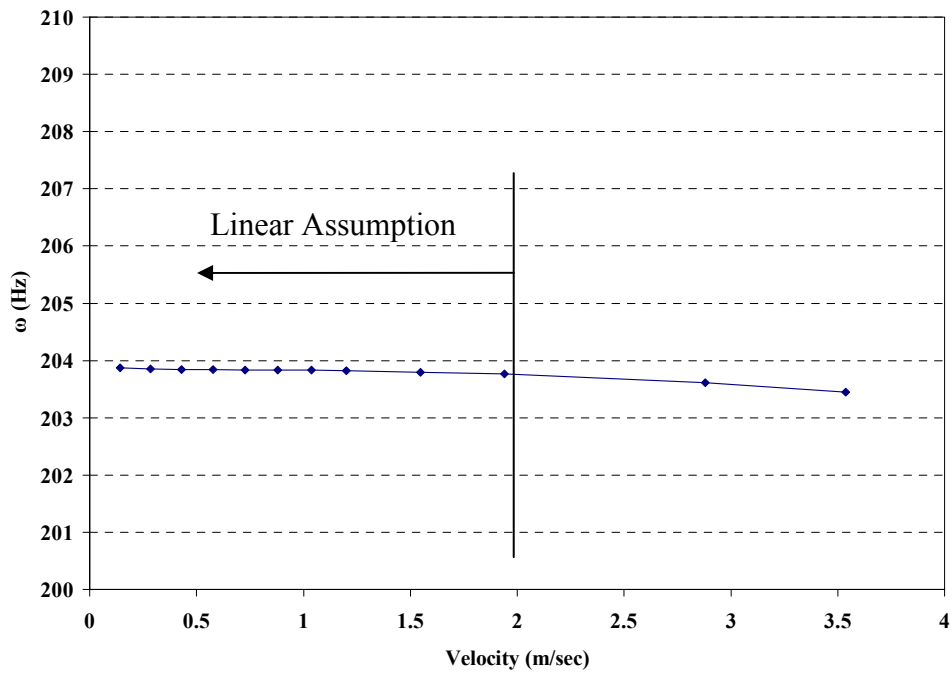


Figure 32: Titanium Beam Resonant Frequency in Vacuum

As a result of the curves produced in this section, it is important to note that the assumptions made for the titanium beam could add additional error to the results. The bare beam showed a slight softening in terms of frequency and did not maintain a constant value for loss factor as has been pointed out. The reason this beam did not exhibit these linear characteristics could be because the free-free test setup was used. In any case the data is mostly linear at measured velocities below 2 m/sec and strains below $1500\mu\epsilon$.

Homogenous Coatings

This section will deal with the beams coated with a coating combination of either NiCrAlY and mag spinel or NiCrAlY and YSZ. The results of the analysis on both coatings will be presented but the process of determining the material properties will use the data generated for the mag spinel-NiCrAlY coating combination.

History Effects.

In the description of the testing process it was stated that the beam will be subjected to a certain amount of cycles in order to observe the history effects of the coatings. This task was handled through the VibrationVIEW software. The beams were excited to a velocity of 2.2 m/sec, as previously stated, and held at that velocity for a set amount of cycles using the software control. These resonant frequencies were recorded via a sine sweep, as described in the experimental techniques section, from high

frequency to low frequency at set intervals throughout the break in period according to Table 2.

As can be seen in Figure 33 each beam coated with mag spinel undergoes a decrease in resonant frequency, within the first 400,000 cycles. Each point in the Figure was generated by experimental data. After the initial frequency decrease, it can be seen by the increase in resonant frequency values that, the material increases in stiffness, almost linearly, until the conclusion of the test at 4,000,000 cycles. The initial stiffness that was lost was regained by 1.5 million cycles with the ending resonant frequency no less than 2 Hertz higher than the initial frequency. Each point was generated by conducting a sine sweep according to the schedule in Table 2.

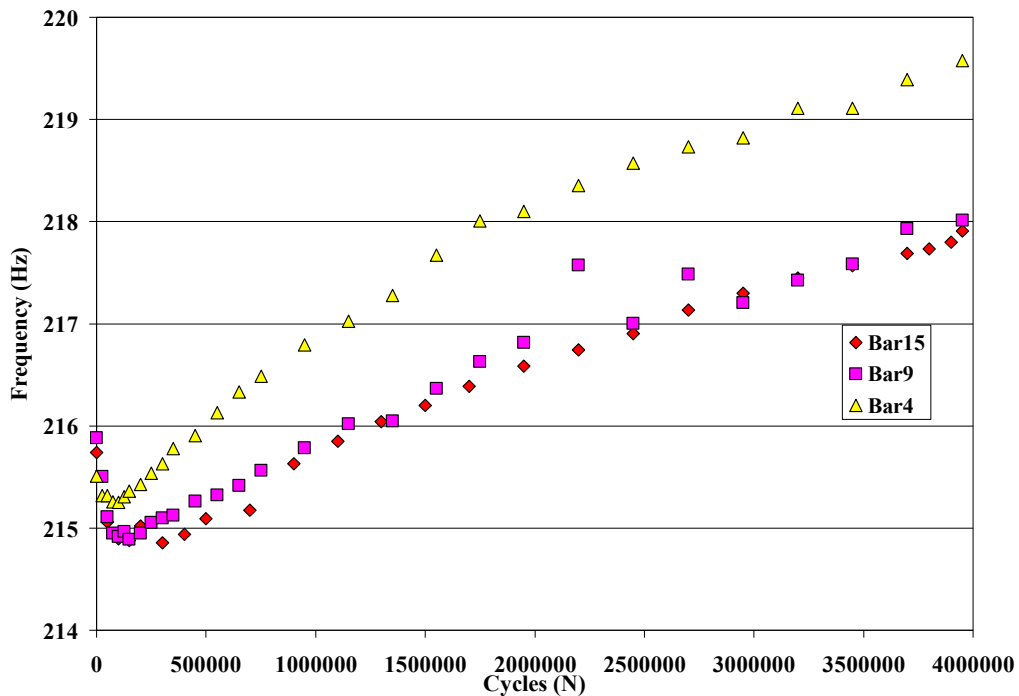


Figure 33: Resonant Frequency Change due to Cycle Buildup for Mag Spinel Beams

Figure 34 shows the system response to input as the number of cycles is increased. Again, each point was determined experimentally. The Figure shows that the accumulation of cycles causes the beam to respond with less and less velocity magnitude. This leads one to conclude that the material increases in damping as the material is cycled at a resonant frequency and that the response is related to stiffness. This is not true within the first 250,000 cycles as the beam responds with increasing amplitude. Again, this initial trend could be a result of the beam not being broken in during the first portion of the test.

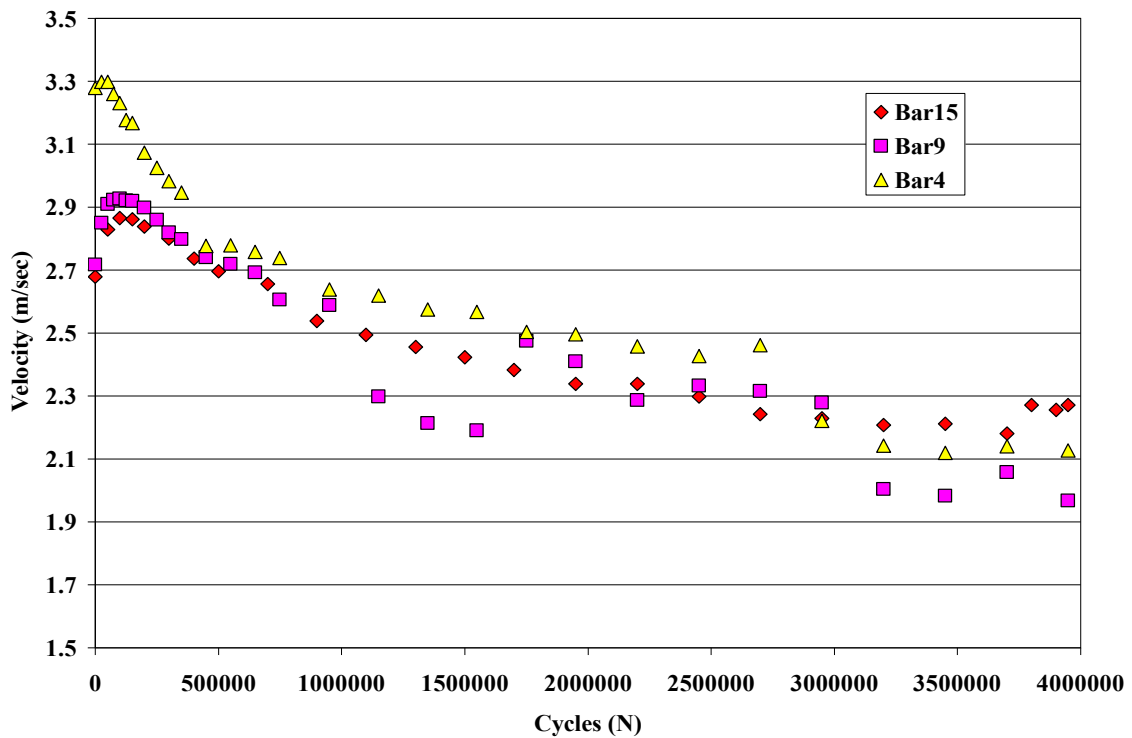


Figure 34: Mag Spinel Response to Input with Cycle Buildup

It appears that the mag spinel specimens never reach a stabilized, equilibrium condition. This means that cycles were still required to get the beam to respond with a

constant velocity and a constant frequency. It will be shown that the other material studied, YSZ, does reach a stabilized state. In the following sections where mag spinel is studied the results may be questionable. As the data in Figure 33 and Figure 34 show, the beam response will continue to change as cycles accumulate. This change could be evident in the data that is produced in subsequent sections. Only after the material has reached steady state will the data accurately show the material behavior without the influence of cycle accumulation.

Figure 35 and Figure 36 show how a yttria stabilized zirconia (YSZ) and NiCrAlY bond coat beam responds to an input over several million cycles. All three YSZ beams analyzed in this chapter were broken in to 4 million cycles. Only one beam was controlled properly and could provide useful data on the resonant frequency response associated with cycle accumulation. The first two beams coated with the YSZ combo were sent through the cycle build-up sequence utilizing a sine sweep that went from low to high frequency. This resulted in uncharacteristic behavior and could not be reported as entirely reliable. It was later discovered that the VibrationVIEW software was incorrectly programmed and was requesting a beam response instead of inputting a voltage for the sweeps between cycle accumulation steps. This resulted in an incorrect beam response. After the control issue with VibrationVIEW was discovered the proper corrections were made (controlling the input voltage instead of the beam response for the sweeps) and the final beam was tested in the proper sweep down manner. The data reported for this beam is done so with a high degree of confidence.

Figure 35 shows that the initial frequency drop that occurred in the mag spinel coating also occurs in the YSZ coating. The main difference in the data being that the YSZ frequency seems to reach an equilibrium frequency at 2.5 million cycles.

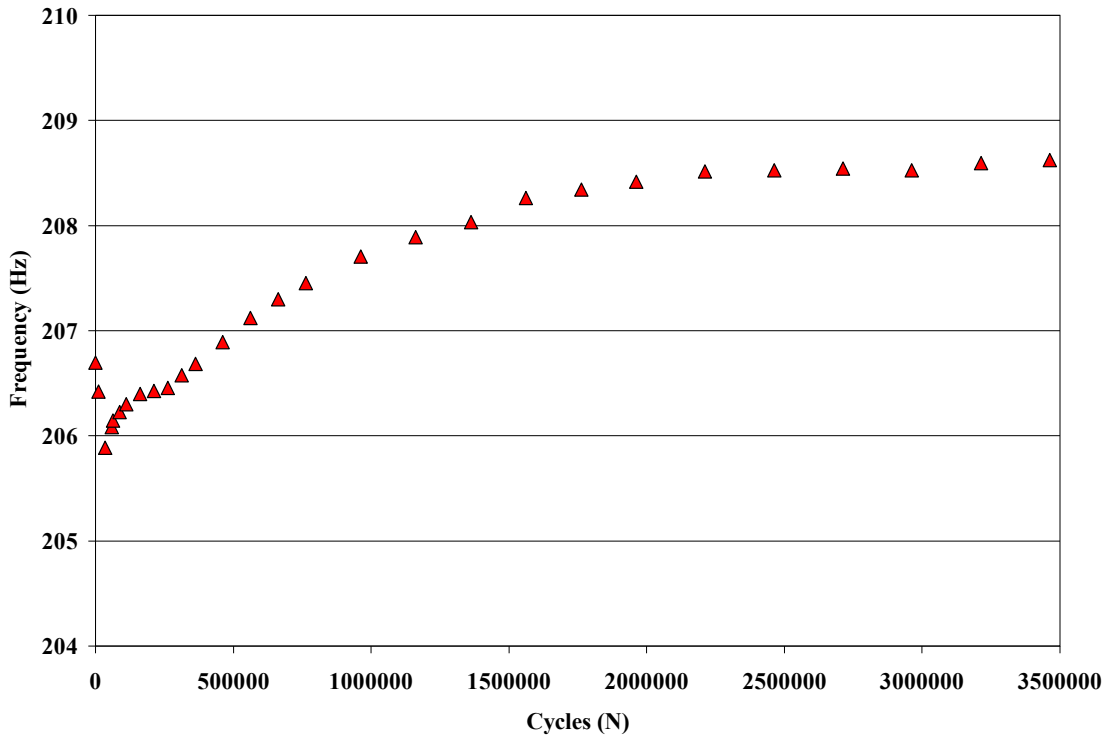


Figure 35: YSZ Resonant Frequency Change

This material also causes the beam to respond with decreasing amplitude as the cycles accumulate; YSZ seems to reach a steady minimum velocity response much faster than mag spinel, 2.5 million cycles. The similar trends seen in the cycle build up will be investigated in a following section. It is assumed that both hard ceramic coating possess similar traits that may be characteristic of all hard coatings.

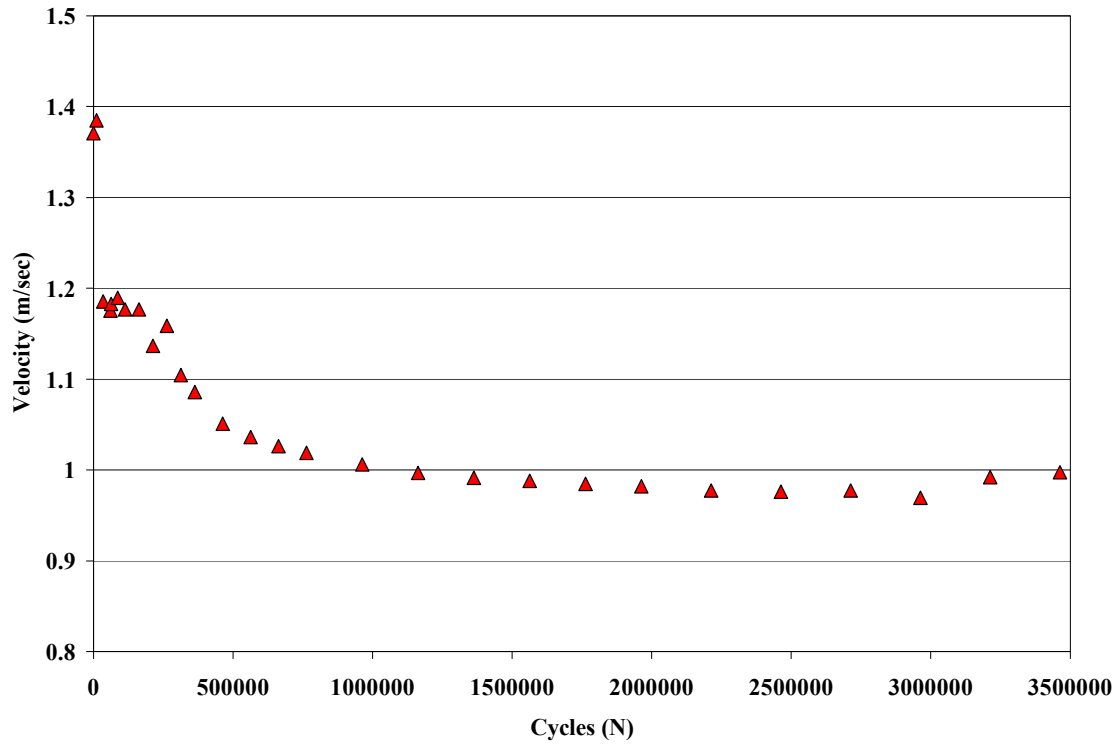


Figure 36: YSZ Response Magnitude Change

Sweep Rate.

The sweep rate utilized in the forced response investigation is an important factor for the accurate recording of data. The sweep rate in this report is the number of minutes it takes to sweep across a set range of frequencies. If the frequency range of the beam is swept through too fast the transient response of the system will be recorded. The recorded data would not generate an accurate picture of the beam/coating system. It is necessary to sweep at a rate that lets all transient responses (both geometrically and materially) decay so the response recorded is considered steady state.

The five sweep rates analyzed were 20 Hz/min, 10 Hz/min, 5 Hz/min, 2 Hz/min and 0.5 Hz/min for one beam coated with mag spinel. The range takes into account rates

that are both considered excessively quick and excessively slow. Ivancic has reported that the maximum sweep rate should be calculated according to Equation 12 (Torvik, Patsias, and Tomlinson, 2001).

$$S_{\max} = \frac{\pi f_0^2}{MQ^2} \quad (12)$$

Where S_{\max} = Maximum Sweep Rate (Hz/min)

f_0 = resonant frequency (Hz)

Q = quality factor

M = number of time constants

The sweeps were conducted by increasing input voltage after each sweep utilizing the VibrationVIEW software. The sweeps occurred in rapid succession, from low input to high input, with a 10 second voltage ramp up at the beginning of each run. This test was performed for 12 input voltages. This 10 second ramp up allowed the input to gently reach the desired voltage and reduced the shock that would be associated with instantaneously applying the entire voltage. Figure 37 shows the effect of the sweep rate on the coating modulus. All the data points are within 5% of each other. Figure 38 shows the effect of sweep rate on the loss factor. All data points are also within 5% of each other.

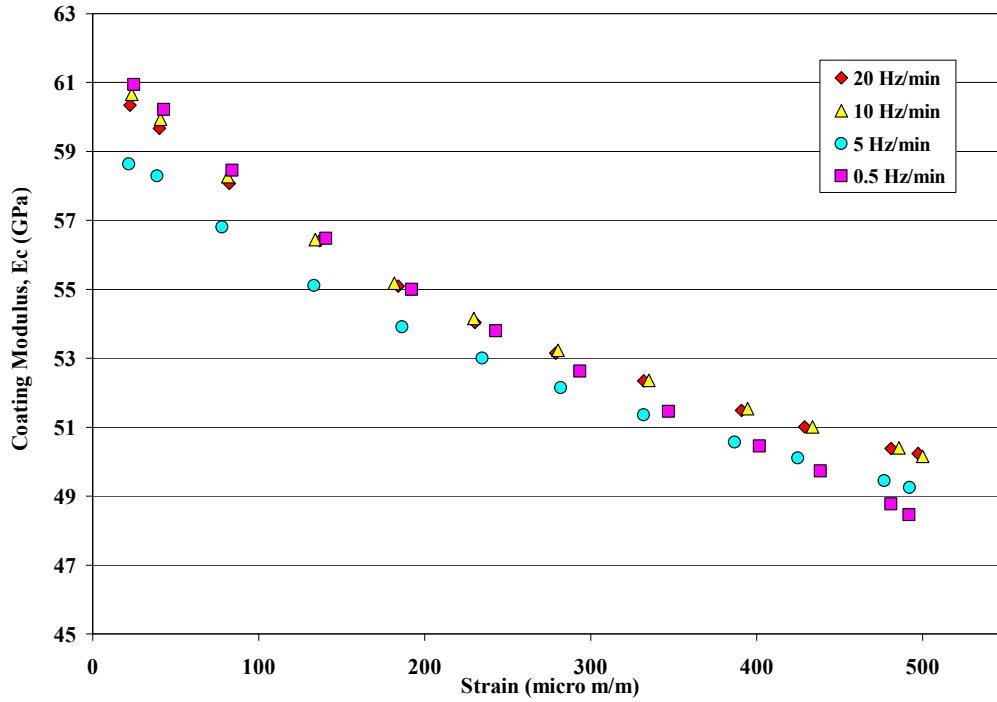


Figure 37: Sweep Rate Comparison for Coating Modulus

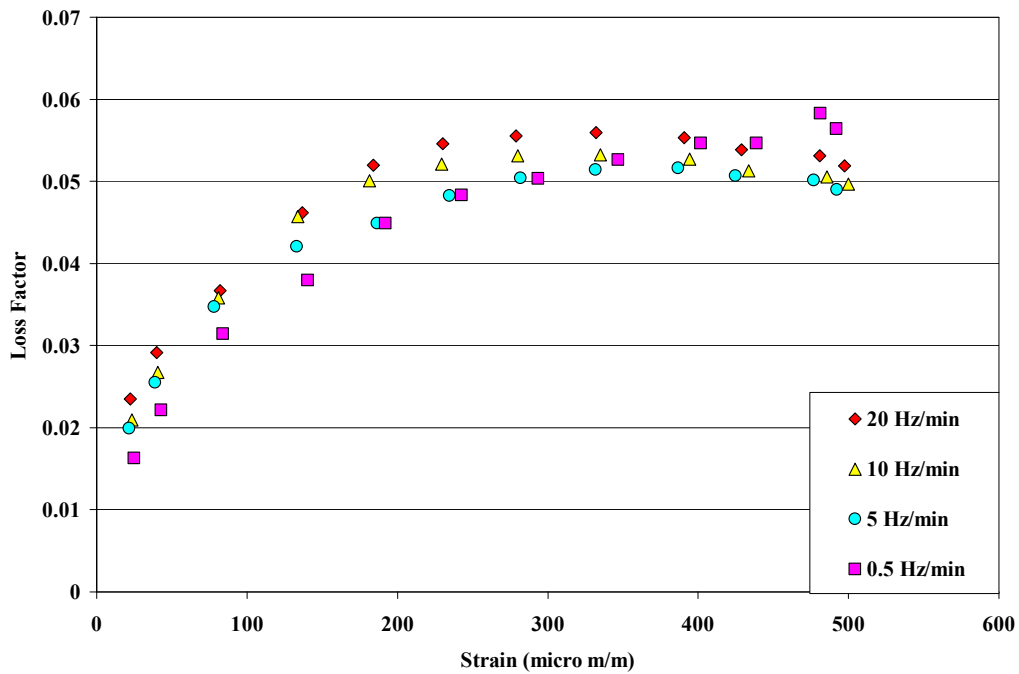


Figure 38: Sweep Rate Comparison for Loss Factor

At this time the process that was used to generate the sweep rate data will be discussed. The first points generated were the points for 0.5 Hz/min and 5.0 Hz/min. Each rate test was conducted one after another. To begin with, an initial input test of 5 Hz/min was run. This result is indicated in figures Figure 39 and Figure 40 and was omitted from the previous two graphics. This sweep lasted approximately 24 minutes. At the conclusion of that sweep the 0.5 Hz/min sweep was conducted. This test lasted 240 minutes. This resulted in coating modulus values that were much lower than the values recorded for 5 Hz/min. The loss factor data generated indicates fairly similar results. Immediately after the 0.5 Hz/min test a 5 Hz/min test was ran to see if any changes had taken place in the material due to use. This test lasted 24 minutes and resulted in even lower coating modulus values and different loss factor values. In the case of the coating modulus it can be seen that the values for all three sweep rates begin to converge at higher strains (above 400 $\mu\epsilon$). For the loss factor the values associated with the initial 5 Hz/min sweep and the 0.5 Hz/min sweep maintain similar values while the set of data associated with the second 5 Hz/min sweep only converges between 200 $\mu\epsilon$ and 300 $\mu\epsilon$. This is thought to be a result of the material not reaching steady state during the cycle buildup portion of the test. The day after this sweep were run it was decided to run the test at 20 Hz/min and 10 Hz/min. The beam was initially put through a 5 Hz/min sweep much like the day before. This data was not recorded. Then the sweeps were run at 20 Hz/min and 10 Hz/min consecutively. For the coating modulus the data lines up well with the 0.5 Hz/min data up to strains of 400 $\mu\epsilon$. The data begins to diverge after that point. The loss factor data also does not correlate with the previous data points.

The random data produce through the sweeps indicates that the mag spinel material is history oriented. This means that the results that are generated are directly a result of the work already done on the material. The results do not indicate that a definitive answer can be made in relation to the effect sweep rate has on the generated data. A source of error has been presented in this analysis. There is not enough information to say that a certain percentage of error is added to the results. The difference in sweep rate will result in a difference in frequency which will ultimately lead to a difference in the modulus of the coating.

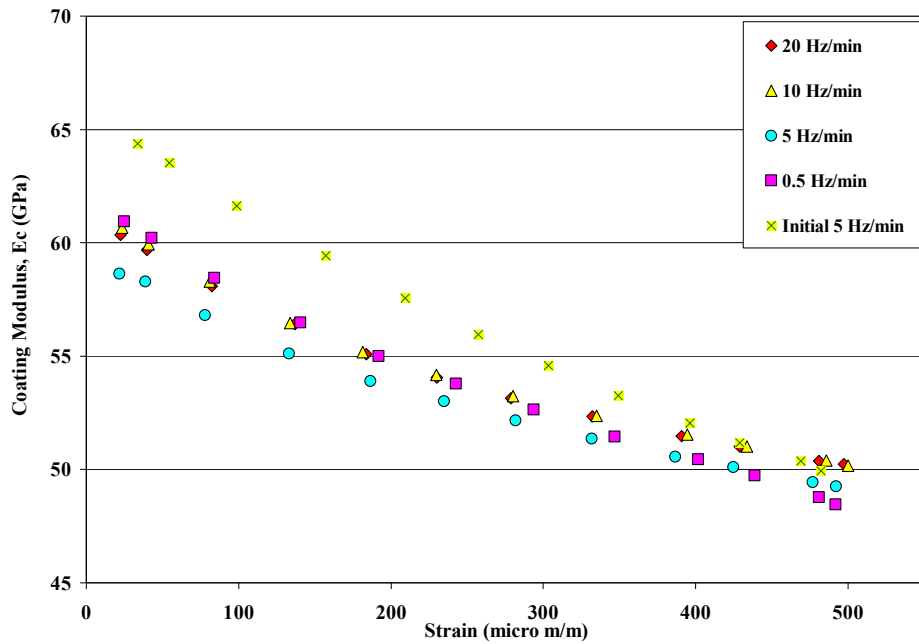


Figure 39: Sweep Rate Effect on Coating Modulus with Initial 5 Hz/min Sweep

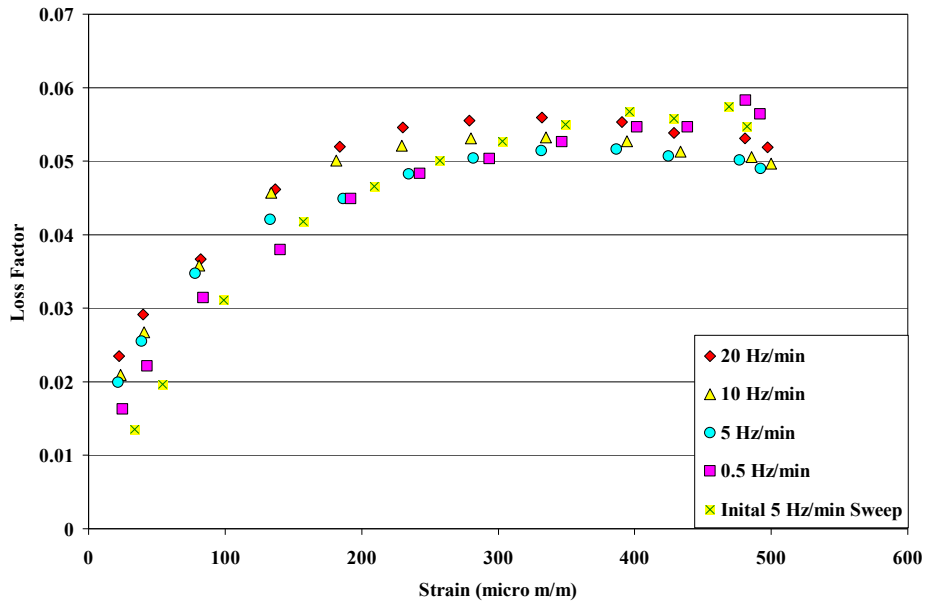


Figure 40: Sweep Rate Effect on Loss Factor with Initial 5 Hz/min Sweep

It was decided that the sweep rate of 2 Hz/min would be used to record all sweep data in the input voltage tests and the sweeps conducted during cycle build up. In relation to the sweep rates investigated the data falls within 10% of all points (Figure 41).

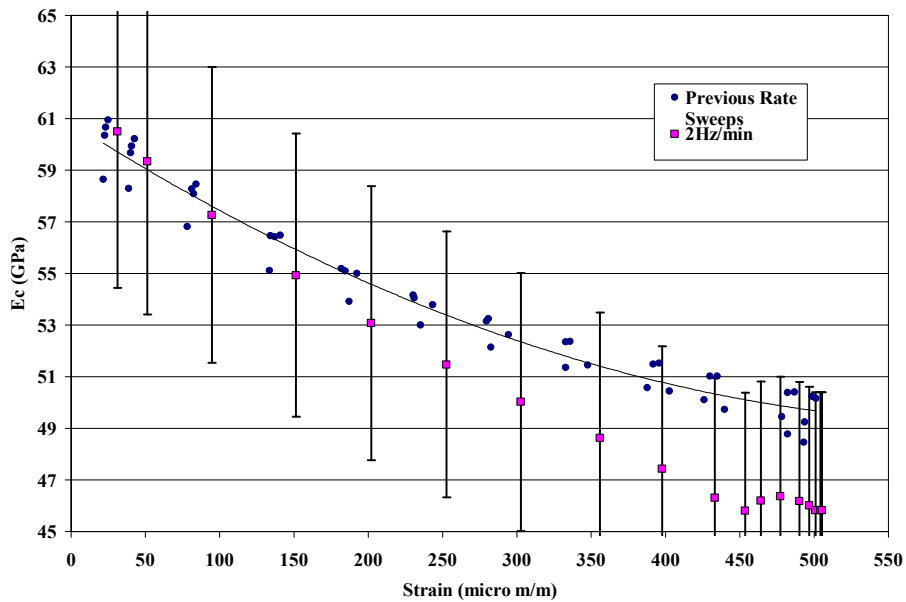


Figure 41: Chosen Sweep Rate Compared to Other Rates

Input Sweeps on Fully Coated Beams.

Once each of the beams has been broken in, a suitable sweep rate of 2 Hz/min has been identified, and the bare beam has been modeled, it is possible to perform the sine sweep data collection. Each of the six beams (3 mag spinel, 3 YSZ) went through 18 sine sweeps utilizing a down sweep. The input ranged from a value of 0.01 Volt to 8 Volts beginning with lowest input. There was a period of 10 seconds in between tests and a test took just over 90 minutes. During this time it was necessary to keep the electromagnet cool via the embedded cooling tubes. The thermocouple implanted in the electromagnet never indicated that the temperature of the coil exceeded 50°C. To minimize the time it takes to perform the test, a 10 Hertz sweep range data collection window was chosen. It was necessary to manually observe the sweeps and ensure that the entire resonant peak was being recorded. With this in mind, it was necessary to re-window the sweeps if it appeared that the graph would not capture all of the data. Re-windowing is when the data being recorded via VibrationVIEW was physically observed and the 10 Hz range adjusted manually to allow the entire resonant peak to be recorded. That is why Figure 42 and Figure 43 have portions of lines missing on the sweeps. For instance, in Figure 42, the low input graphs have no data past 225 Hz. This is because the data collection window had to be resized so as not to cut off the resonant peaks of the high input voltage data.

Both the graphs highlight the nonlinearity of the beams associated with increasing input magnitude. The strain softening of the material can be observed by the way the curves tend to “lean” to the right. A linear material would have the resonant peaks all at

the same frequency. To a lesser extent, linearity in the beams at low input voltage magnitude can be seen in the form of nearly symmetrical curves.

The steps necessary to generate one curve are:

1. Set sweep range, beginning at high frequency progressing to low frequency, of 10 Hz determined by resonance value at last sweep. If necessary shift range to allow entire peak and values equal to or greater than $.707V_{MAX}$ to be plotted. Refer to previous section for specific process.
2. Set sweep rate of 2 Hz/min as determined in previous section.
3. Set desired input voltage.
4. Run Sine Sweep Test
5. Repeat for all curves. Monitor results to allow for frequency shift.

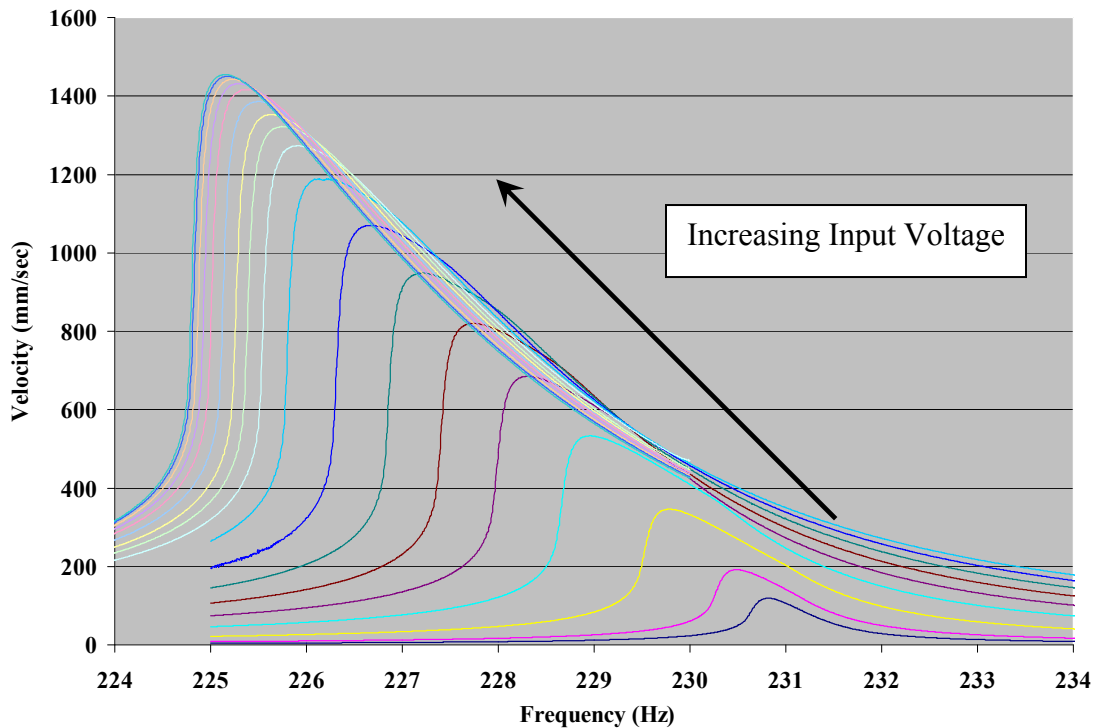


Figure 42: Sine Sweep of Titanium Bar Coated with Mag Spinel and Bond Coat

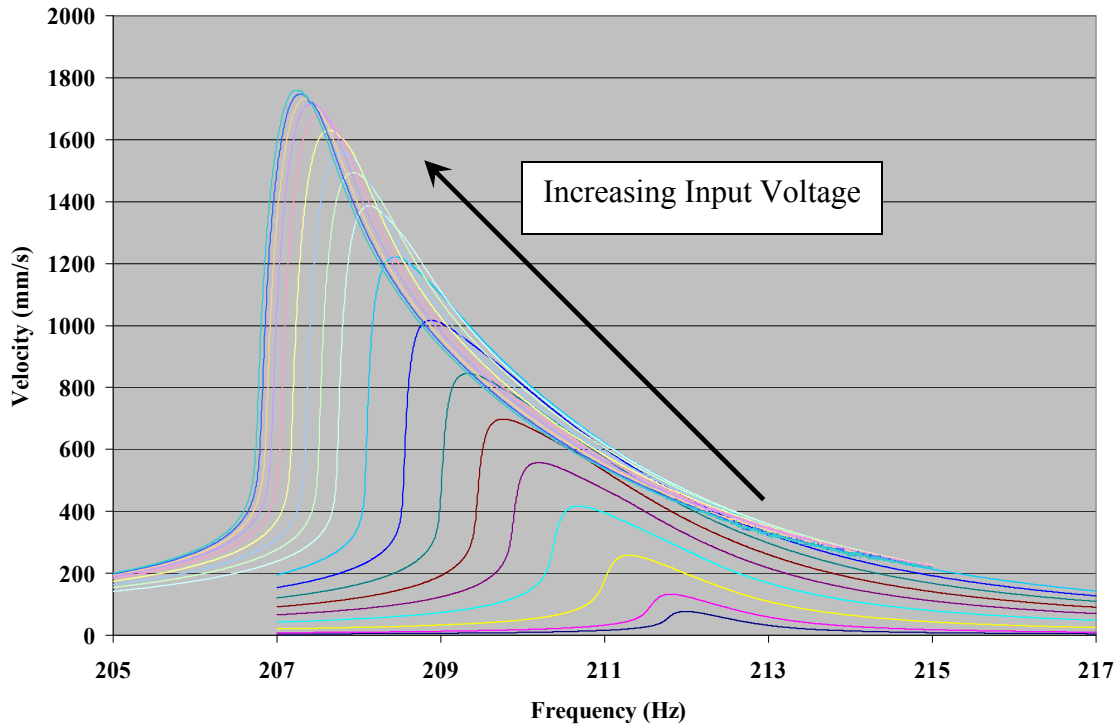


Figure 43: Sine Sweeps of Titanium Bar Covered with YSZ and Bond Coat

This lean also indicates that as the maximum velocity increases the resonant frequency decreases. The frequency decreases until an input voltage is reached that doesn't produce an increase in the velocity at the center of the beam or a change in frequency. The change in frequency and the change in velocity in this study was very small at the highest input voltages. This can be seen by the peaks of the curves that pile up one on top of another at the lowest frequencies. It should be noted that the data generated by these graphs have not been altered by smoothing or processing of any type and are directly out of the VibrationVIEW program. Each curve generates one resonant frequency, one peak velocity and a loss factor. This data is what is used in the finite element portion of the experiment to extract the material properties of the homogenized coating. Table 4 gives insight into the variety of responses beams of the same dimension and with the same

coatings can have. This table shows how each beam displays different response characteristics to the same inputs. The maximum velocity at the center of the beam is different for each specimen. The maximum response value is the maximum response of all 18 input voltages. The minimum response is the minimum for all 18 as well. Also the range of frequencies which is needed to capture each resonant frequency, is different for each beam.

Table 4: Responses of Six Beams

	Maximum Response (m/sec)	Minimum Response (m/sec)	Frequency Range (Hz)
Mag Spinel			
Bar 4	1.0287838	0.084123787	225.148-230.813
Bar 9	1.33053	0.088296	222.203-227.972
Bar 15	1.35243	0.0899808	220.871-226.459
YSZ			
Bar 10	1.61975	0.0672542	206.802-212.674
Bar 11	1.3812	0.0600998	203.933-209.737
Bar 12	1.75934	0.0771703	207.271-211.987

Material Properties through Finite Element Analysis

This section will describe step by step the process that goes into generating the coating's material properties of Young's Modulus, Loss Factor, and Loss Modulus. The finite element program ANSYS will help to generate curves which will characterize the nonlinear nature of the coatings.

Generating Curves to Determine Material Properties.

The finite element program ANSYS was used to perform finite element analysis on the mag spinel-NiCrAlY coating and the YSZ-NiCrAlY coating. Previously ANSYS

had been used to characterize the bare beam. The bare beam and magnet material properties are listed in Table 5. The properties of the beam were determined experimentally. The density, ρ , was calculated using 10 titanium bar volumes and masses. The volumes, V , were calculated using an average of heights, thicknesses and widths measured with a caliper. The masses, m , were calculated using a scale accurate to thousandths of a gram. The relation $V\rho=m$ was used to determine the density. The magnet material properties used were taken directly from a previous report (Reed, 2007). The mass, volume and density of the glue that was used to hold the magnets on the beam was neglected.

Table 5: Bare Beam and Magnet Material Properties

	Titanium Beam	Magnets
Young's Modulus (GPa)	110.4884854	206.8427184
Density (g/cc)	4.373424944	3.902866564
Poisson' Ratio	0.33	0.33

Likewise the adhesive used to hold the upper tube to the top node was neglected. The stiffness and mass added to the system by the magnets and adhesive was factored into the model when the modulus was adjusted to match the bare beam experimental data. The coated beam was comprised of 10640 elements. The element size of the beam was 1.27 mm X 1.27 mm X 0.8 mm. The element size of the coating was 1.27 mm X 1.27 mm X 0.254 mm. The coating thickness was less than ideal in terms of aspect ratio but, that element size was utilized so the bare beam nodes would all align with the coating nodes. These nodes were connected via a glue command in ANSYS that produced a rigid bond at the nodes. This was a free-free model so there were six degrees of freedom associated

with the model. A modal analysis was performed so there was no input forces applied to the beam. Instead of conducting a convergence study it was deemed acceptable to perform an analysis with similar element numbers as the previous FE model (Reed, 2007).

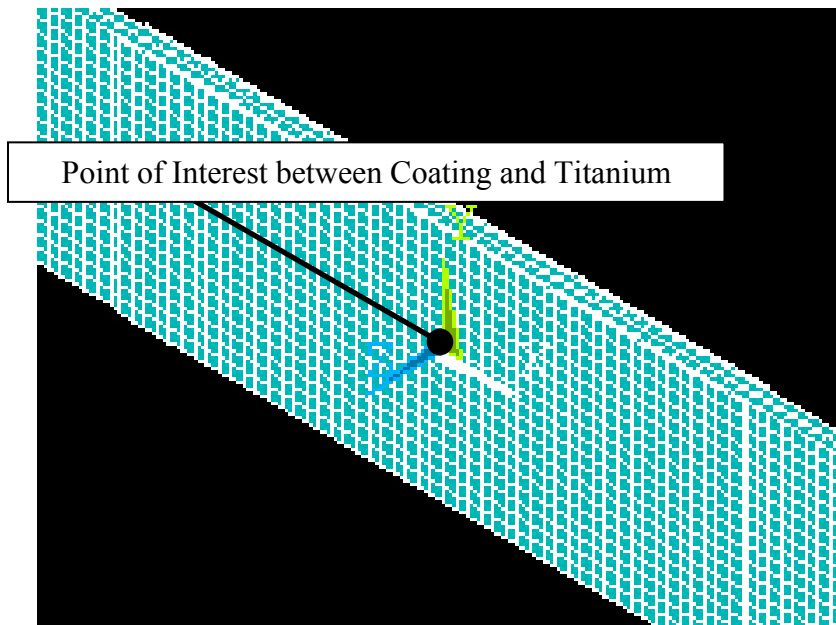
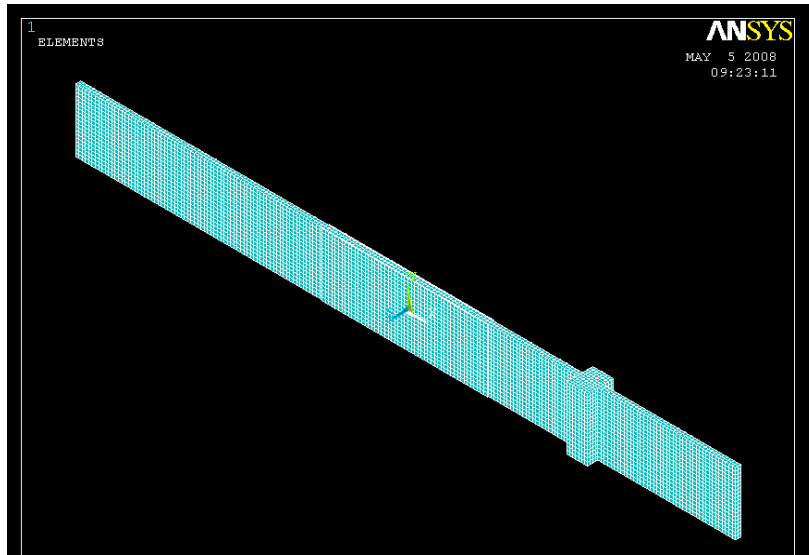


Figure 44: ANSYS Generated Beam with Coating

After the bare beam was modeled with magnets attached, the coating was added to the center of the beam. The density of the coatings was calculated by measuring the volume and mass of the beam before and after the coating process. A density was calculated that took into account both the bond coat and top coat materials. If it is desired to model all three layers (beam, bond coat and top coat) it would be necessary to add an additional step and pause after the bond coat is applied to measure the volume and mass of the beam with bond coat only. A Poisson's ratio of 0.33 was assumed for all of the materials in the model. This was another assumption used in previous studies (Reed, 2007). This conventional assumption could add even more error to the final results. As was stated in a previous section, in order to accurately depict the nonlinear characteristic of the ceramic hard coating curves it is necessary to generate several models over the range of frequencies measured in the laboratory. Table 6 lists all of the material properties that were used to create the models for the finite element analysis. It should be noted, the following Tables and Figures were generated using both finite element data and physical data using the methods described in the two previous Chapters.

Table 6: Material Properties for Ceramic Hard Coatings Used in FEA

Model	Mag Spinel		YSZ	
	Density (g/cc)	E _c (Gpa)	Density (g/cc)	E _c (Gpa)
1	2.7258	34.4738	4.1762	6.8948
2	2.7258	41.3685	4.1762	13.7895
3	2.7258	48.2633	4.1762	20.6843
4	2.7258	55.1581	4.1762	27.5790
5	2.7258	62.0528	4.1762	34.4738
6	2.7258	68.9476	--	--

Once finite analyses were run for all eleven setups, several useful characteristics were extracted from the ANSYS output file (Table 7).

Table 7: Finite Element Results

Model	Mag Spinel			YSZ		
	E_c (GPa)	(Hz)	SER	E_c (GPa)	ω (Hz)	SER
1	34.4738	217.99	0.14796	6.8948	199.63	0.04630
2	41.3685	221.11	0.16329	13.7895	204.05	0.08300
3	48.2633	224.02	0.17584	20.6843	208.11	0.11233
4	55.1581	226.74	0.18613	27.5790	211.86	0.13591
5	62.0528	229.30	0.19454	34.4738	215.32	0.15494
6	68.9476	231.70	0.20138	--	--	--

The other values generated by the ANSYS FEA program have to do with the reference strain in the center of the beam between the coating and the bare beam. This reference location gives a normalized reference strain as well as a displacement that represents the mode shape (eigenvector) for the first bending mode of the beam. As a reminder, Figure 44 shows the location of the reference point.

Table 8: Finite Element Results at Reference Location

Model	Mag Spinel			YSZ		
	E_c (GPa)	$X(L/2)$	$\tilde{\epsilon}(L/2)$	E_c (GPa)	$X(L/2)$	$\tilde{\epsilon}(L/2)$
1	34.4738	-0.53468	0.007329	6.8948	-0.53803	0.008319
2	41.3685	-0.52949	0.007097	13.7895	-0.53122	0.008002
3	48.2633	-0.52462	0.006880	20.6843	-0.52489	0.007709
4	55.1581	-0.52002	0.006675	27.5790	-0.51899	0.007436
5	62.0528	-0.51568	0.006482	34.4738	-0.51348	0.007182
6	68.9476	-0.51170	0.006300	--	--	--

With the five points generated for the YSZ coating and the six points generated for the Mag Spinel coating, it is possible to generate a curve fit to these points to help

characterize the nonlinear character of the coatings. In this analysis, a second order polynomial was fit to the data using the Microsoft Excel trendline feature. The coating moduli, E_c , generated through the finite element analysis were related to: frequency, ω ; mode shape, X ; normalized strain, $\tilde{\varepsilon}$; and strain energy ratio (SER). Each of the following four graphs and equations generated using the FEA data are for the mag spinel coating. The same figures and calculations for YSZ can be found in Appendix B.

The first curve fit, via the add trendline function in Microsoft Excel, characterizes the relationship between coating modulus and frequency. A second order polynomial was generated to represent this relationship.

$$\text{Mag Spinel: } E_c = 0.0297\omega^2 - 10.827\omega + 985.2 \quad (13)$$

The relationship between the modulus and the frequency depends on using units of GPa for modulus and Hertz for frequency.

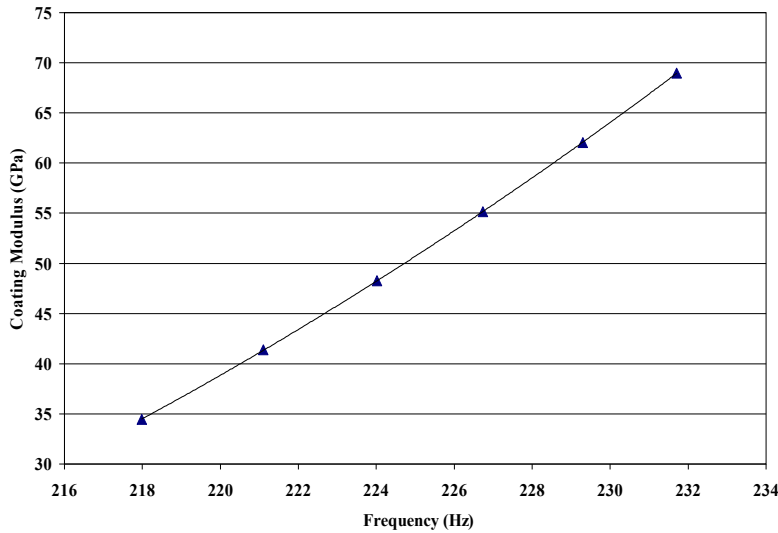


Figure 45: Storage Modulus Relationship to Frequency

The next relationship in Figure 46 relates coating modulus to mode shape displacement at the center point. Visually the graph makes sense in the fact that as the material stiffens the beam deflects less. Again this equation was generated via Microsoft Excel and the trendline function.

$$\text{Mag Spinel: } X(L/2) = -3E-06E_c^2 + 0.001E_c - 0.565 \quad (14)$$

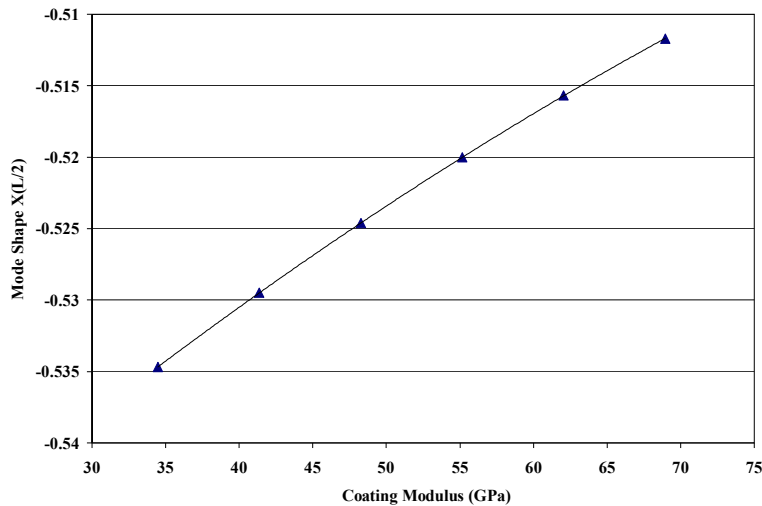


Figure 46: Mode Shape Relationship to Coating Storage Modulus

The next equation generated is the relation between coating modulus and normalized reference strain. As previously stated, the reference strain is located at the coating/beam interface. The strain at this point is a normalized value which will be related to actual strain in a subsequent section. The equation generated by the points in Figure 47 is:

$$\text{Mag Spinel: } \tilde{\varepsilon}(L/2) = 1E-07E_c^2 - 4E-05E_c + 0.0087 \quad (15)$$

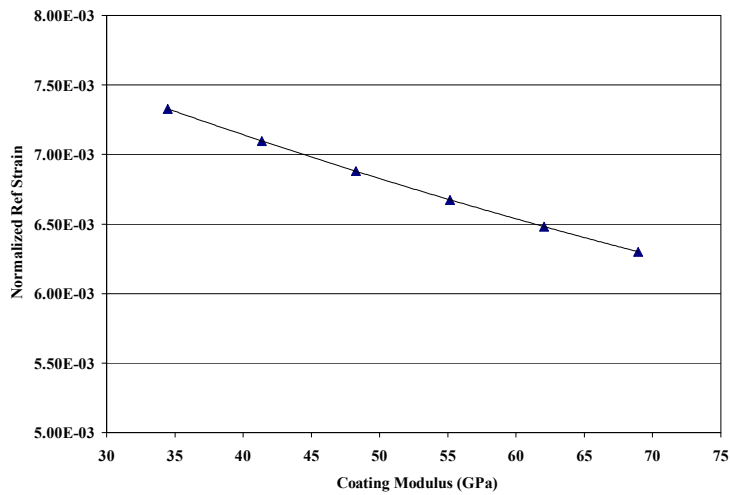


Figure 47: Normalized Reference Strain Relation to Coating Storage Modulus

The final relationship generated by the finite element analysis is the relation between strain energy ratio (SER) and coating modulus. This ratio is the value that relates strain energy in the coating alone to the strain energy in the coating and beam system. The following equation relates SER to coating modulus.

$$\text{Mag Spinel: } \text{SER} = -2\text{E-}05\text{E}_c^2 + 0.0038\text{E}_c + 0.0425 \quad (16)$$

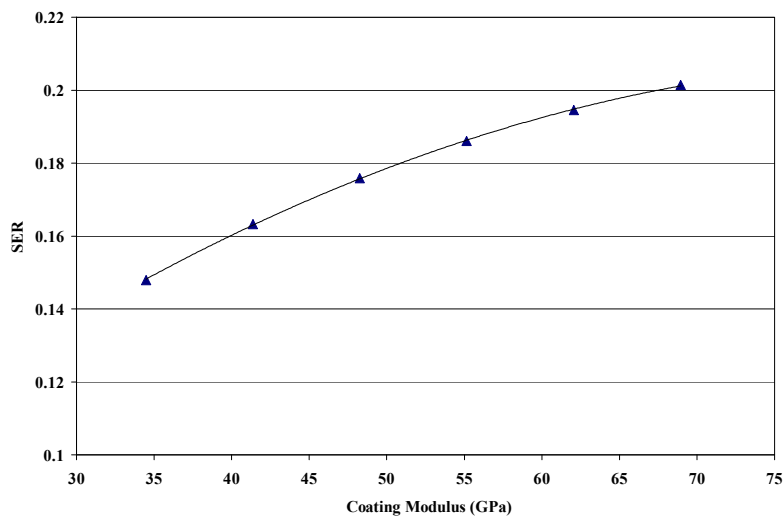


Figure 48: Strain Energy Ratio Relation to Coating Storage Modulus

Apply Experimental Data to Finite Element Model.

The next step in generating material properties is inserting experimental data into the four Equations (13-16) produced through the previously explained curve fitting. This step applies the data generated by the input sweeps in the lab to the second order polynomial equations for the three beams coated with either the mag spinel combination or the YSZ combination. Figure 49 shows the experimental data points that will be used in conjunction with the FE generated quadratic equations. The frequency values will be inserted into Equation 13 to produce coating modulus values. The velocity values for the points in the Figure will all be related to the values generated using Equations 13-16 .

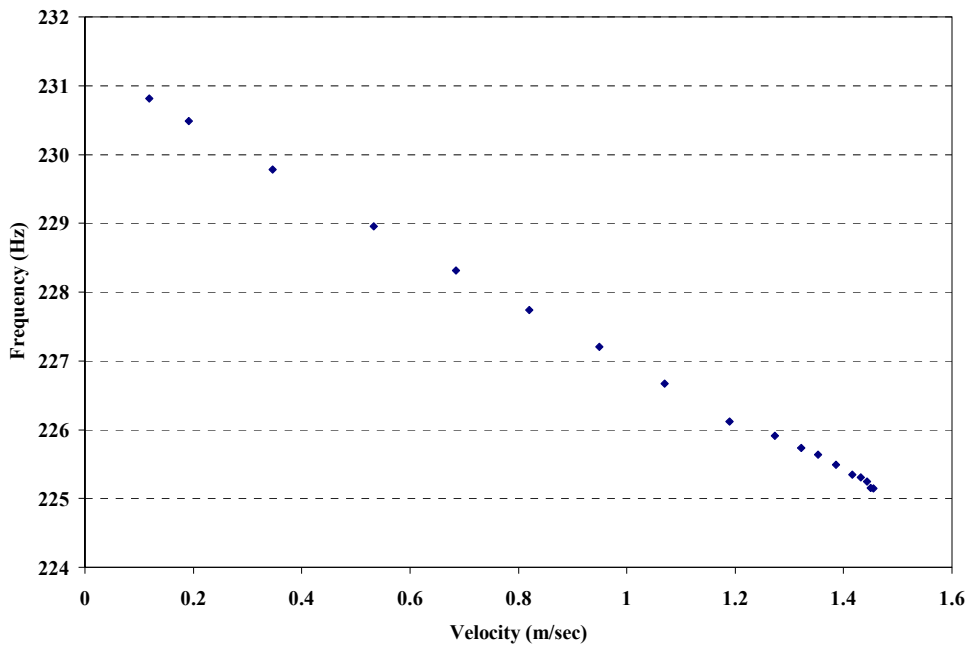


Figure 49: Experimental Data Resonant Frequency Associated with Maximum Velocity

The following graphs were generated using the experimental and finite element data collected for a mag spinel-bond coated beam. The first graph (Figure 50) shows the relationship between measured velocity and coating modulus. The frequency values for each point in Figure 49 were inserted into Equation 13. This generated 18 coating modulus values which could be related to velocity because of the relationship between frequency and velocity in Figure 49. It appears, from Figure 50, that the material has yet to achieve a minimum stiffness. Had this happened the graph would have approached, asymptotically, a particular coating modulus value. In future research it is recommended that the beam be tested at higher strain amplitudes. As the YSZ coating was stiff, it approached a constant coating modulus value. The YSZ coating was less stiff than mag spinel and appeared to achieve a minimum coating modulus value at high strains.

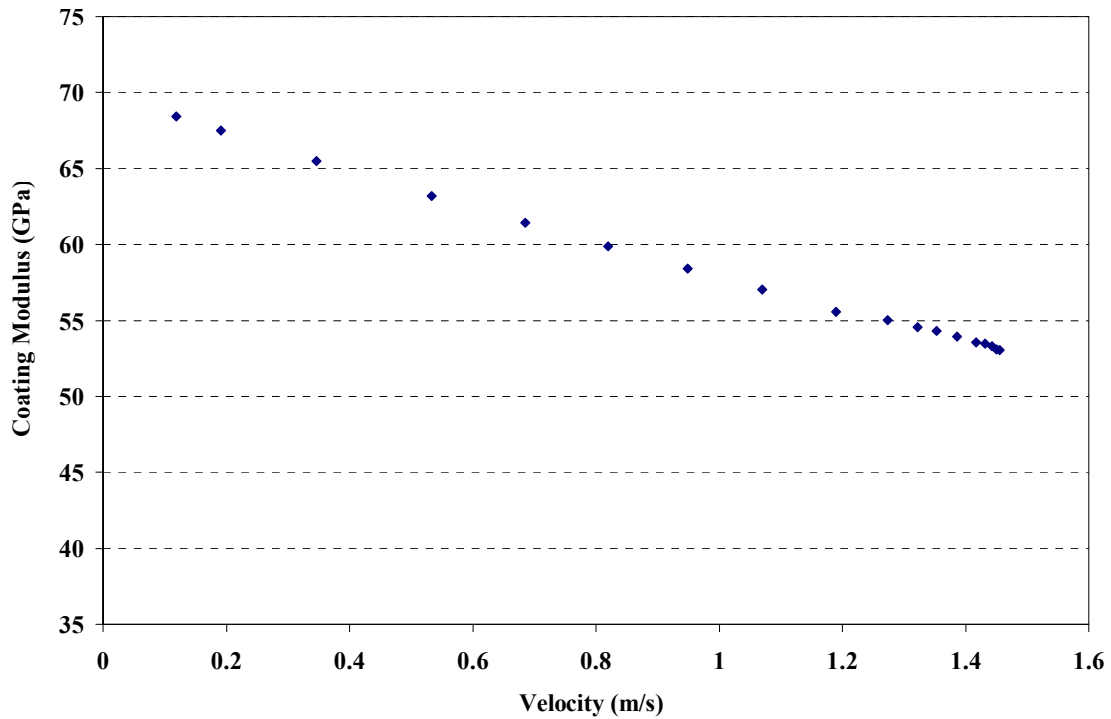


Figure 50: Mag Spinel Coating Modulus vs. Beam Measured Velocity at L/2

The next relationship generated is between the recorded velocity at the center of the beam and the strain energy ratio. These values were calculated by inserting the coating modulus values from Figure 50 into Equation 16 and plotting the SER values with respect to the measured velocities. Figure 51 shows that as the response increases (velocity increases) the strain energy ratio decreases. This indicates that as the velocity at the center of the beam increases, the SER decreases which means that the strain energy in the beam becomes more dominant with respect to the strain energy in the coating. Thus, the coating becomes less effective at damping at high velocities. The variation in the bare beam loss factor is not affected at strain values in a low range such as what is being examined in this study. Therefore the constant loss factor assumption is appropriate. In dealing with higher strains, it may be appropriate to not use a constant bare beam loss factor.

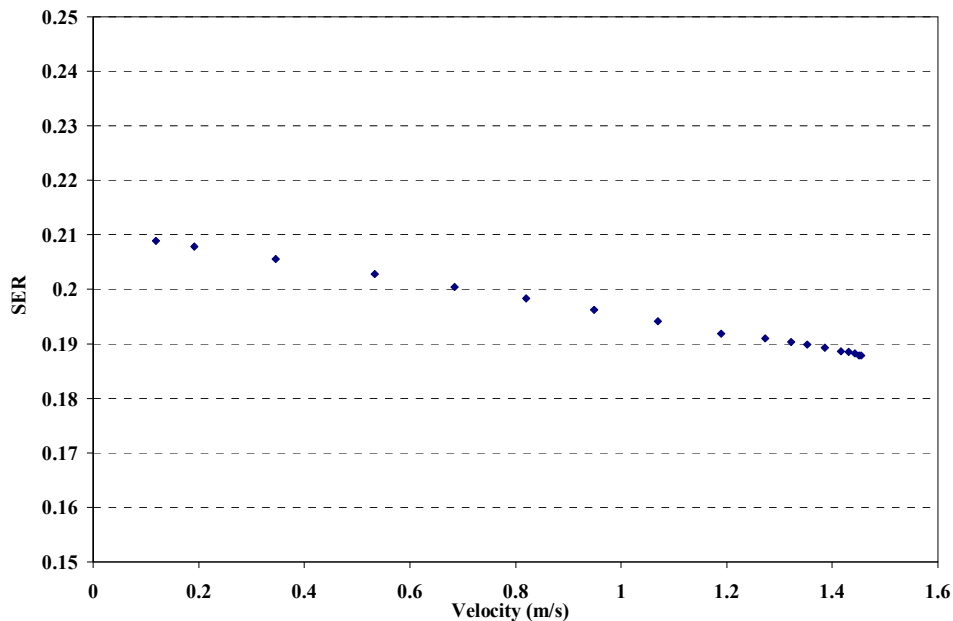


Figure 51: Strain Energy Ratio vs. Measured Velocity at L/2

The next relationship to be determined is between the loss factor, η_c , of the coating alone versus response velocity at the center of the beam. This value is determined using the equation:

$$\eta_{coat} = \frac{\eta_{sys}(SER + 1) - \eta_{bare}}{SER} \quad (9)$$

It should be noted that this equation uses values calculated through pure experimental methods (η_{sys} and η_{bare}) and FE modeling methods (SER). The values of SER inserted into Equation 17 were a product of the values displayed in Figure 51. The system loss factor, η_{sys} , values were generated by utilizing the half-power bandwidth method. The values generated to use this method were from the input voltage sweeps discussed in a previous section. The bare beam loss factor, η_{bare} , was assumed to be a constant value.

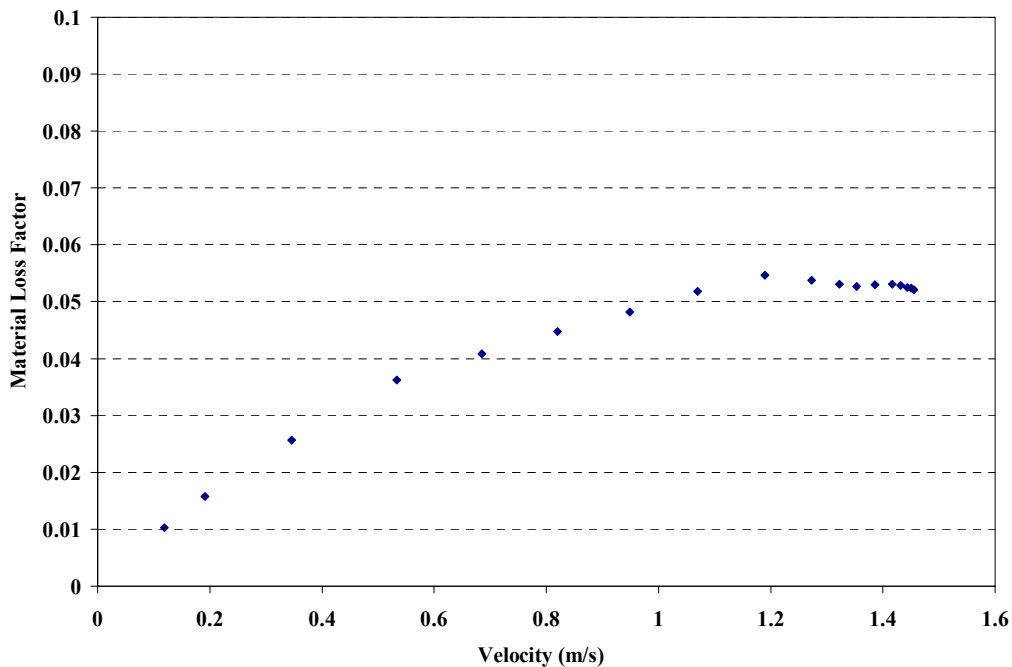


Figure 52: Coating Loss Factor in Response to Response Amplitude at L/2

The relationship presented in Figure 53 shows how deflection at the center of the beam increases as the beam responds to increasing input voltage. This set of points was generated by inserting the values of coating modulus in Figure 50 into Equation 14. This relationship will eventually help lead to a scaling factor which will be used to generate a relationship between normalized strain and actual strain.

Figure 54 shows the scaling factor that will be used to relate the normalized reference strain to the actual strain. This data was generated by first using the relationship of Equation 18 for the points in Figure 49 then dividing the resulting values by the data in Figure 53. Again it is important to multiply frequency, ω , by 2π to ensure the computed value has the correct units.

$$\delta = \frac{V}{\omega} \tag{5}$$

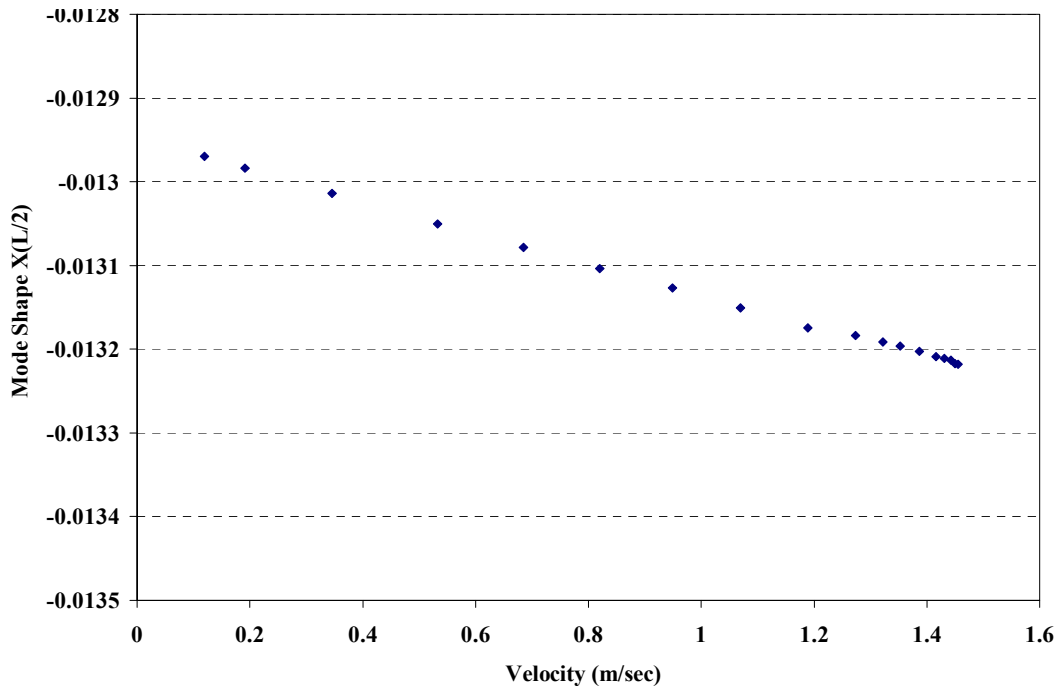


Figure 53: Mode Shape Response to Beam Response at L/2

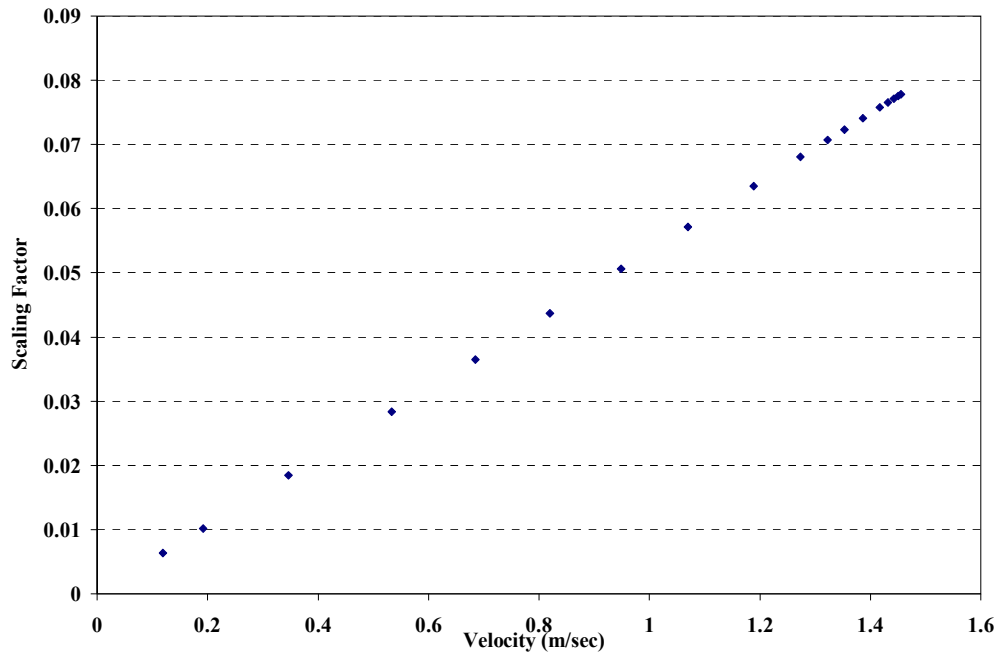


Figure 54: Scaling Factor

Figure 55 was generated by inserting the coating modulus values of Figure 50 into Equation 15. The resulting values are the normalized strains at the center of the beam between the coating and titanium. Finally, Figure 56 was generated by using the relationship $\varepsilon = \lambda \tilde{\varepsilon}$. The scaling factor values in Figure 54 are multiplied by the normalized reference strain values in Figure 55. The result is a set of actual strain values that are related to the experimental velocity values in Figure 49. Figure 55 and Figure 56 show how the strain response of the beam increases as the beam responds to input with high velocities. Now that each of the relationships has been generated the material properties of the coatings can be examined.

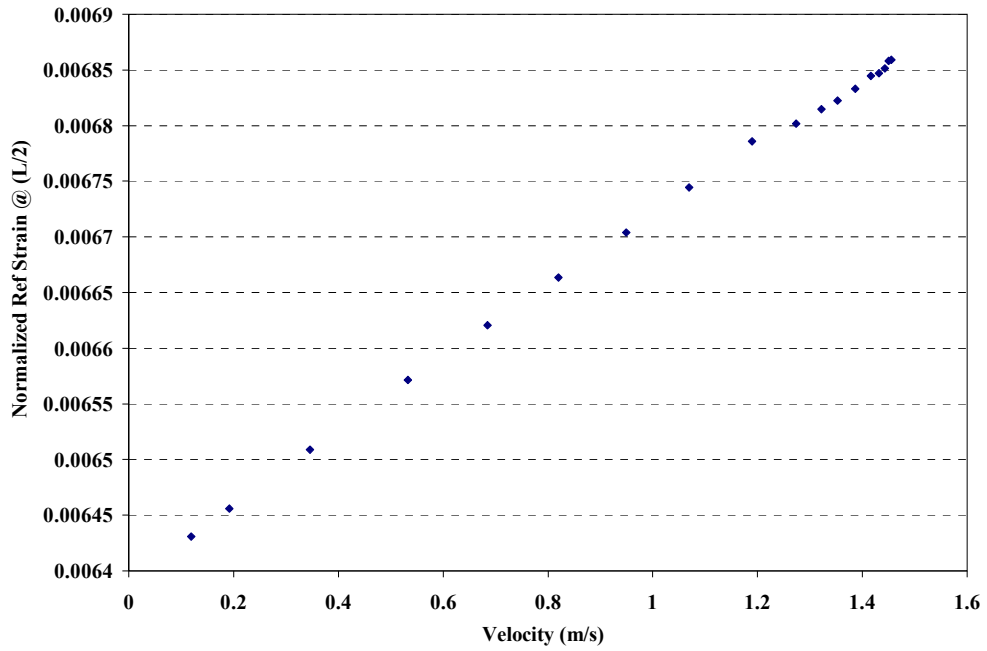


Figure 55: Normalized Reference Strain Response to L/2 Measured Velocity

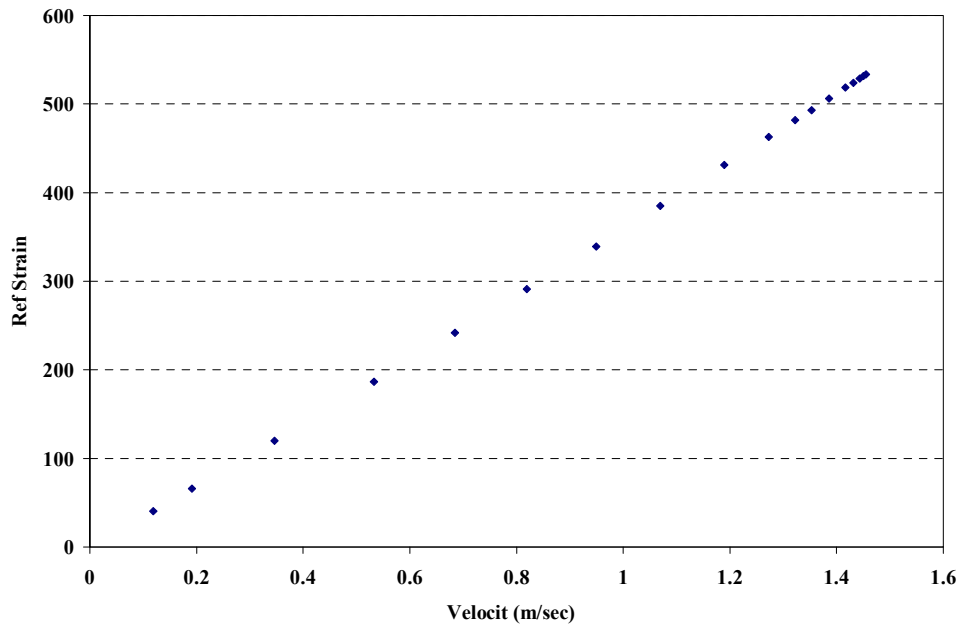


Figure 56: Reference Strain Response to L/2 Measured Velocity

Material Properties.

Now that relationships have been developed for strain, coating modulus, and loss factor, each of the coating's material properties can be analyzed. The first coating to be analyzed is the Mag Spinel-bond coat combination. The first Figure shows the three beam's calculated responses along with a curve fit to the points from the three beams. One can see that the modulus curve fit begins at a value of $E_c=62.5$ GPa and decreases, almost linearly, to a value of $E_c=47.3$ GPa at a value of $535 \mu\epsilon$. A sign that softening occurred could be observed in the graphs generated by the sine sweeps that appear earlier in the report. Because the value of the strain was not particularly high, it should be noted that there is not enough information to conclude whether or not the value of modulus has reached its lowest value.

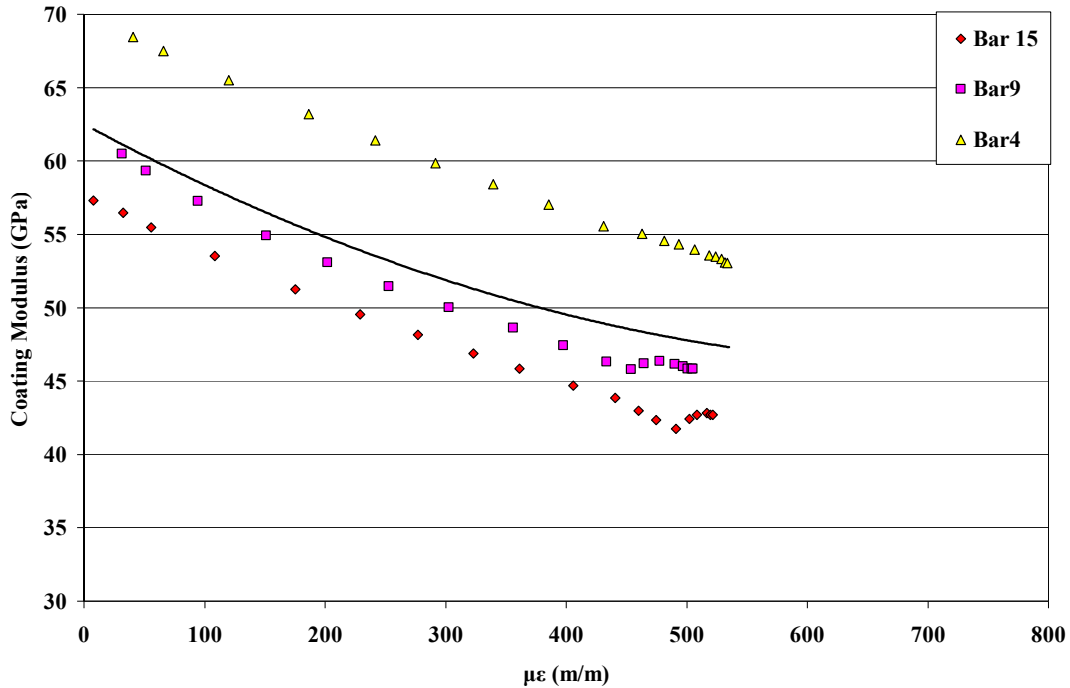


Figure 57: Coating Modulus Change Due to Strain for Mag Spinel

The next figure shows the beam response to strain in terms of the loss factor. One can see from the curve fit that the coating reaches a maximum damping value of $\eta = 0.058$ (or a damping ratio of 0.029 or a quality factor of $Q=17.24$) at a strain of $442\mu\epsilon$. That is a 747% increase in damping from the low strain condition to the maximum loss factor. After maximum damping is reached the coating damping effectiveness begins to decline.

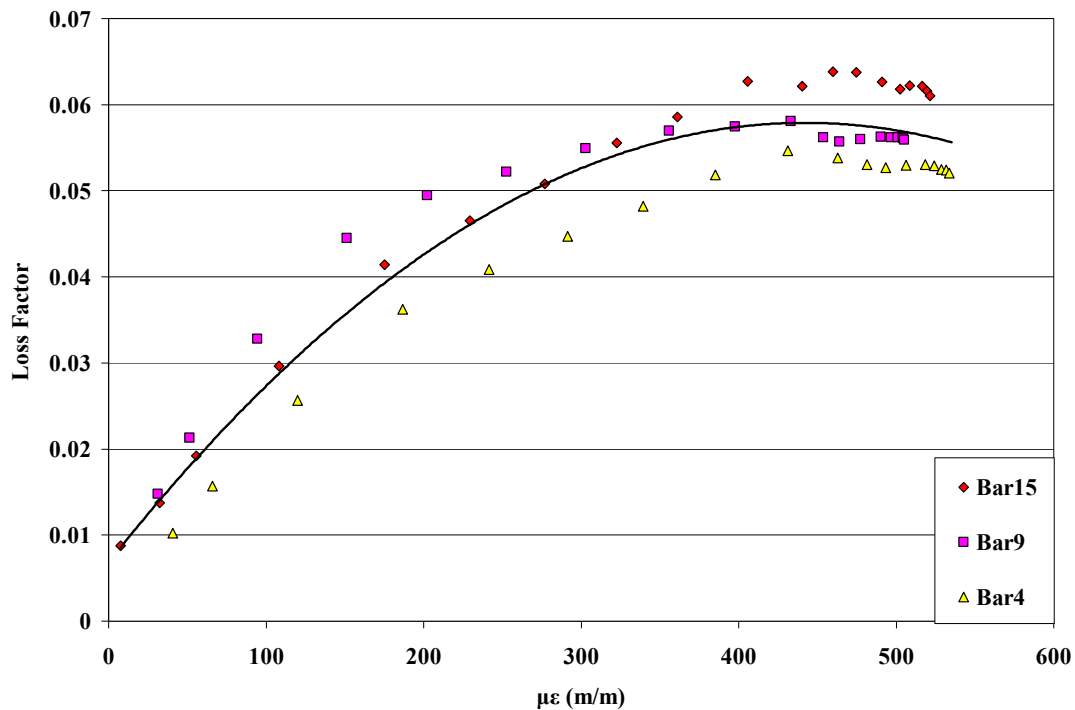


Figure 58: Loss Factor Change Due to Strain for Mag Spinel

The final mag spinel property that will be evaluated is the relationship between loss modulus and strain. Loss modulus is the product of loss factor and coating modulus. The

curve fit on the graph shows that the loss modulus reaches a maximum value of $E_2 = 2.85$ at a strain of $400 \mu\epsilon$. This is a 428% increase from the low strain condition.

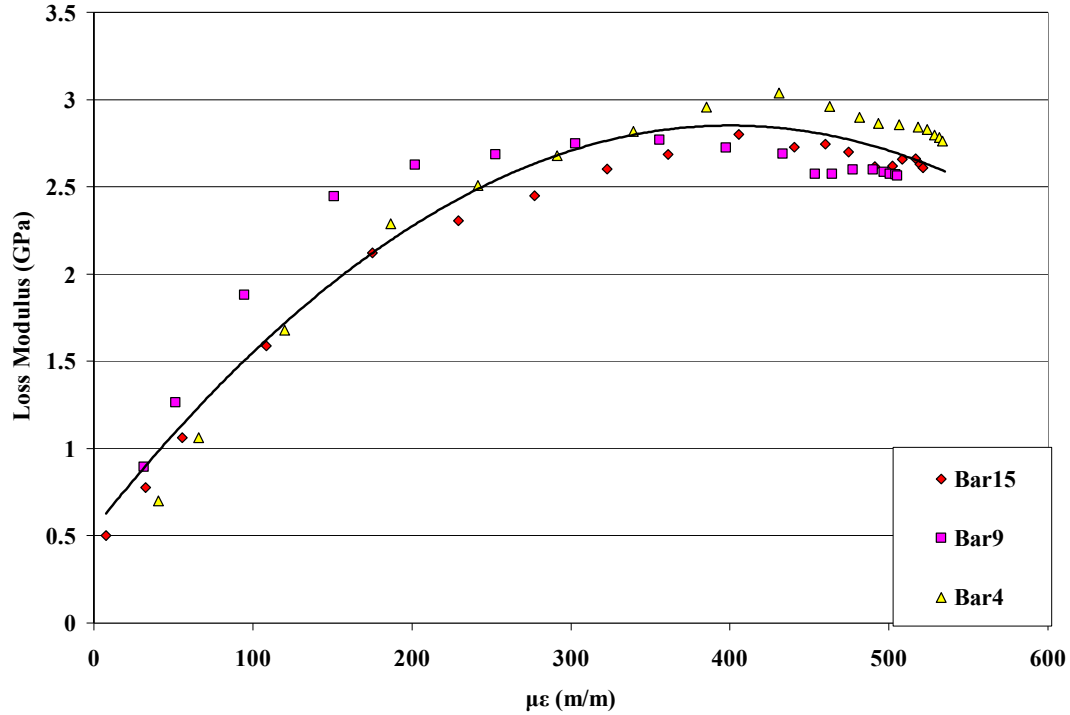


Figure 59: Loss Modulus Change Due to Strain of Mag Spinel

The other coating, yttria stabilized zirconia-bond (YSZ) coat, is evaluated in the same manner as the mag spinel. The YSZ coating modulus behaves in much the same manner as the mag spinel. The coating modulus value begins, at low strain, at 27.7 GPa and decreases in value as strain increases to a value of 15.4 GPa at a strain of $668 \mu\epsilon$ (Figure 60).

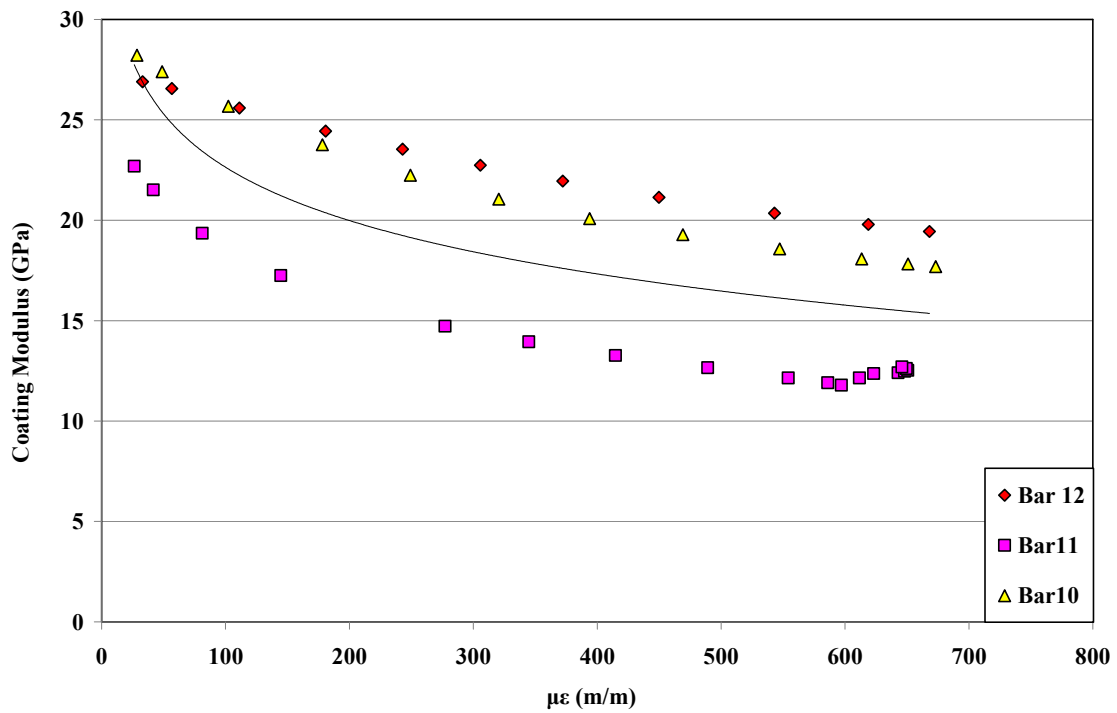


Figure 60: Coating Modulus Change Due to Strain for YSZ

The loss factor of YSZ follows the same trend as mag spinel. The loss factor is 0.025 at low strain and reaches a maximum value of 0.098 at a strain of 583 μ ϵ . This is a 295% increase in loss factor with strain increase. The damping ratio corresponding to 584 μ ϵ is .049 and the quality factor is Q=10.2. In Figure 61 it appears the curve fit generated does an accurate job of representing the shape of the curves.

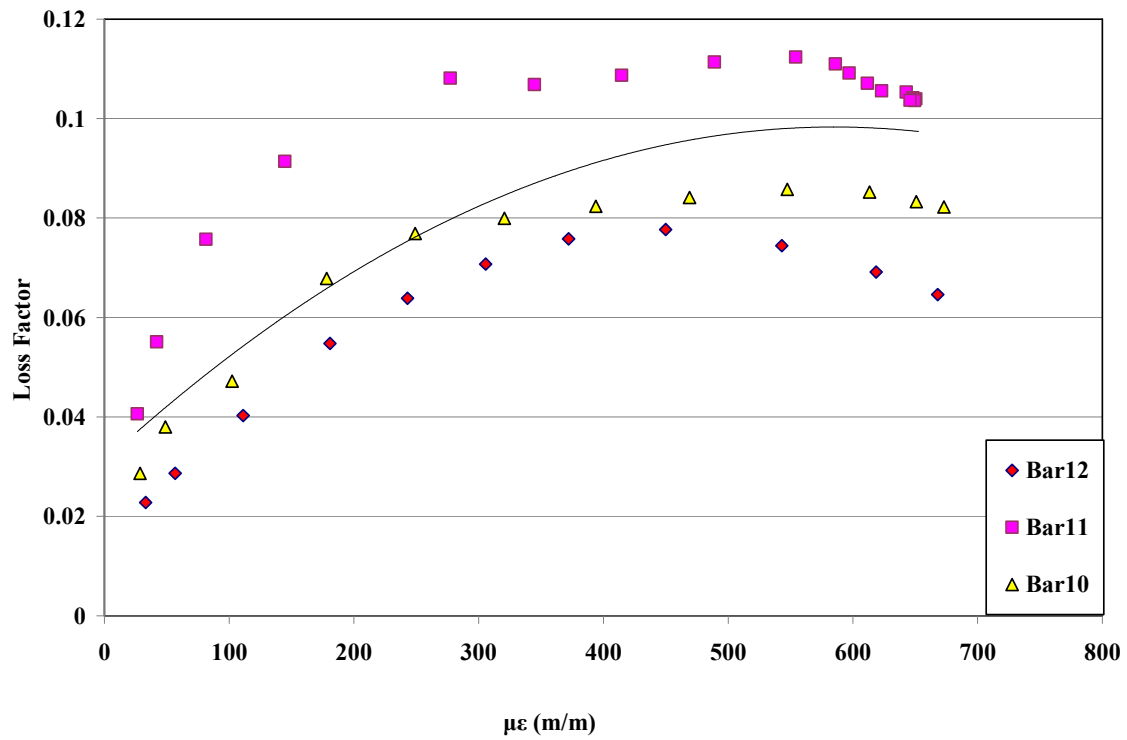


Figure 61: Loss Factor Change Due to Strain for YSZ

Finally, Figure 62 shows the change in loss modulus with strain. This value reaches a maximum of 1.64 at a strain of $392\mu\epsilon$. This is an increase in loss modulus of over 80% as strain increases.

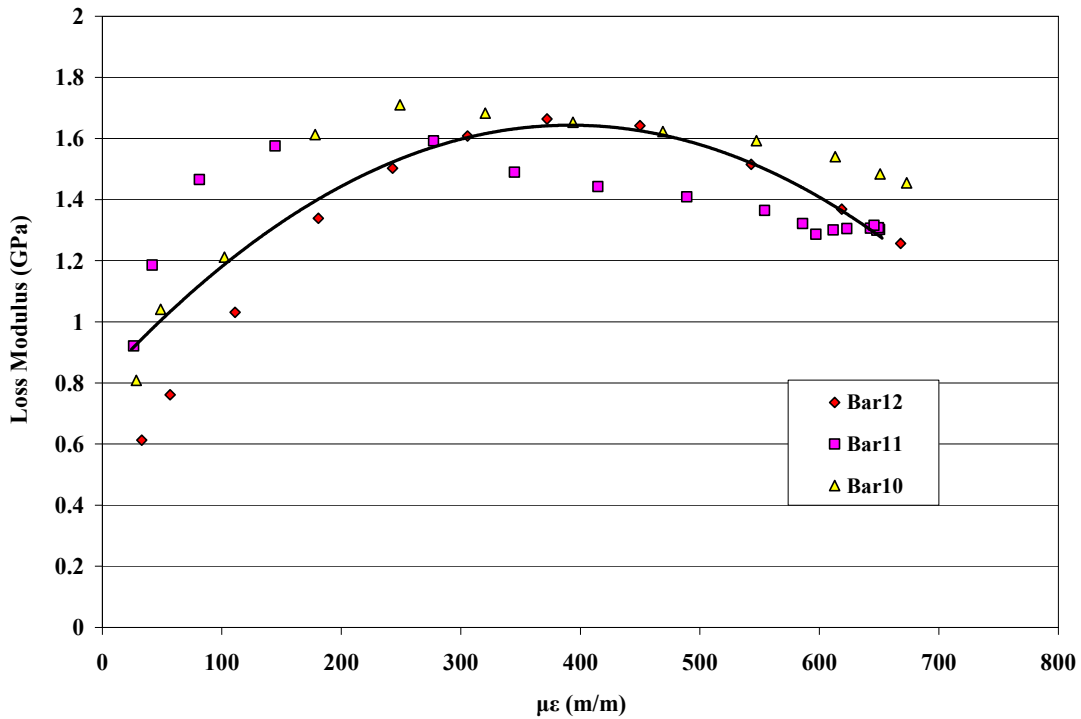


Figure 62: Loss Modulus Change Due to Strain for YSZ

The data that was recorded for YSZ exhibits a large variability across specimens. The reason for this variability is unknown but several assumptions can be made. First, the manufacturing of the specimens using the plasma spray process could lead to dissimilar coatings. This random nature of the bond coat shown in Chapter II shows how varying amounts of material could be contained in each beam specimen. Also the application of the magnets and the top tube to support the beam in the free-free test setup could lead to these results. The magnets and tubing were placed on the beam manually. A variation in the placement of these materials could lead to a slight difference in boundary condition from beam to beam. Therefore, the curve fits should only be used to get a general trend of the material YSZ.

Comparison of Results to Reed's Results

One of the objectives of this study was to determine whether or not decreasing the sweep rate would cause Reed's free and forced response data to coincide. Meaning, would the forced response curve migrate to the ends of the free response data? The thought was that if the slow sweep rate is equivalent to a quasi static solution for the forced response then the curve would correspond to the end or starting points of the free decay which is quasi static. In Figure 63 and Figure 64, one can see that the forced response curve does not quite align with the ends of the free response data. As the data was not readily available for a direct comparison, values of the "tips" of the free response curves and points of the forced response curve used in Figure 65, Figure 66 and Figure 67 had to be eyeballed off of the published data and are therefore estimates (Reed, 2007).

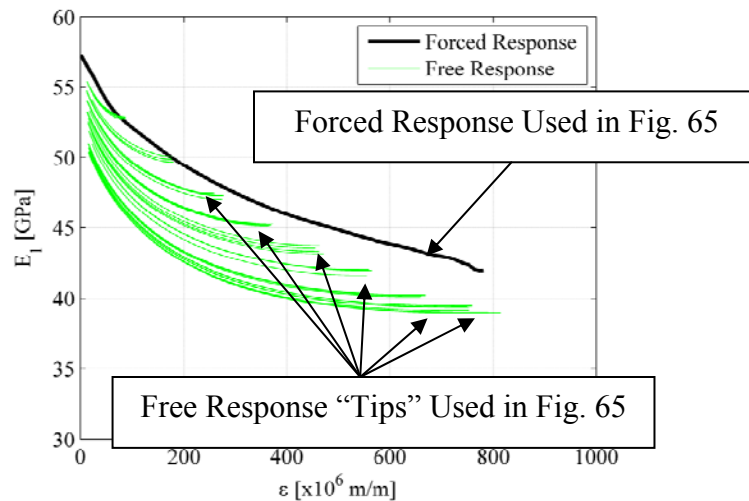


Figure 63: Reported Coating Modulus Calculated Via Forced and Free Response

(Reed, 2007)

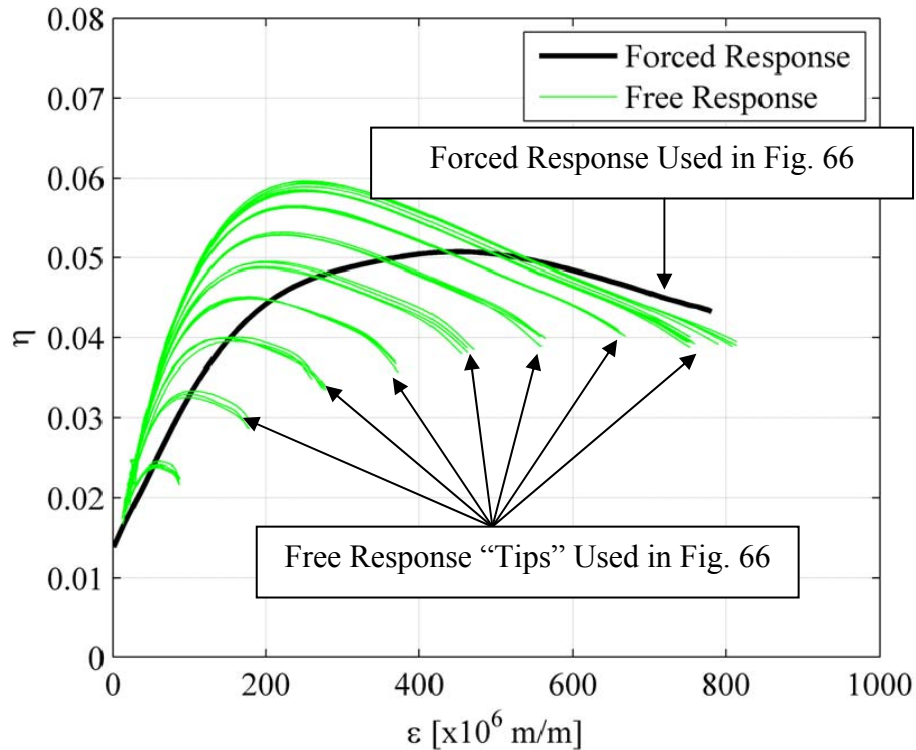


Figure 64: Reported Loss Factor Calculated Via Forced and Free Response
(Reed, 2007)

Figure 65, Figure 66, and Figure 67 shows the effect slowing down the sweep rate (2 Hz/min) has in attempting to correlate the tips of the free response curves to the forced response curve. As could be surmised from the analysis dealing with sweep rate in a previous section, it is apparent that adjusting the sweep rate will not cause the two sets of data to correlate. As was previously explained, altering the sweep rate has a minimal impact of maybe 10% change of value. This small of a change wouldn't cause the previously recorded data not to correlate. The free response and forced response lines were generated by visually picking values off of Figure 63 and Figure 64.

Evidently, the sweep rate is so time dependent that inertial effects are always present no matter how slow the rate and therefore the static free decay start is never approximated.

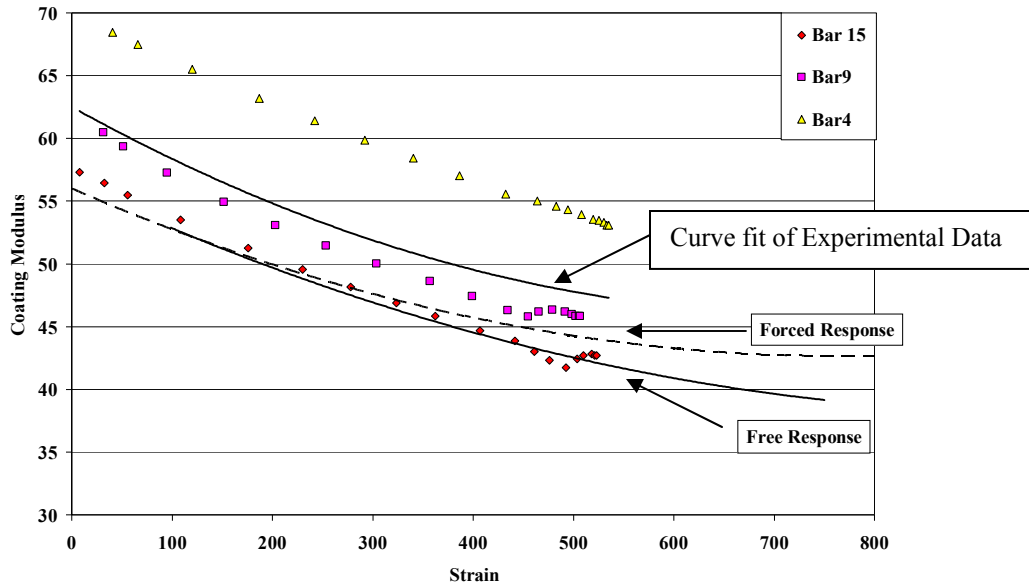


Figure 65: Comparison of Coating Modulus Values

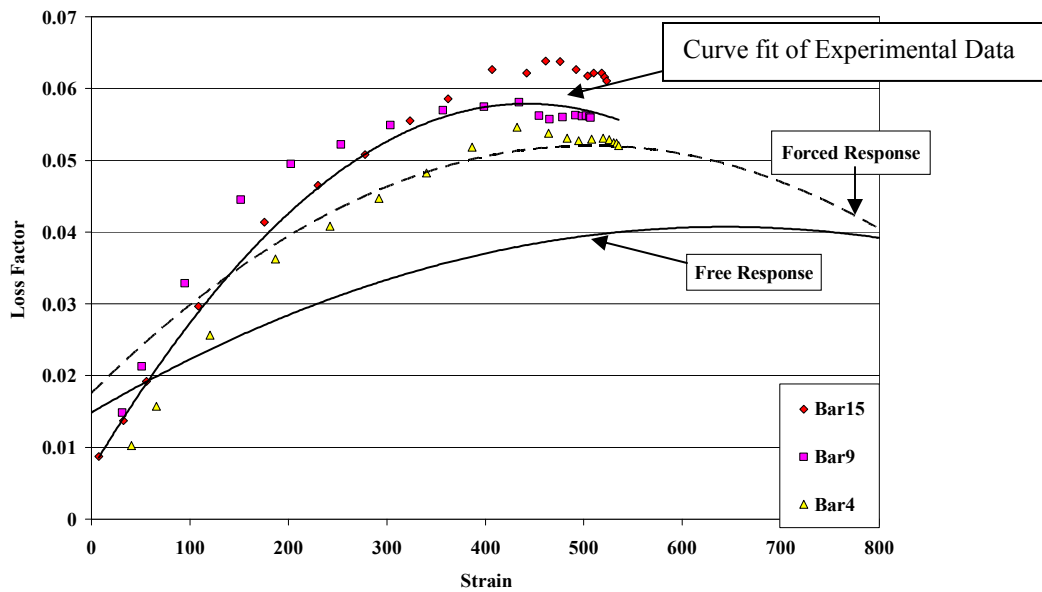


Figure 66: Comparison of Loss Factor Values

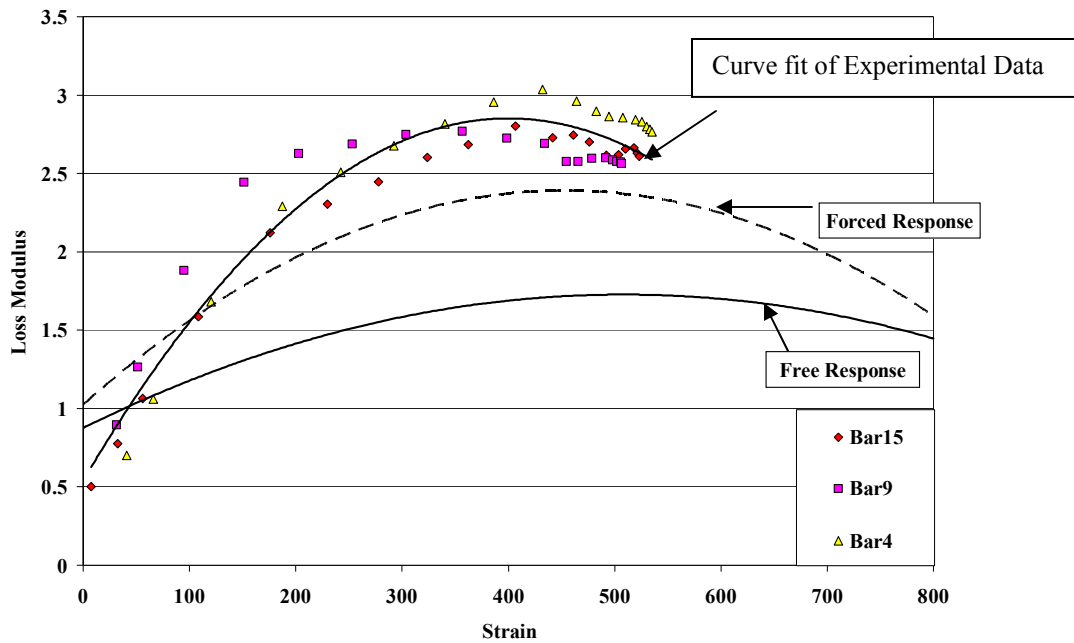


Figure 67: Comparison of Loss Modulus Values

Coating Material Comparison

This section deals with the similarities and differences between mag spinel and YSZ. In performing all the analysis up to this point it was noticed that both materials displayed similar trends which may be worth looking into. These plots should be able to differentiate how each material responds to loading.

First, Figure 68 displays the coating modulus for each coating with respect to strain. This figure shows that mag spinel is almost 2.5 times stiffer than YSZ. With this in mind it should be noted that both curves are very similar in shape. This indicates that the two hard ceramic coatings may use the same mechanism for damping.

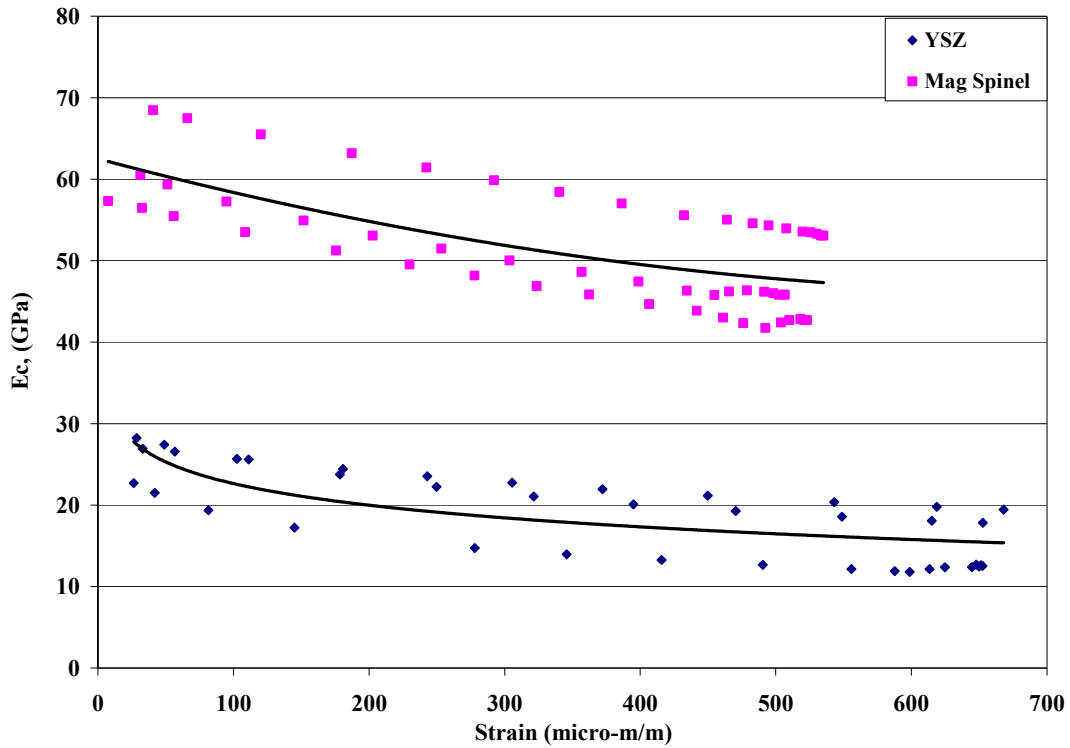


Figure 68: Material Comparison of Coating Modulus

In Figure 69, the loss factor for each material has been plotted with a curve fit to each set of data points. It is immediately apparent that YSZ does a better job of damping than mag spinel over all strain values. This is verified in the next section in the investigation of SEM images. The loss factor for the bare beam was reported earlier as .0008 over the same range of strains.

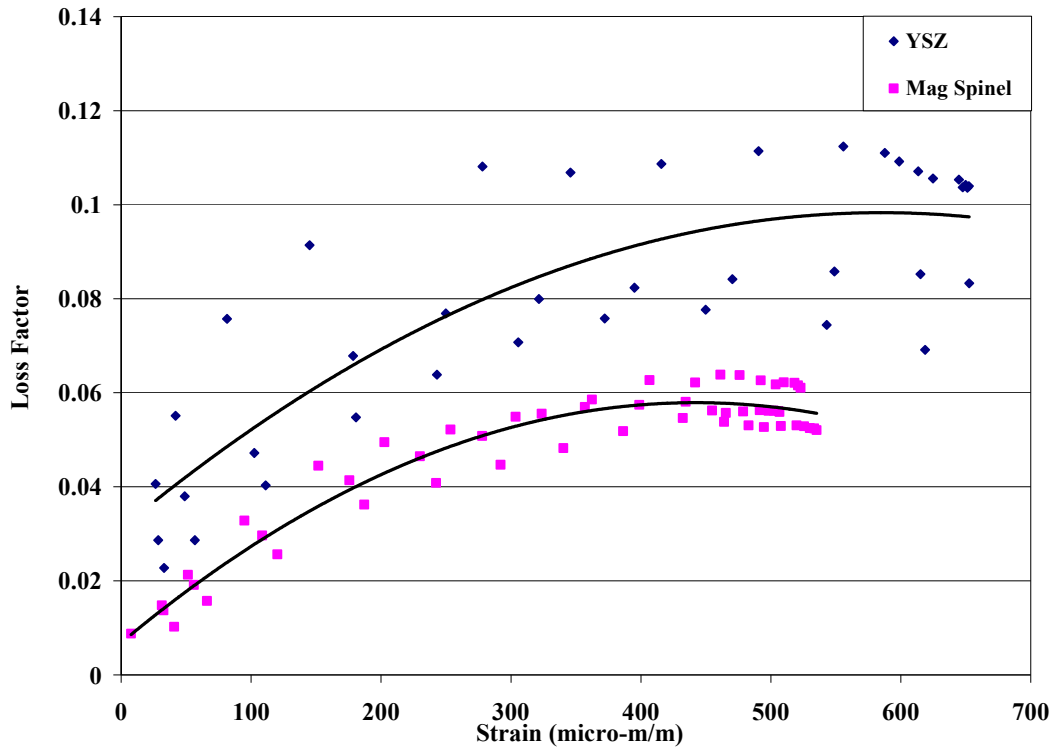


Figure 69: Material Comparison of Loss Factor

The similarities in the graphs indicate that the hard ceramic coatings applied via plasma spray behave in similar trends. As the loss modulus is a product of loss factor and coating modulus, it is no surprise that the trend lines have different shapes. Figure 70 shows the loss modulus of the two coatings and indicates that the coatings reach a maximum value at similar strain levels in the E_2 direction. This could be a cause of the method of application. It would be interesting to see if a material with an EB-PVD applied coating would behave in the same manner.

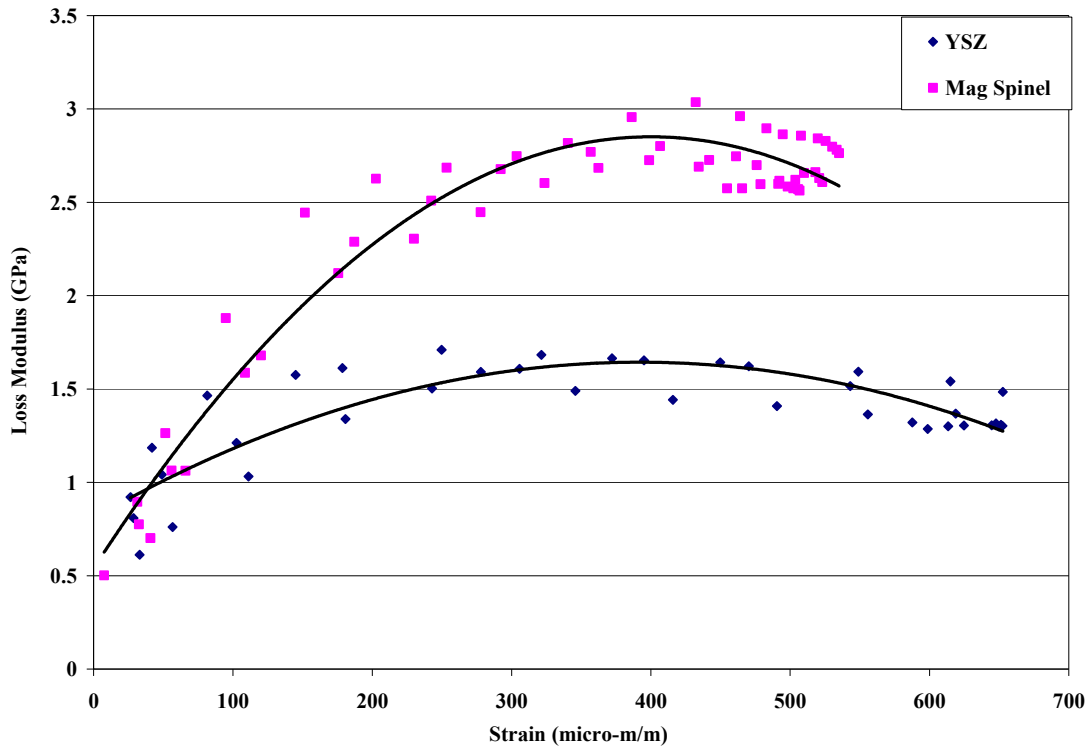


Figure 70: Material Comparison of Loss Modulus

Scanning Electron Microscope Analysis

This section of the report attempts to relate the experimentally determined findings from previous chapters to the physical microstructure behavior of the coatings. It was previously stated that the plasma sprayed coatings are made up of a series of splats which are the product of molten ceramic coating droplets that rapidly cool as they impact the substrate. The application process produces an intricate network of cracks and boundaries that help relieve stress and strain. Strangman states that as more and more boundaries are created and the microstructure develops, the modulus decreases to very small values (Strangman, 1985). The decrease in the value of the modulus with respect to strain increase could be a result of this phenomenon. By looking at before and after pictures of the coatings it is hoped that this hypothesis is confirmed.

It is assumed that the before pictures will show smooth boundaries between splats and a small number of cracks within the boundary which are perpendicular to the splat direction. The after pictures should show the boundaries between splats more opened up and an increased number of perpendicular cracks within the cracks. A significant increase in crack density should significantly relieve internal stresses and increase damping effectiveness.

A few issues may make this idea difficult to investigate. First, the materials may not have been subjected to adequate stresses and strains to produce crack growth. Second, the before pictures may not show the expected grain structure. Lastly, the before and after pictures could be extremely similar to one another.

Mag Spinel before Deformation.

The images that show mag spinel before being tested are presented in this section. Note that both a Back Scatter Electron (BSE) detector and a Secondary Electron (SE) detector were used in this analysis. The BSE detector made it possible to identify the different materials in the images. There are four materials that the reader should be aware of: the mounting material, the ceramic coating, the bond coat and the titanium. The other detector, the SE, was used to generate images that allowed physical inspection of the material surface. These images were the ones used to determine what kind of crack activity occurred during the experimental testing.

The first images in Figure 71 were captured at a magnification of 200x. These images clearly show the cross section of the titanium with bond coat and mag spinel. At this magnification, the SE image (top) does not give any clear indication of the microstructure. The only features identifiable with a splat structure in the ceramic coating are the pores which are a product of the plasma spray process. The BSE image (bottom) clearly shows the four different materials in the specimen. Starting at the top of the image, the material is mounting material, mag spinel, bond coat and titanium.

Figure 72 shows a picture of the coating at 247x magnification. This image was captured to show that the bond coat is extremely insignificant thickness-wise and the assumption that the material properties found for the homogenous coating could in fact be stated as the material properties of mag spinel alone. Again it is difficult to detect any type of microstructure besides the pores in the images. The BSE image (bottom) does

barely begin to reveal cracks in the microstructure. The spots in the SE image (top) are a polishing residue.

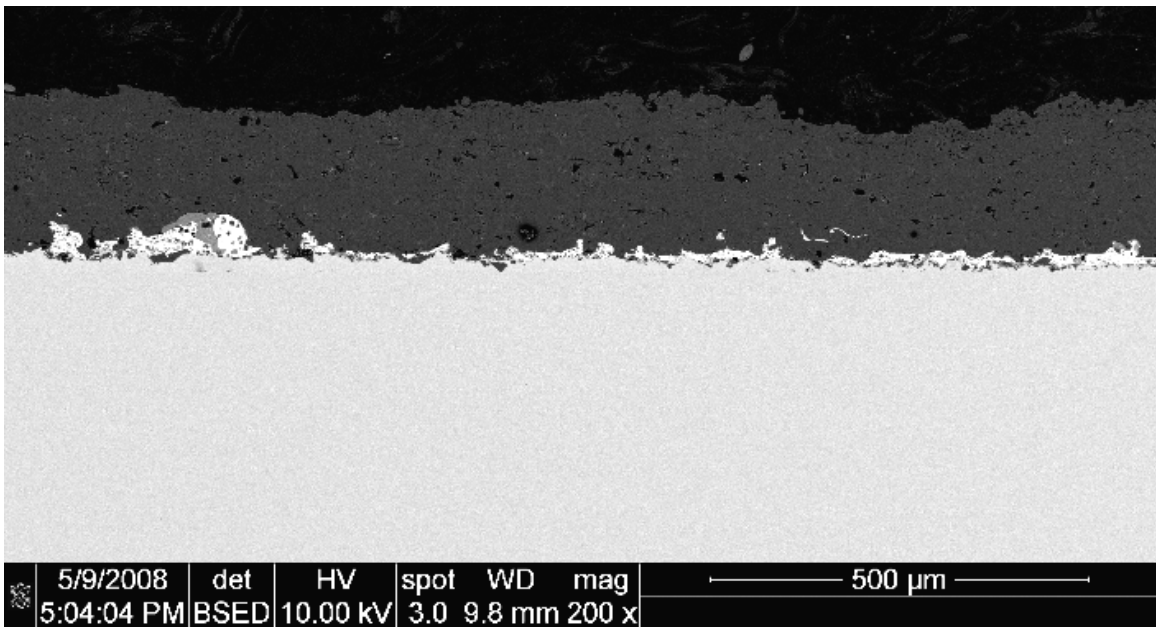
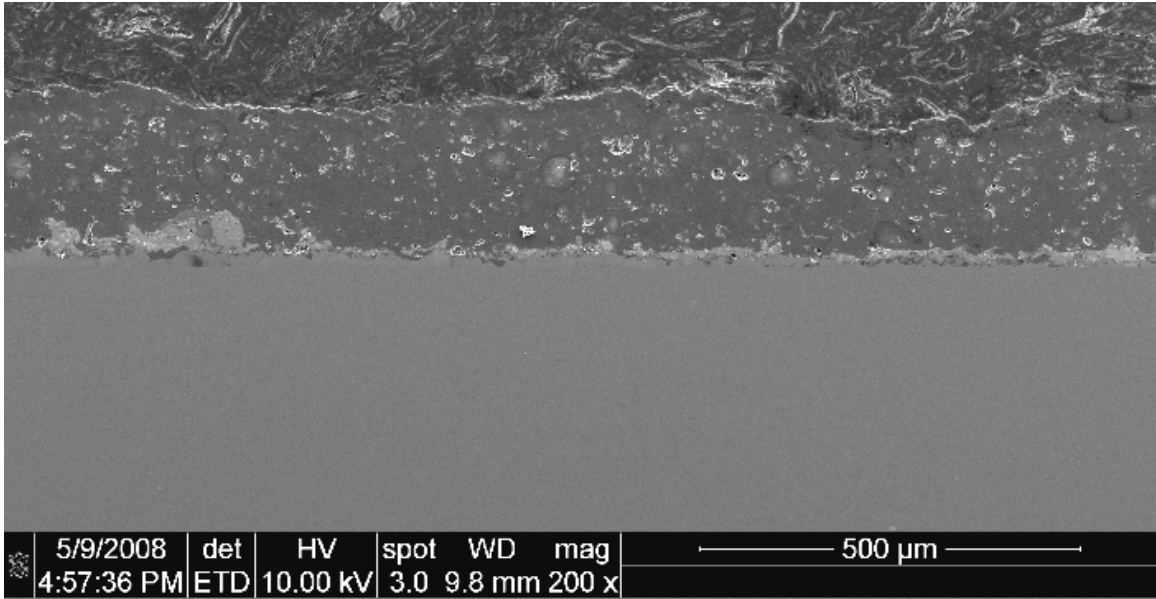


Figure 71: Untested Mag Spinel SEM SE and BSE Images 200x Magnification

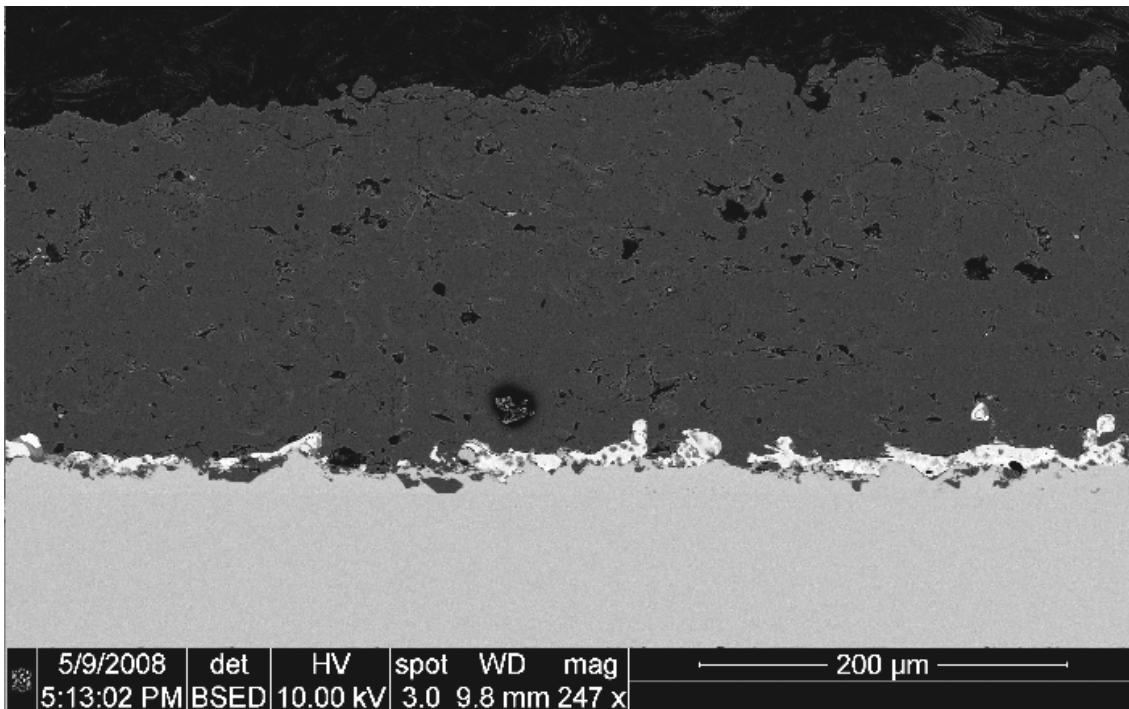
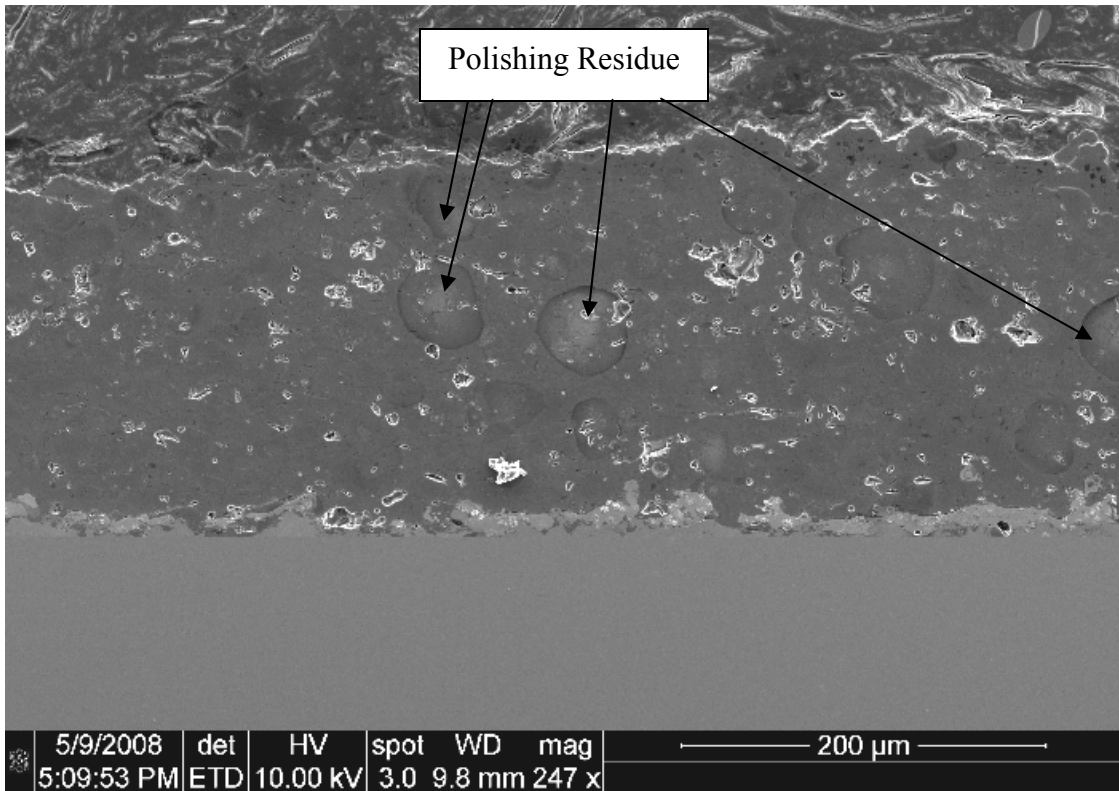


Figure 72: Untested Mag Spinel SEM SE and BSE Images 247x Magnification

The next image, Figure 73, shows the specimen at a magnification of 385x. At this magnification the splat microstructure is still rather difficult to see. By looking at the BSE image (bottom), it is obvious that the microstructure displays the cracks typical of a plasma sprayed TBC. The oily looking splotches on SE detected image (top) are polishing residue.

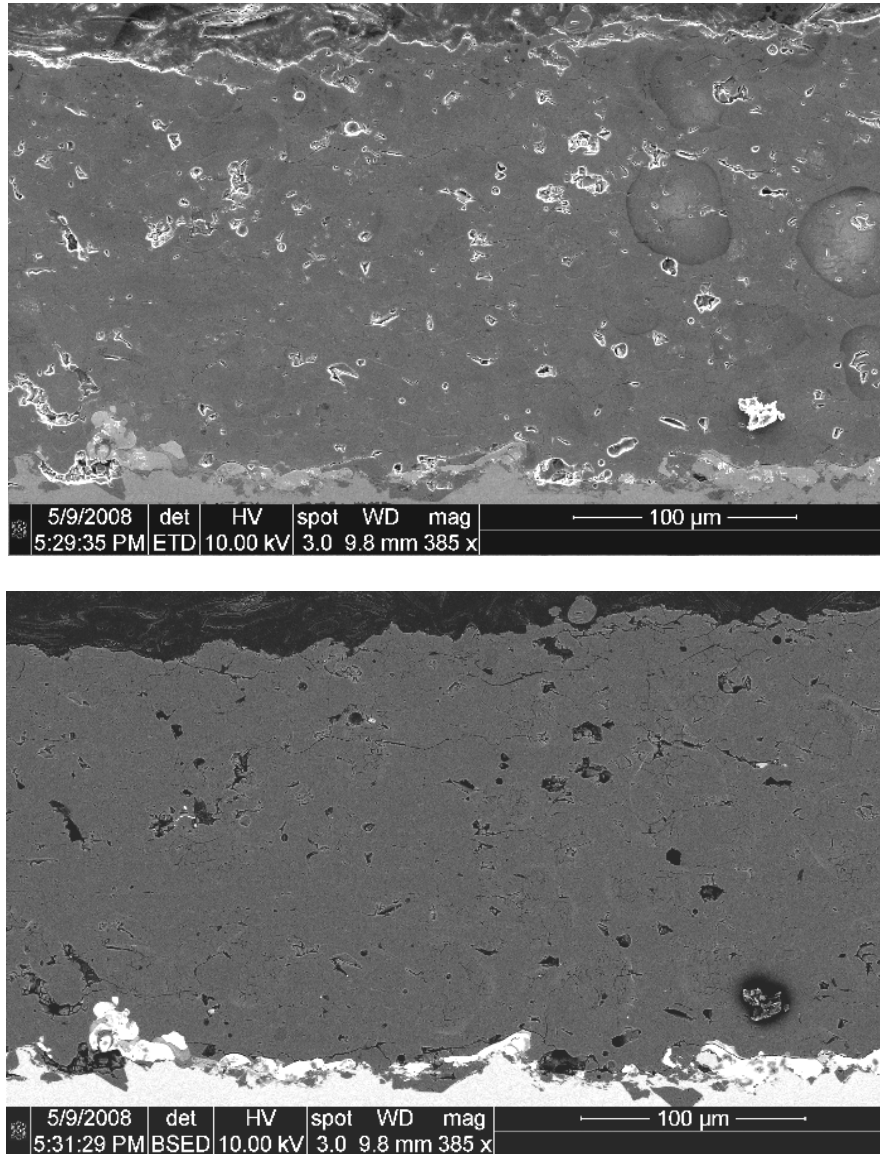


Figure 73: Untested Mag Spinel SEM SE and BSE Images 385x Magnification

Finally, the splat microstructure can be seen for the untested mag spinel coated titanium beam in Figure 74. This SE image at a magnification of 1500x does not need an accompanying BSE image as all the material is comprised of mag spinel. In this image the characteristics of a splat microstructure are apparent. There are large irregular pores that resulted from the manufacturing process. There are also intersplat cracks and pores within the splats. Finally, the perpendicular cracks that are inside of the splats are visible. It should be noted that the cracks are readily visible and that the space between the cracks is extremely clean and tight. The image also shows that the splats have a radial characteristic. It is assumed that this feature occurs as a result of the plasma spray application process when the molten mag spinel particles, which are assumed to be spherical impact onto the substrate and flatten out. It is assumed that more material remains in the center of each splat than on the edge. This leads to the curved splats characteristic of the microstructure.

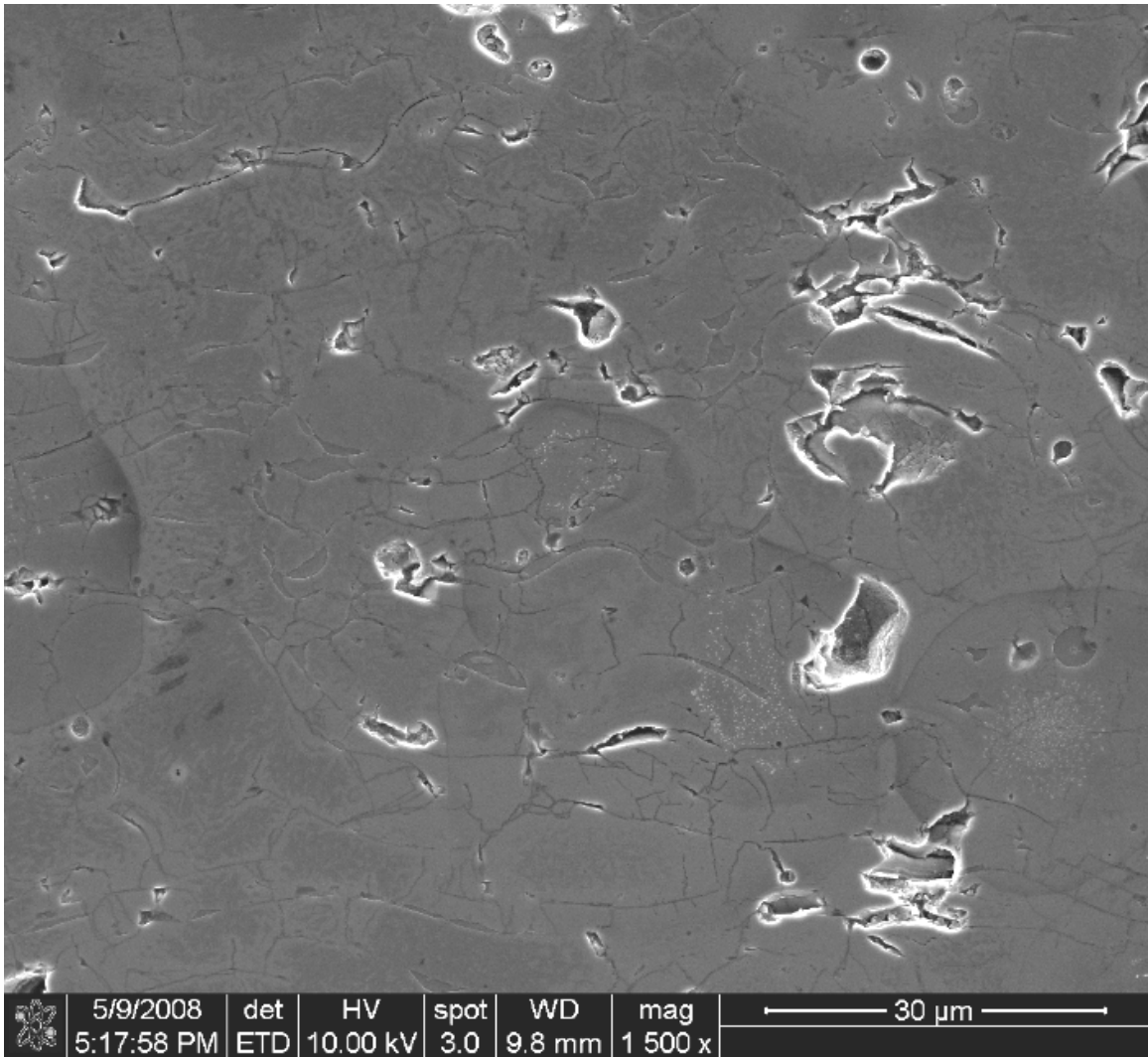


Figure 74: Untested Mag Spinel SEM SE Image 1500x Magnification

Mag Spinel after Deformation near Beam Center.

This next image shows the mag spinel at a magnification of 1603x. Note, that when examining this specimen the microstructure of the tested beam and the microstructure of the untested beam were virtually identical at low magnifications. Therefore, it was deemed unnecessary to capture images at the low magnifications for the

tested beam. This image gives some insight into the mechanical behavior of mag spinel. What should be taken from first glimpse of this image is that the image of the untested specimen doesn't look much different than the image of the tested specimen. The absence of material movement after testing is an indication that mag spinel is a stiff material. The circle in the lower left hand corner of Figure 75 is an area of interest. In this area one can see numerous, very small, vertical cracks in the splats. The fact that the cracks are small and don't grow vertically through the thickness of the splat indicates that the tensile effect in mag spinel is not as dominating as compression.

The other mechanism that can be identified is the fact that the cracks did not widen substantially. This indicates that the splats did not slide over each other. This leads one to believe that the material is also quite strong in the shear direction.

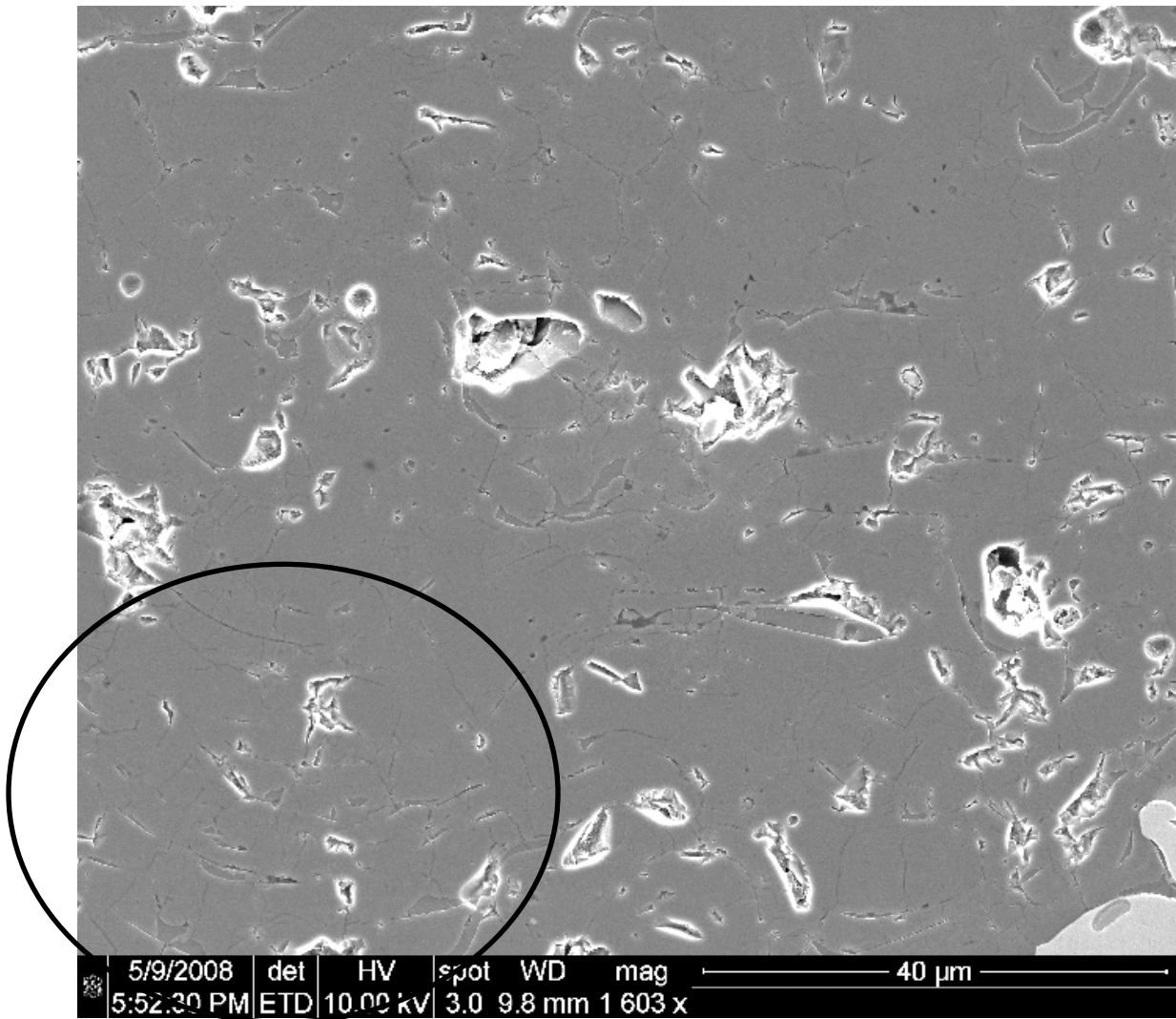


Figure 75: Tested Mag Spinel SEM SE Image Near Center 1603x Magnification

Mag Spinel after Deformation away from Center.

The final image of mag spinel is one after the material has been subjected to 4 million cycles and that was captured away from the center of the beam. The image captured away from the center of the beam is very similar to the image near the center of the beam. One significant conclusion that can be taken from this image is that the plasma

spray process appears quite consistent throughout the coating. Also, the microstructure characteristics are common throughout the coating.

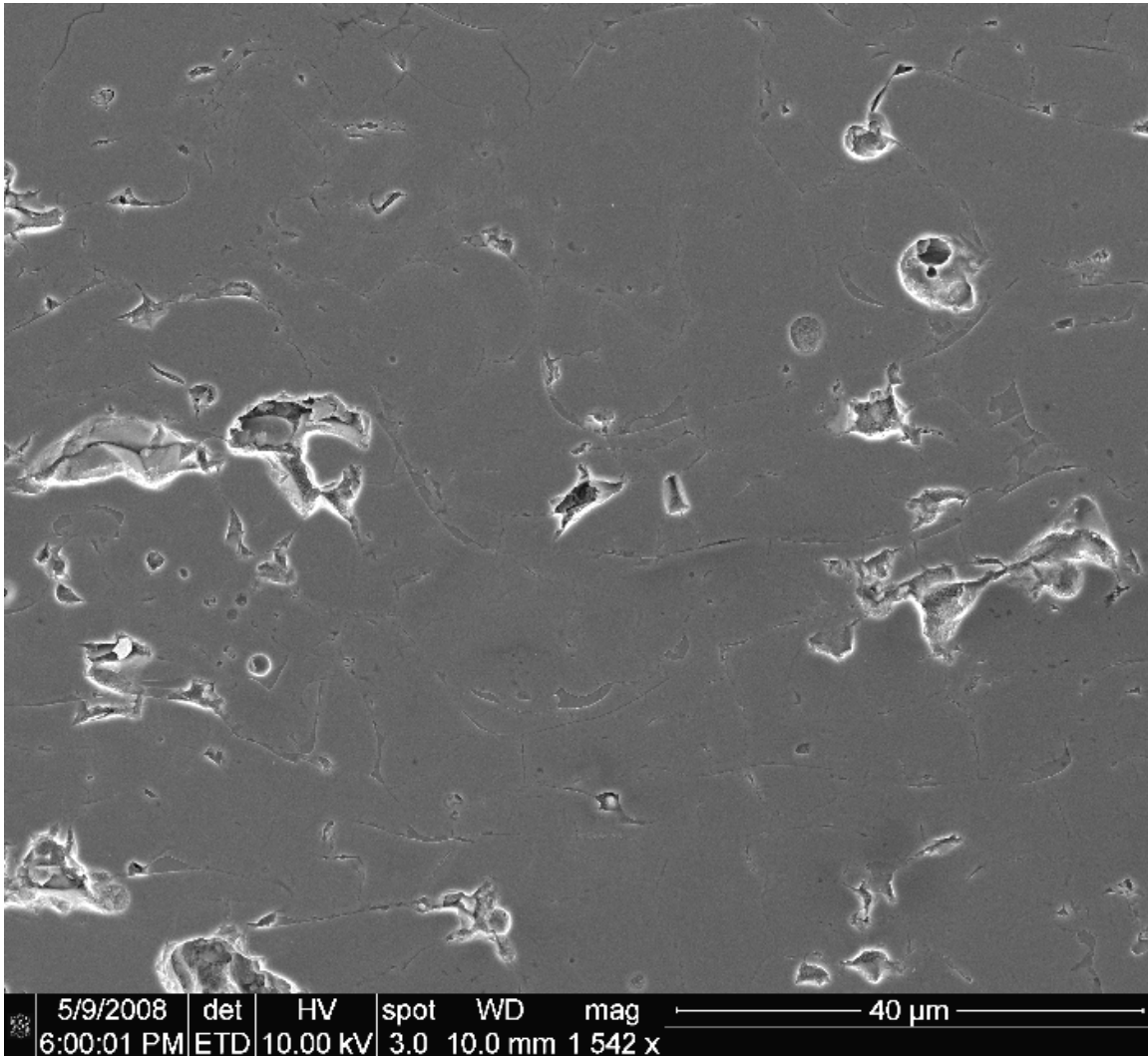
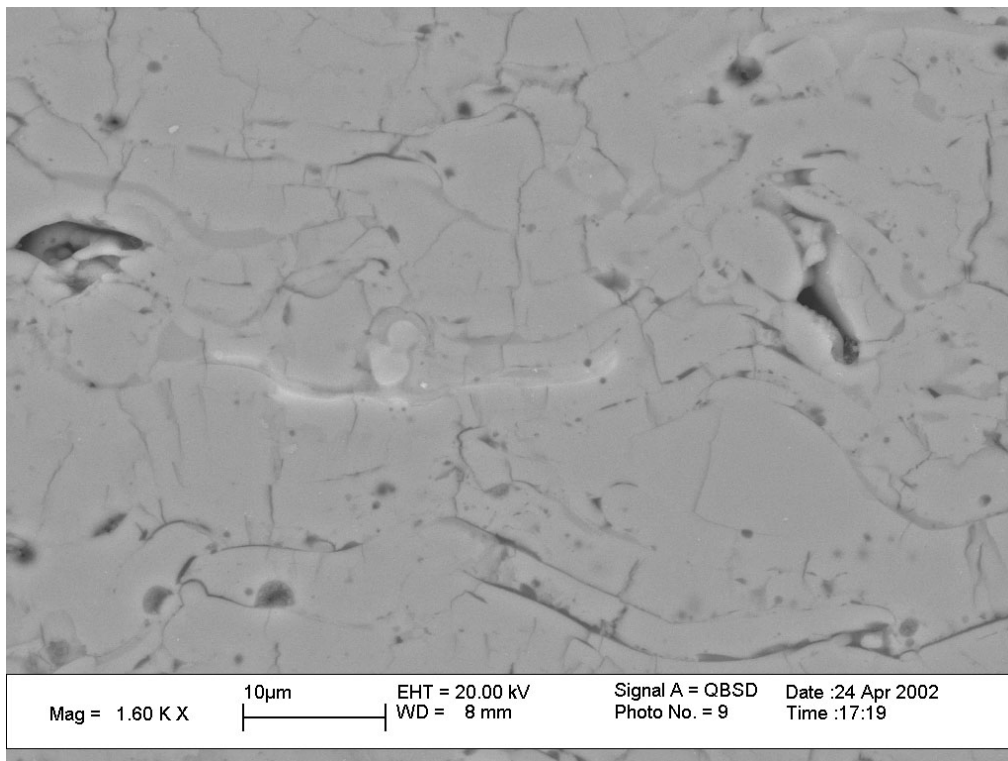


Figure 76: Tested Mag Spinel SEM SE Image Away From Center 1542x

Magnification

Mag Spinel Compared to Previous Studies.

The images of Mag Spinel captured in this study for an untested beam coated with mag spinel show a microstructure that is not readily observable. The images do indicate a typical splat structure common to coatings applied using the plasma spray method. A previous study by Shipton and Patsias indicates that the splat microstructure of mag spinel is readily identifiable at a magnification of 1500x (Figure 77) (Shipman and Patsias, 2003), the same magnification as Figure 74. The well defined splat boundaries are evident in Figure 77. It is thought that the specimen was prepared in a different fashion than the specimens for this study. The authors also experimented with different plasma spray setups altering variables such as spray angle and particle size.



**Figure 77: Previously Captured Mag Spinel 1500x Mag
(Shipman and Patsias, 2003)**

YSZ before Deformation.

The next material to be examined is the yttria stabilized zirconia with NiCrAlY bond coat over titanium. This material exhibits the same type of material behavior as the mag spinel but has a lower stiffness and lower damping characteristics. Figure 78 shows a 200x magnification of this coating. It is apparent, even at this low magnification, that the microstructure is made up of the splat boundaries. The top figure is the image produced by the SE detector. The BSE image already indicates that the coating has a much higher crack density than the mag spinel. The relative insignificance of the bond coat can be seen in this coating. It is important to note that a much higher crack density can be observed in these two images than could be observed in the mag spinel images at the same magnification.

The next highest magnified image, 367x, is shown in Figure 79. In this set of images, both the images, SE detected and BSE detected, show a distinct crack system in the material. Also present are the irregular pores that are a product of the plasma spray application process.

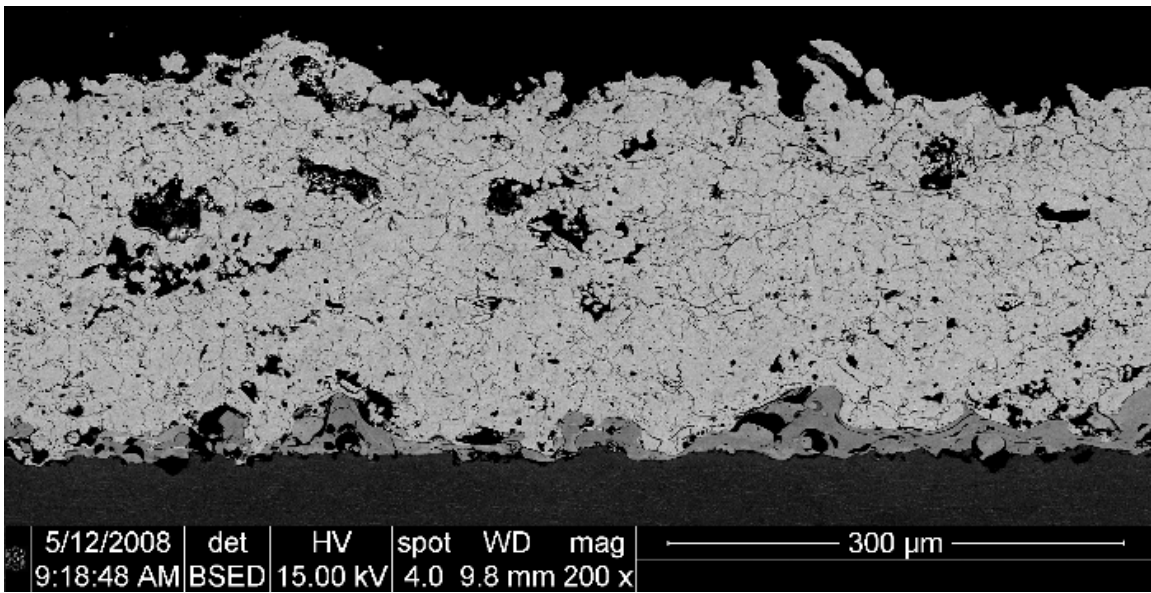
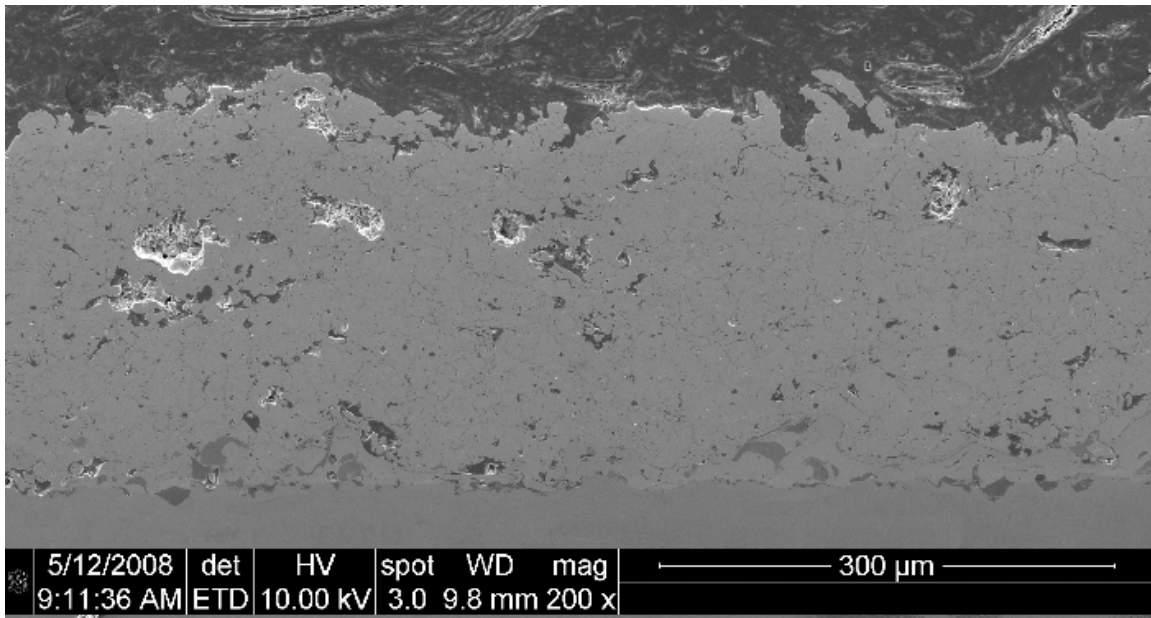


Figure 78: Untested YSZ SEM SE and BSE Images 200x Magnification

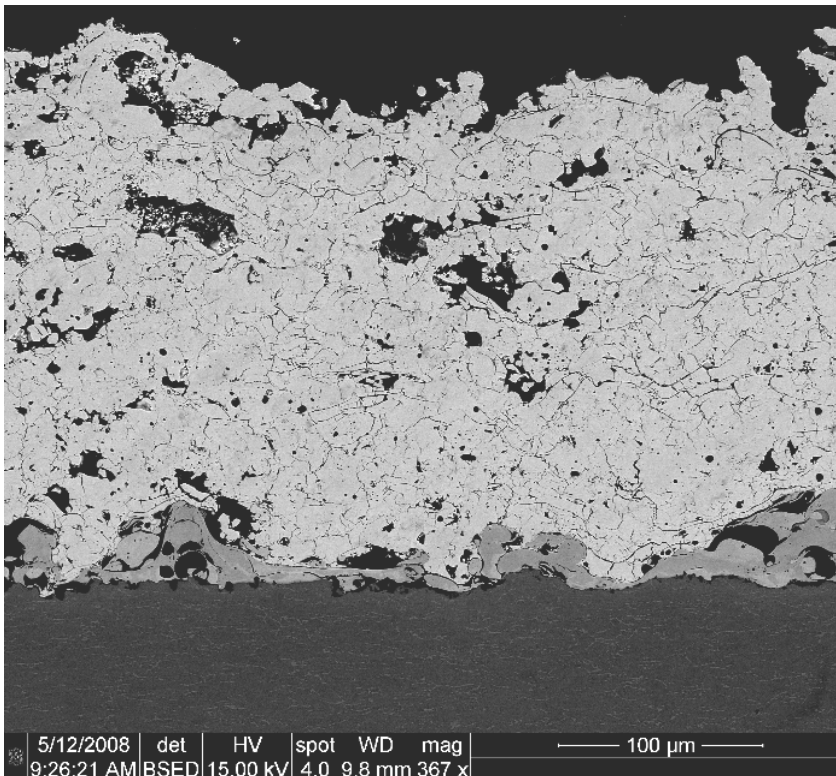
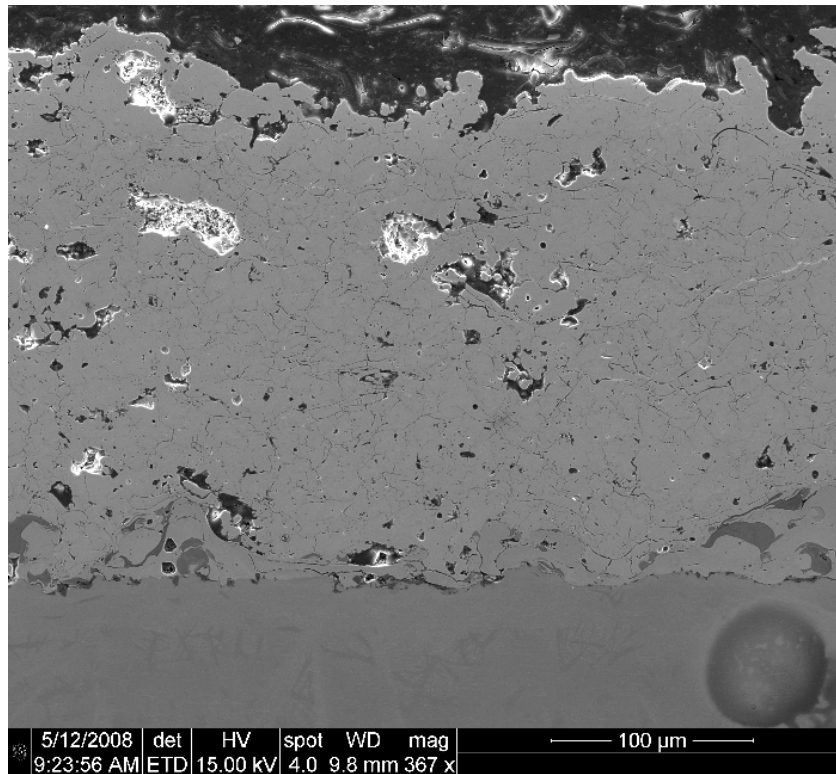


Figure 79: Untested YSZ SEM SE and BSE Images 367x Magnification

Finally, the last image captured by the SEM was SE detected and shows a distinct microstructure. This image has all of the characteristics of a coating applied using the plasma spray process: irregular pores, intersplat cracks, perpendicular cracks and pores within splats. It is expected that after 4 million plus cycles, this microstructure, due to the low stiffness observed for YSZ, will alter through crack generation and expansion of space between cracks.

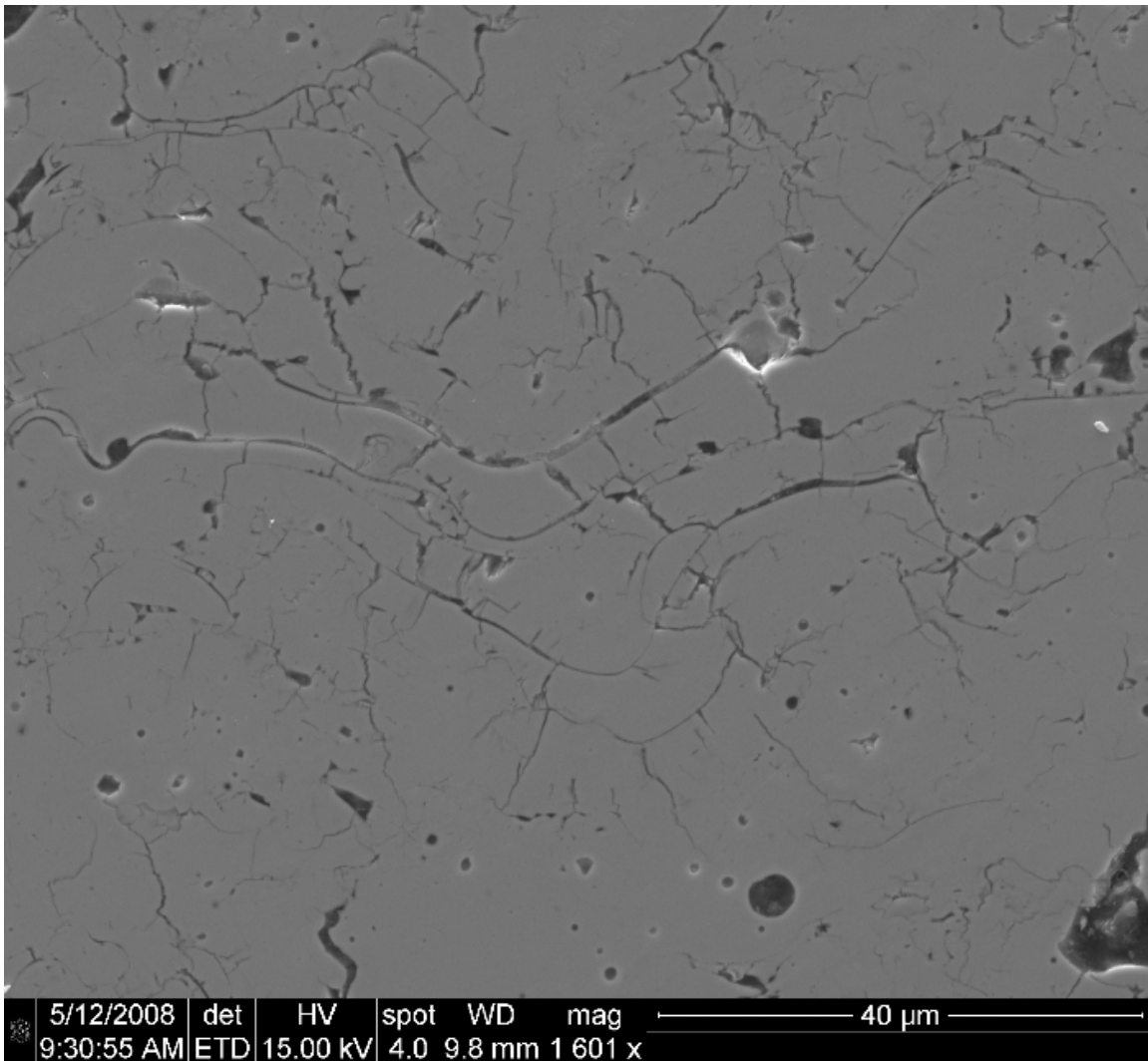
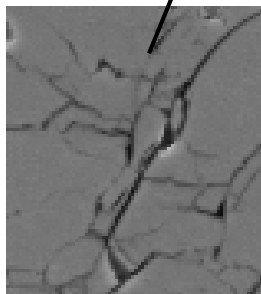
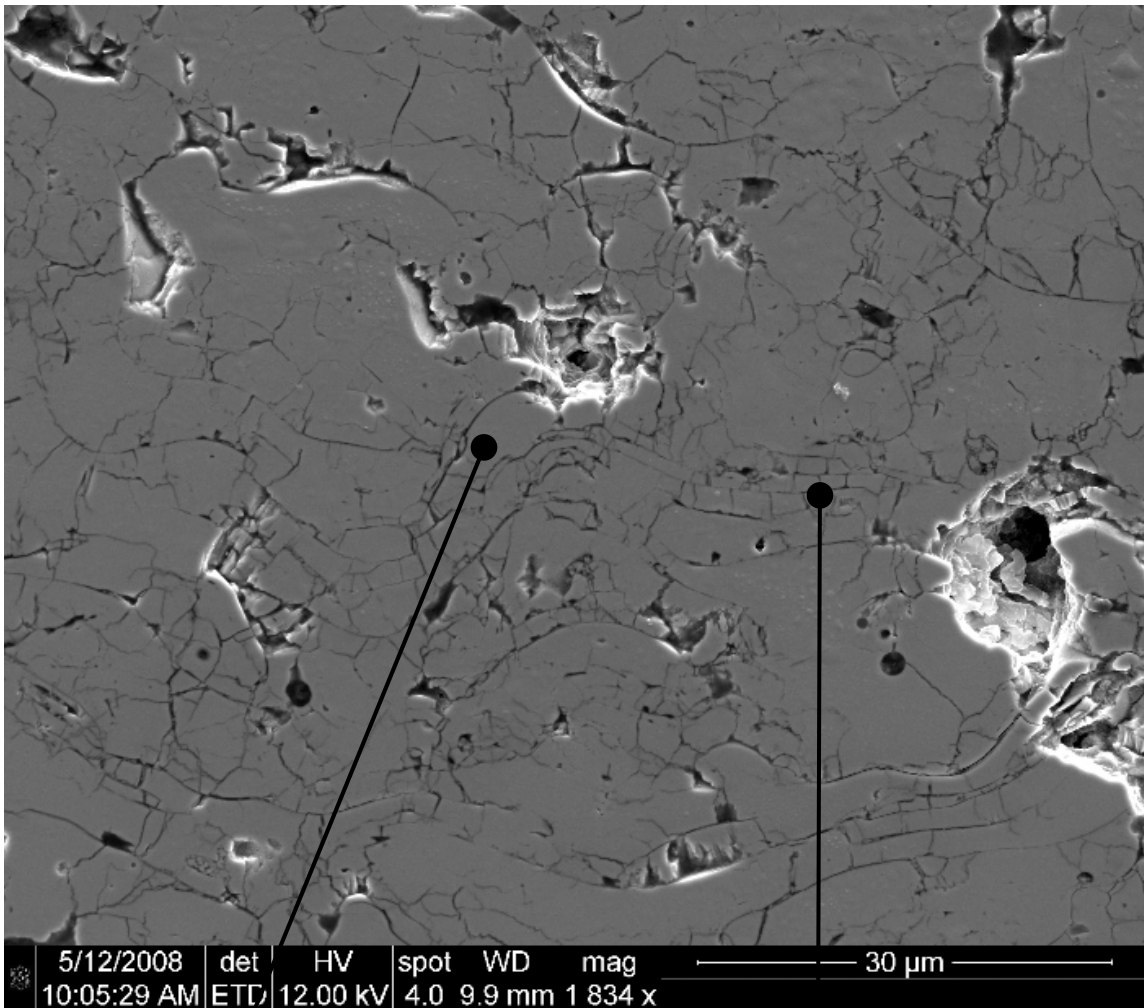


Figure 80: Untested YSZ SEM SE Image 1601x Magnification

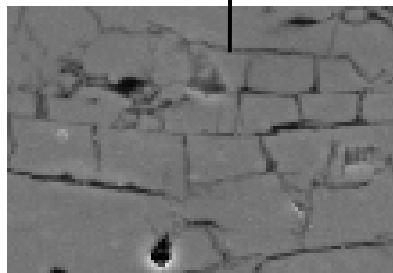
YSZ after Deformation near Beam Center.

The first image that will be examined is the image of the YSZ specimen at 1834x magnification captured in a section near the center of the beam where the highest strains are expected. The difference in magnification between the following images and the untested specimen is not significant. What is significant is that the scales of the three images are similar. The lower magnification images captured for the untested beam were not captured in this section. This was because the images did not look different for tested and untested beams at the lower magnifications.

The image, Figure 81, shows a complex crack structure. This image was captured near the center of the beam. It can be seen that large network of cracks has formed. This image shows cracks growing vertically, almost entirely through the thickness of the splats. The image also shows a widening of the cracks. This two observations lead to two conclusions. First, the crack generation through the thickness of the splats indicates that YSZ is not as stiff in tension as the mag spinel. This can be confirmed by the lower coating modulus values shown by YSZ in the experimental portion of this study. The second conclusion is that YSZ is not as strong in shear as mag spinel. This is evidenced by the widening of the horizontal cracks throughout the specimen. This indicates that the splats have less resistance to slide over one another. These two results are indicators that the loss factor for YSZ is expected to be higher than the loss factor for mag spinel. This can be observed in the experimental data in Figure 67.



Crack Separation



Crack Generation

Figure 81: Tested YSZ SE Image Near Beam Center 1834x Magnification

YSZ after Deformation near Beam Center.

The final SEM image to be examined is that of a cross section subjected to a high number of cycles away from the highest strains at the center of the beam. The area in Figure 82 that is surrounded by the circle appears to be an extremely thick splat. This could point to a process defect in the plasma spray application. Perhaps this could be a result of a YSZ particle that was larger than the rest of batch used in the process. The horizontal cracks in that splat cannot go through the entire thickness of the splat and therefore could reduce the damping effectiveness of the coating.

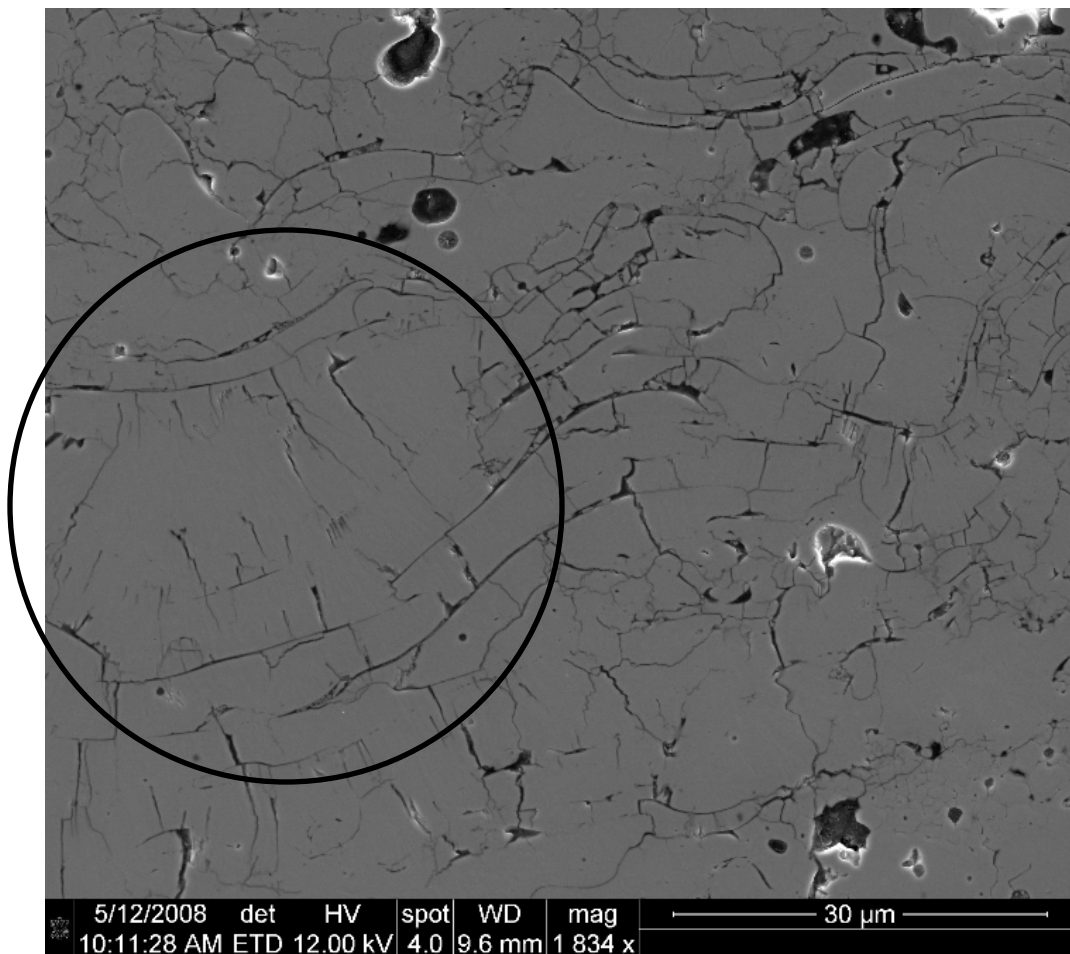


Figure 82: Tested YSZ SE Image Away from Beam Center 1834x Magnification

YSZ Compared to Previous Studies.

The images of plasma sprayed YSZ captured in this study agree with the images captured in previous studies which also investigated plasma sprayed YSZ at the microstructure level. The characteristics of a splat microstructure are apparent. Figure 83, Figure 84, and Figure 85 show the material at various magnifications. In the images at the highest magnification (Figure 83 and Figure 84) the microstructure displays the typical splat structure. The image at the lower magnification (Figure 85) displays the YSZ material's high crack density which was observed in this study. Also on display is the bond coating and the irregular surface which the YSZ adheres to, to form a strong bond with the substrate.

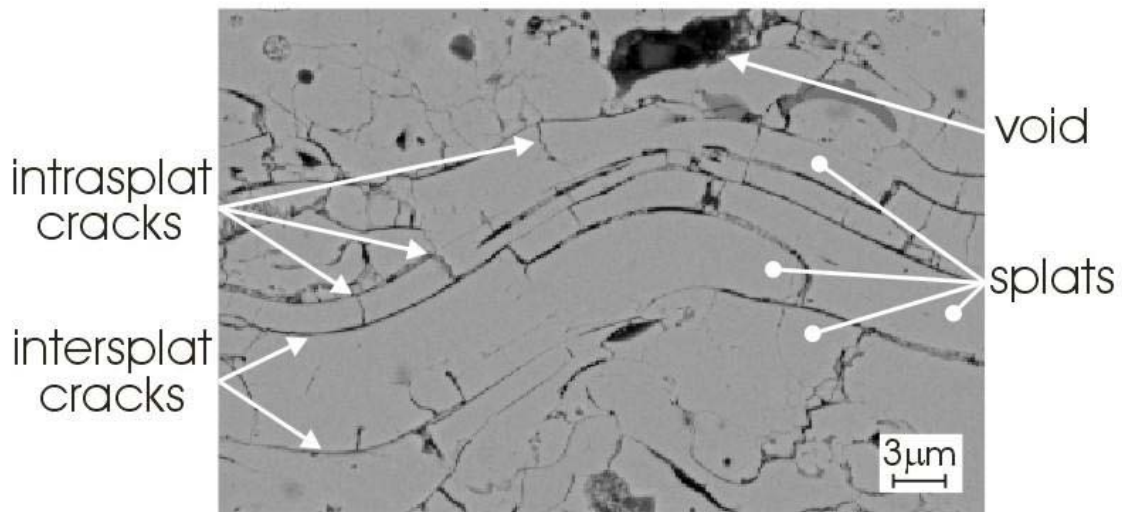


Figure 83: Image of YSZ with 3 um Scale (Tassini et al., 2005)

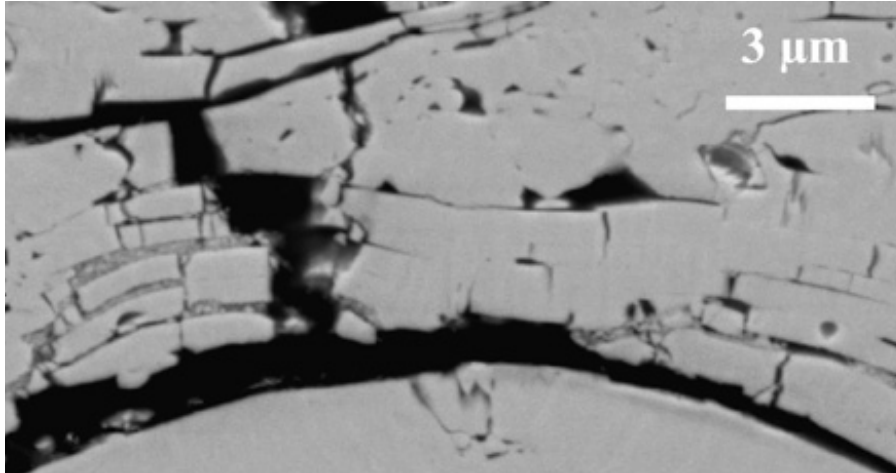


Figure 84: Additional Image of YSZ with 3 um Scale (Tassini et al., 2007)

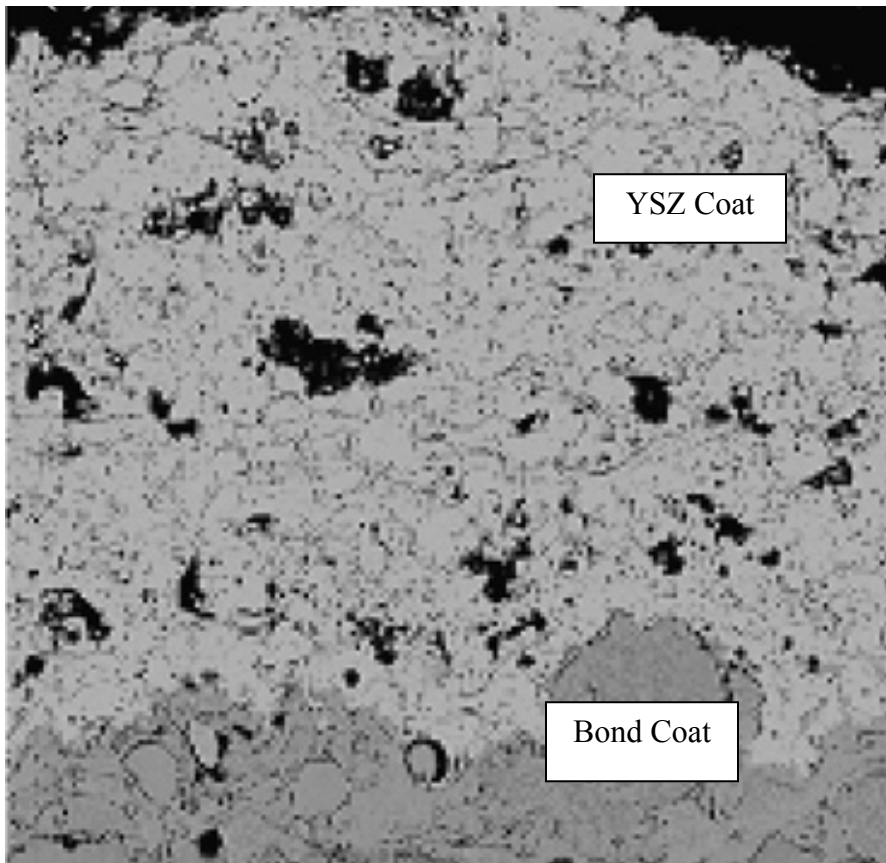


Figure 85: Figure of Bond Coat and YSZ Coating (Tassini et al., 2007)

V. Conclusions and Recommendations

Conclusions

After testing each beam in a vacuum, the results indicate that each coating provides a significant amount of damping over an uncoated beam. The mag spinel loss factor was $\eta = 0.058$ at a strain of $442\mu\epsilon$, the damping ratio was $\zeta = 0.029$ and the quality factor was $Q = 17.24$. The YSZ values at $583\mu\epsilon$ were: loss factor $\eta = 0.098$, damping ratio $\zeta = 0.059$ and quality factor $Q = 10.2$. The addition of either material greatly improves the damping characteristics over the bare beam. In this study, the YSZ has over twice the loss factor of mag spinel. The mag spinel, however, is over twice as stiff as YSZ for all the reported strains. The mag spinel modulus values range from 62.5 GPa to 47.3 GPa while the YSZ modulus values range from 27.7 GPa to 15.4 GPa. The values calculated for YSZ were determined using data that was highly variable. This variability is an indication that the trend line used to calculate the numbers may not accurately describe the material.

Adjusting the sweep rate did not lead to results that point out, definitively, which rates were better suited for generating data. Sweep rates of 0.5 Hz/min, 5.0 Hz/min, 10 Hz/min and 20 Hz/min were all compared and all values were within 5% of one another for a beam coated with mag spinel. The results did not indicate a true pattern related to sweep rate. The results also indicate that the material is has a dependency on time

history. This dependency may have been eliminated if the material had reached steady state during the cycle build up portion of the experimentation.

The bare beam data also produced results which could indicate that the free decay method leads to better bare beam material property results than the forced response method. The bare beam loss factor data recorded using the free decay method was half the value measured using the half-power method. This is closer to the ideal no damping value of zero. The bare beam data produced in this study, generated using the half-power method, produced coating loss factor results that were nearly 6% lower when compared to the coating loss factor results using the bare beam data generated using the free decay method.

To add to this observation, it should be noted that the type of data collection method, forced response or free response, could have an impact on material property results. The results obtained via the free response test could not be replicated using the forced response test.

The titanium beam coated with magnesium aluminate spinel and bond coat yielded the following results:

1. The resonant frequency increased when exposed to a high number of cycles
2. The material resonant frequency decrease as input voltage is increased
3. The material loss factor reaches a maximum value of 0.058

The titanium beam coated with YSZ and bond coat yielded the similar, although not identical, results:

1. The coated beam also increases resonant frequency as it accumulates cycles

2. The material reaches a nearly constant coating modulus value
3. The material loss factor reaches a maximum value of 0.098
4. The coating modulus indicates a much less stiff material but had a higher loss factor

As was stated in the opening paragraph, both beams provided a significant source of damping over the bare beam in the vacuum.

It was also noticed in the study that, the hard ceramic coatings possessed extremely similar traits in terms of material properties. The coating modulus and loss factor especially trended in similar fashions. The main difference between the two materials was the magnitude of these two factors.

The difference in the two materials could also be seen on a microscopic scale. It was noticed that mag spinel had a microstructure that was very dense. The microstructure before and after testing did not lend itself to being easy to find a “typical” splat makeup. This dense structure was probably one of the reasons that the stiffness of mag spinel was more than 2.5 times higher than the stiffness of YSZ. The YSZ microstructure was extremely easy to observe in terms of a typical splat structure. This feature had also been noticed in other research efforts. This material’s microstructure underwent a transformation between the tested and the untested specimen in terms of crack generation and crack widening.

The main finding of this report came when the experimental data was correlated with the microstructural mechanics. The experimental data showed that mag spinel had coating modulus values that were more than two times higher than the YSZ coating

modulus values. When a mag spinel specimen was placed in the SEM the microstructure on an untested coating was easily seen at a magnification of 1500x but not at lower magnifications. A tested specimen didn't show much change except that vertical cracks were generated that did not stretch very far into the splat. For YSZ the experimental findings revealed that the material had lower coating modulus values than mag spinel and that YSZ had a higher loss factor. In the SEM, YSZ displayed a microstructure that was readily apparent even at lower magnifications before and after testing. After testing, the crack density greatly increased and horizontal cracks widened.

Processing this information leads to the conclusion that the materials gain their damping abilities from the cracks that are produced through use due to the friction that takes place along these interfaces. The YSZ is less stiff than mag spinel and has a higher loss factor; this can be attributed to the fact that the material has numerous cracks before loading and after loading the damping ability increases as cracks are generated through use.

Recommendations

After performing this study there are quite a few recommendations that can be made. First, if the homogeneous coating needs to be separated into two distinct coatings, one layer of bond coat and one layer of top coat, it is important to correctly size the elements. This means that the model should be composed of extremely small elements

with low aspect ratios. Due to the random nature of the bond coat, the only appropriate way to model this layer would be to do so from a statistical point of view.

Another FE recommendation is that the damping properties be included in the initial model. In this model the damping characteristics were not a model input. This may help in creating a more accurate model of the TBC coated titanium. One of the only programs that use the damping properties as an input value is NASTRAN. Therefore, NASTRAN should be used in an iterative fashion to see how much impact damping has on resonant frequency. If this effect is not great then the program doesn't need to be used throughout the analysis.

The next recommendation to aid in a correct bond coat/top coat model is to weigh and measure the beams after each coating is applied. This should be accomplished with a scale and a caliper that possess a high degree of accuracy. With these almost minute amounts of material being applied to a large object measurement accuracy is key to an accurate model. After each coating is applied the thickness of the coating should be measured and the beam plus coating should be weighed. This is important in determining the correct material properties.

In addition to measurement issues it is recommended that the beams be subjected to high strains for the sine sweep tests. It is extremely important that these tests be carried out to determine the correct model for the coating. One characteristic that needs to be strictly controlled is the electromagnetic force applied to the beam. It was noticed during this test that the beam would exhibit different responses depending on the location

of the electromagnet with respect to the magnets adhered to the beam. A study should be done to determine the optimum placement of the beam with respect to the magnet.

Another aspect of this report that needs further study is the impact of each assumption on the final result due to error accumulation. In this report error was shown to occur in several calculations. This error was a result of the bare beam nonlinearity exhibited in the half-power loss factor results, the variation in coating modulus and loss factor due to sweep rate, the use of a constant value for Poisson's ratio, and the exclusion of damping property input. These errors, by themselves, may only add errors in the 2%-6% range but as a combination may compound on each other and lead to rather high errors in the final material property calculations.

Finally, testing should be conducted that examines the beam microstructure at several intervals as cycles accumulate. At these intervals, the loss factor and coating modulus should be determined as well as the microstructure observed. These intervals should show an increase in crack density and an increase in damping effectiveness. The beams should also be strained to much higher strain values to determine whether or not the greatest damping is limited to $500\mu\epsilon$.

Appendix A: VibrationVIEW Setup Procedure

The purpose of this appendix is to show the procedure that is used when setting up the VibrationVIEW program to build up cycles, phase track and finally to perform input sweeps.

The first step in setting up a test is to open VibrationVIEW by clicking on the appropriate icon on the Window's Desktop. This opens the VibrationVIEW Screen. To begin a test you would click on New Test and choose the sine test option in that screen. Then you would click on the settings button to begin the test setup. Figure 86 shows the screen after following those steps.

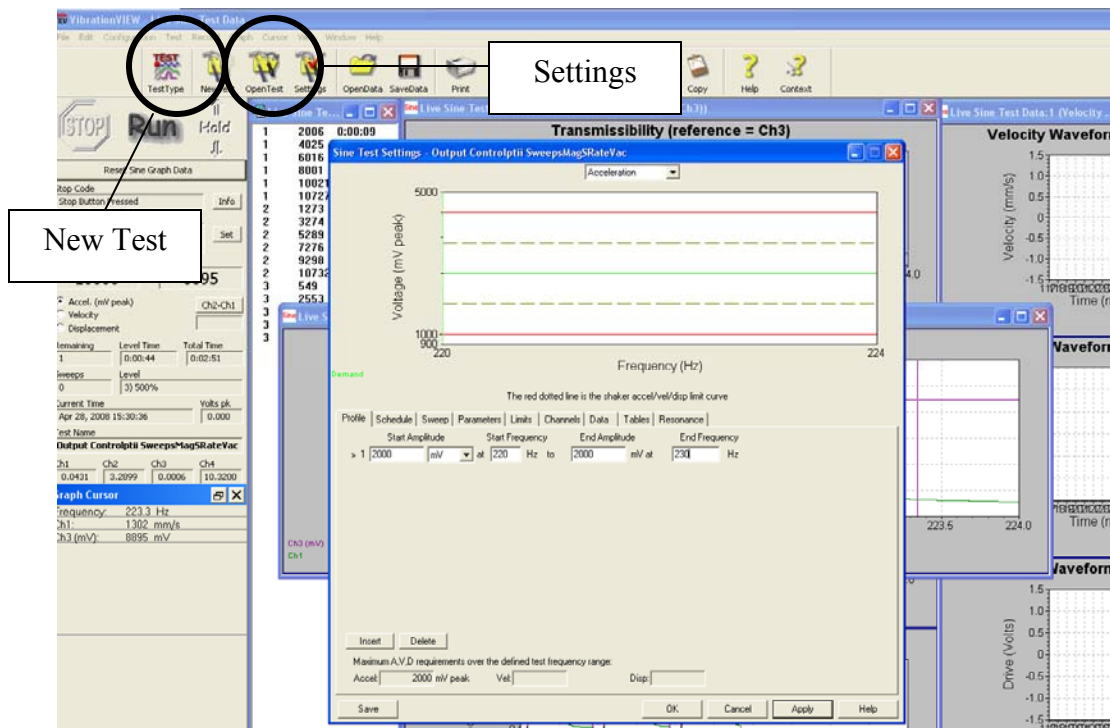


Figure 86: Test Setup Screen Shot

The first tab that needs to be filled out is the Profile tab. This screen is where the both the input voltage and frequency range is input into the test. This is the amount of voltage that goes into the amplifier which in turn drives the electromagnet.

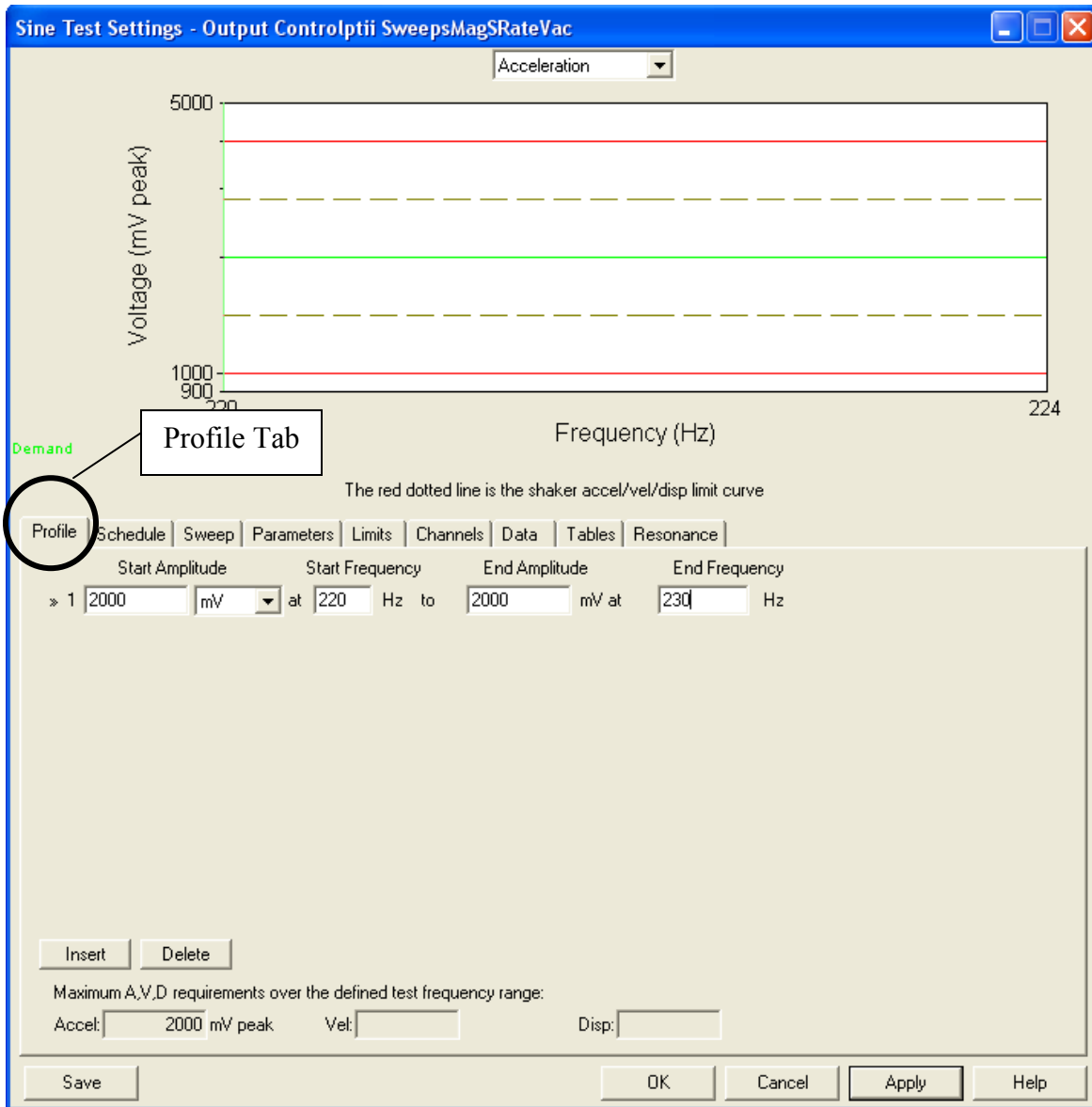


Figure 87: Test Settings Profile Tab Screen Shot

The next tab is where the schedule is determined. The schedule can be setup for cycle build up or for doing input voltage sweeps. In Figure 88 the schedule is setup to do input voltage tests. The level start column indicates the type of function that is being performed with VibrationVIEW. In this case a sine sweep from high frequency 224 Hz for one sweep is being performed for each row. The modified column heading indicates the voltage that will be input into the electromagnet. Each percentage is a percentage increase, in this example, in voltage. The schedule will be followed until the final sweep is performed.

It is also possible in this tab to put a step in between the sweeps that lets the user identify the resonant peak and to perform phase tracking for a set amount of cycles. The procedure for this function will be explained in subsequent paragraphs.

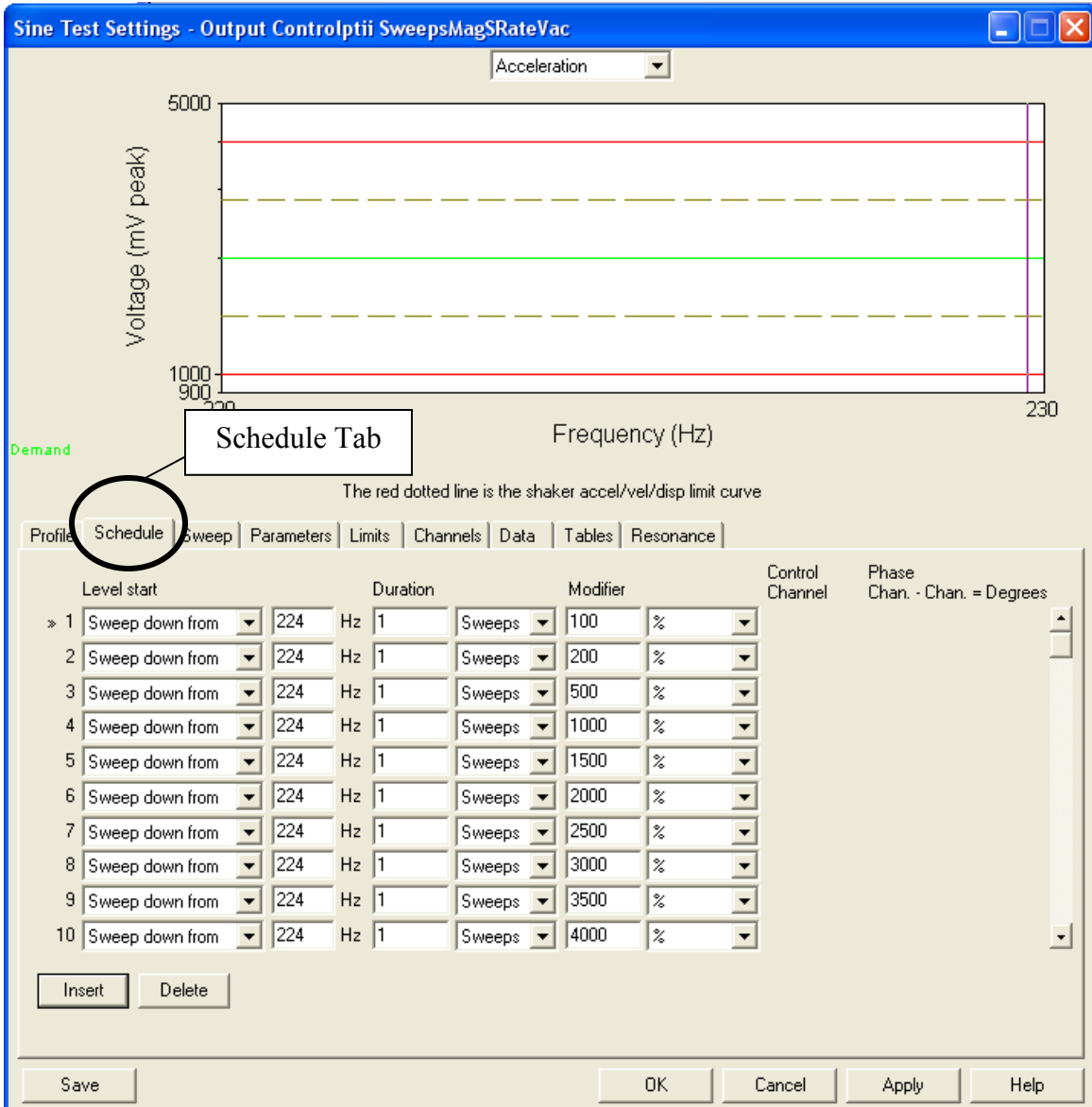


Figure 88: Test Settings Schedule Tab Screen Shot

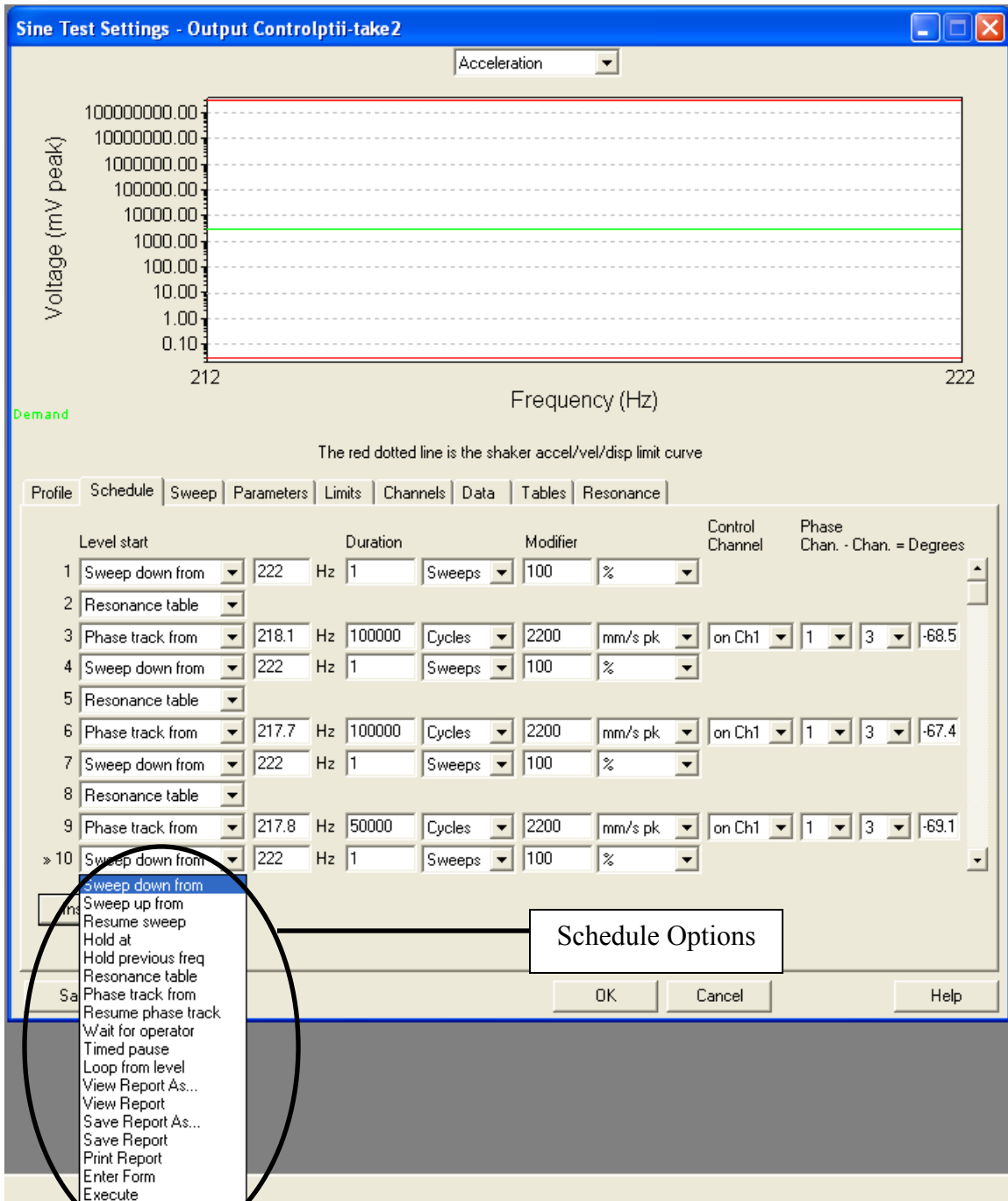


Figure 89: Options for VibrationVIEW Schedule

The sweep tab is the section in which the user can define the sweep rate for the test. In this instance the test is going to be performed at 5 Hz/min.

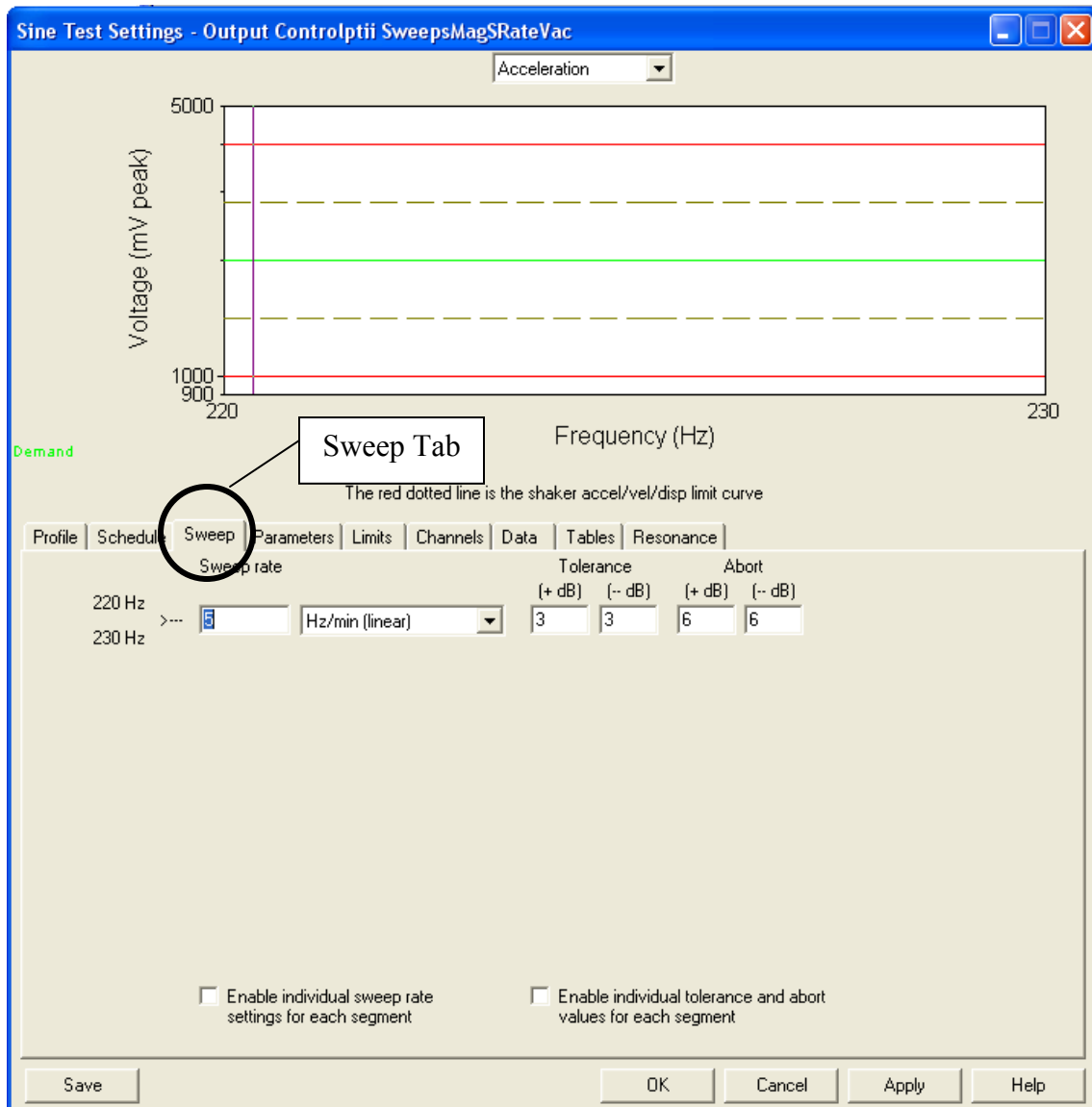


Figure 90: Test Settings Sweep Tab Screen Shot

The Resonance tab is important for the phase tracking while trying to stay in resonance. The selection parameters tab is overridden when the resonance option is selected in the schedule so this tab is only important for control parameters. This box has options for sweep rate and feedback gain. This determines how long it takes for the beam to reach resonance. It also determines how sensitive the program is to adjusting input to the electromagnet. If the feedback gain is too fast then the input signal is always chasing the output signal. If the gain is too slow the input signal reaches the output signal too slowly.

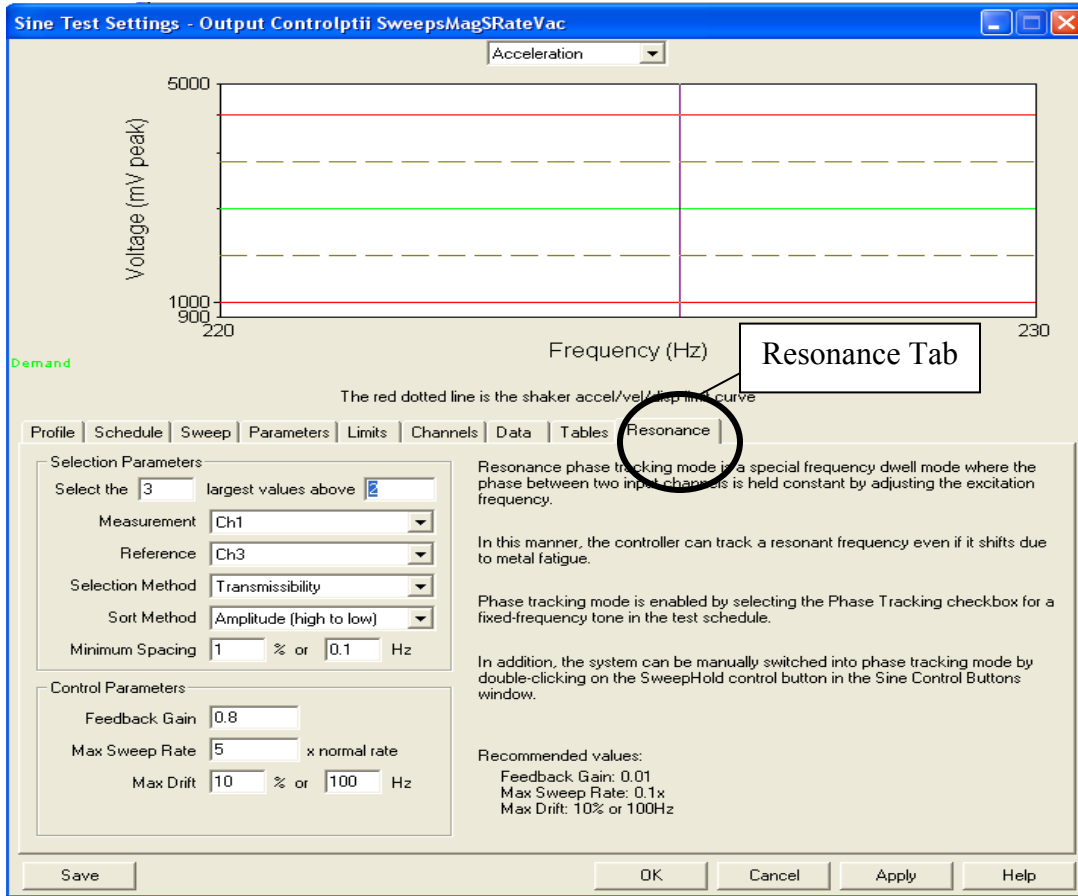


Figure 91: Test Settings Resonance Tab Screen Shot

Figure 92 shows the down sweep result which is achieved when the schedule is set, the sweep rate is input, the input voltage is set and the beginning and end frequency is determined.

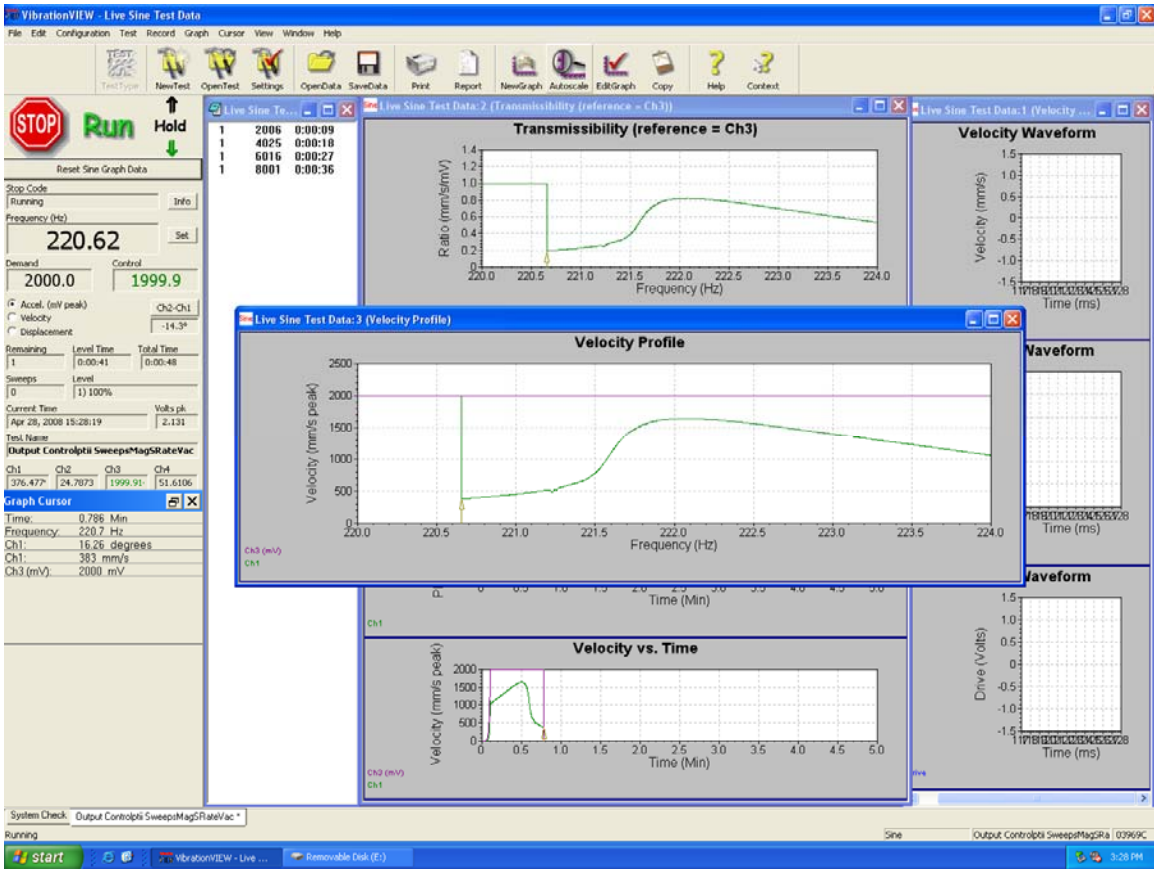


Figure 92: Sweep Down Test Screen Shot

If the resonance option is selected between sweeps in the schedule tab, the screen in Figure 93 will appear at the end a sweep. This screen identifies the resonant frequency in Hertz. To begin building up cycles at resonant frequency it is necessary to check the box next to the frequency which is filled out.

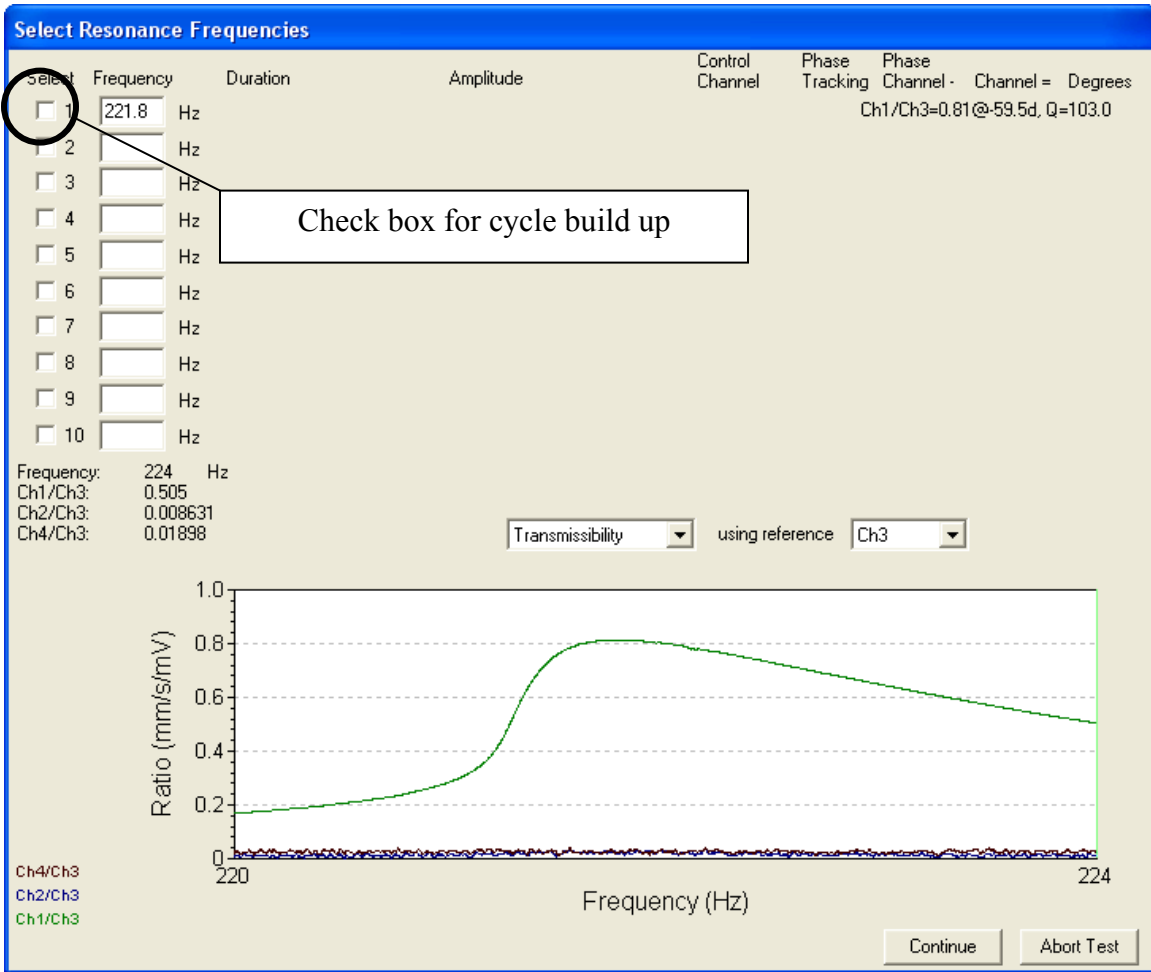


Figure 93: Resonant Frequency Selection Screen

When the box is checked it is possible to put in the number of cycles desired for the portion of the test. It is also possible to determine the response that is desired for the beam. This is input under the amplitude tab. In the example the 2200 mV peak indicates a velocity of 2.2 m/sec is desired to be recorded by the LDV which is Channel 1. In order to get the beam to stay at resonance and to maintain a 2.2 m/sec velocity at the center of the beam it is necessary to check the Phase Tracking box and to note the value of degrees. In this example the degree value is -59.9° . This is the phase difference

calculated by the VibrationVIEW software that needs to be maintained between Channel 1, output, and Channel 3, input, for the beam to stay at resonance.

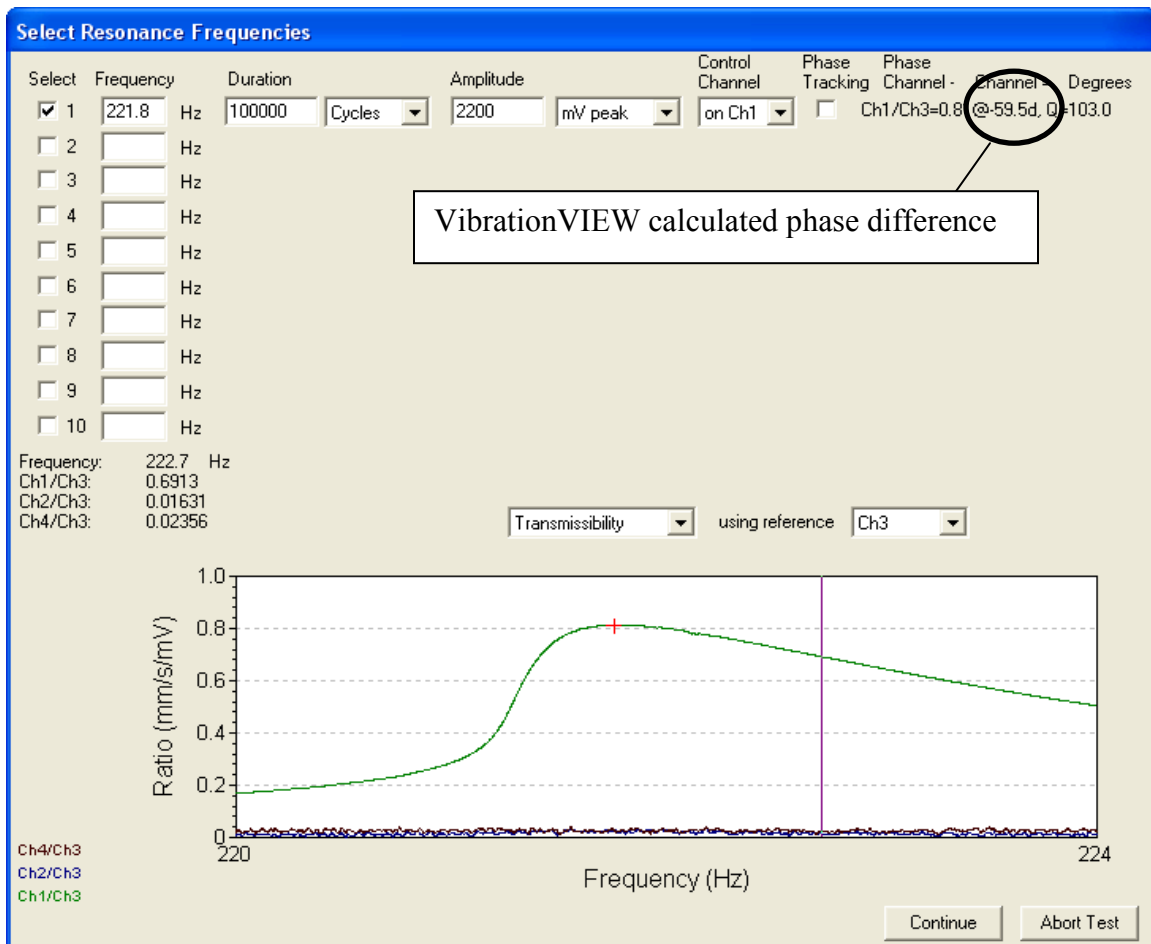


Figure 94: Resonant Frequency Selection Screen Cycles and Amplitude

By clicking on the phase tracking box the two channels that are desired to maintain a certain distance apart in terms of degrees can be determined. The -59.9° is input at this point. The Continue button can be selected and the test will continue until the next sweep or until the end of the test for the desired number of cycles, at resonance, with the center maintaining a desired velocity.

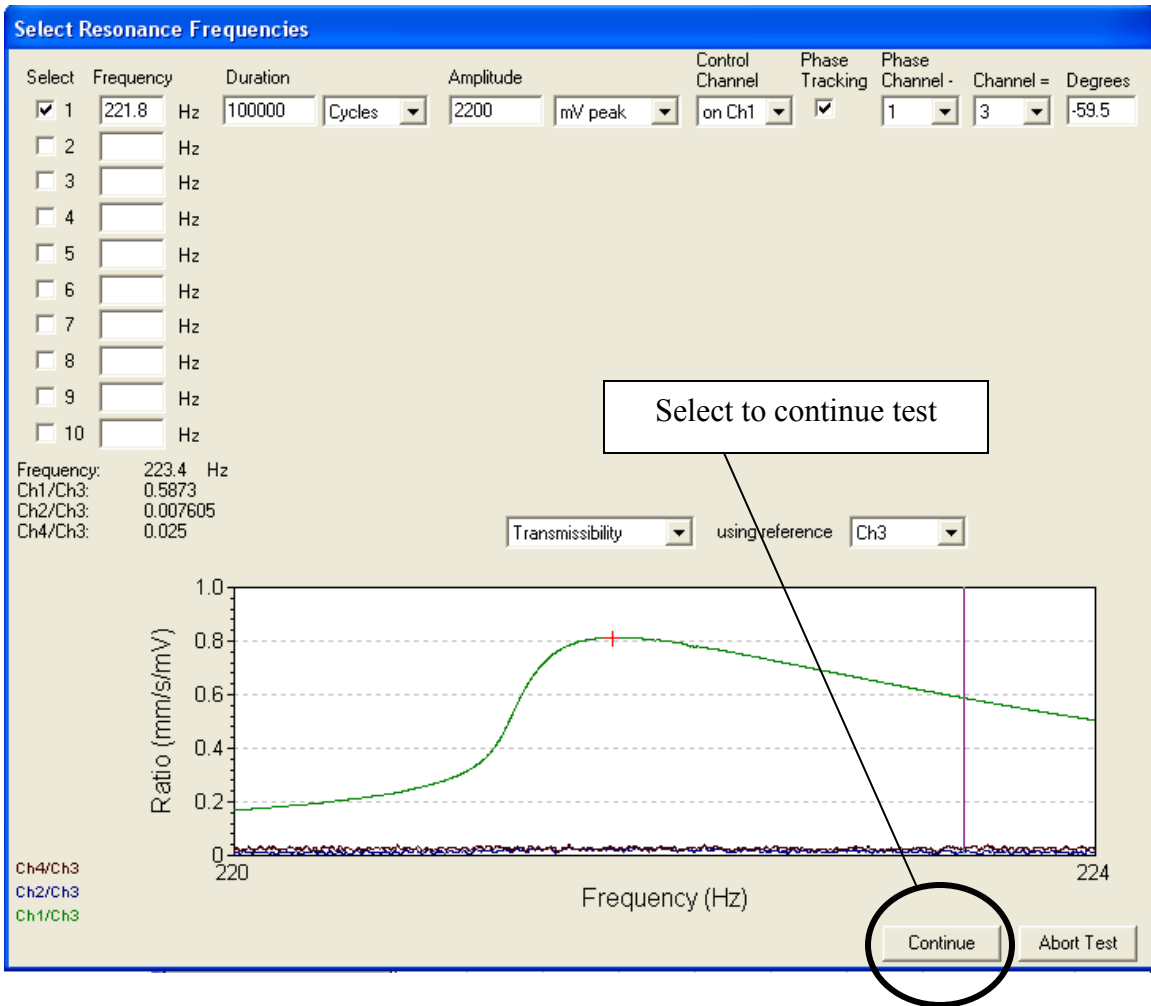


Figure 95: Resonant Frequency Selection Screen Phase Tracking

Figure 96 shows how the phase tracking helped maintain a constant beam velocity. The dark line represents the input voltage and the light line represents the measured beam velocity. The constant velocity maintained by the beam during cycle accumulation is represented by horizontal lines that line at 2.2 m/sec. As one can see, the input voltage begins at a value of 2 volts and gradually increases as the cycles accumulate. This represents the strain hardening of the beam. The means that more input voltage must be added to the system to generate the desired beam response. The lower image in Figure 96 shows, in more detail, the sweeps that took place between cycle

buildup segments. For the sine sweeps, a 3 volt input was applied to the beam producing a 2.2 m/sec velocity at the center of the beam.

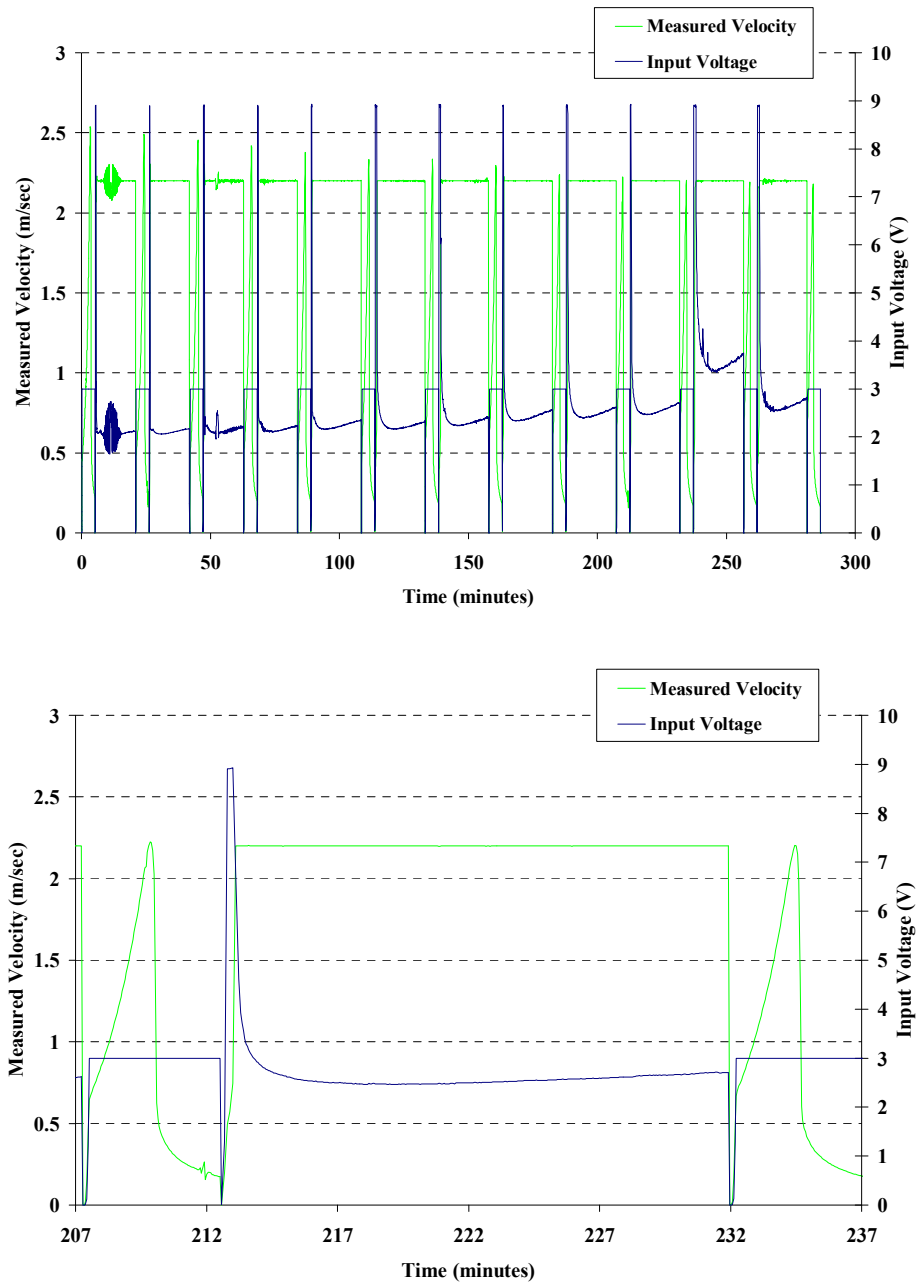


Figure 96: Phase Tracking with Cycle Build-Up

Appendix B: YSZ Material Property Curves

The first curve fit, via the add trendline function in Microsoft Excel, characterizes the relationship between coating modulus and frequency. A second order polynomial was generated to represent this relationship.

$$\text{YSZ: } E_c = 0.0182\omega^2 - 5.8052\omega + 439.65 \quad (17)$$

The relationship between the modulus and the frequency depends on using units of GPa for modulus and Hertz for frequency.

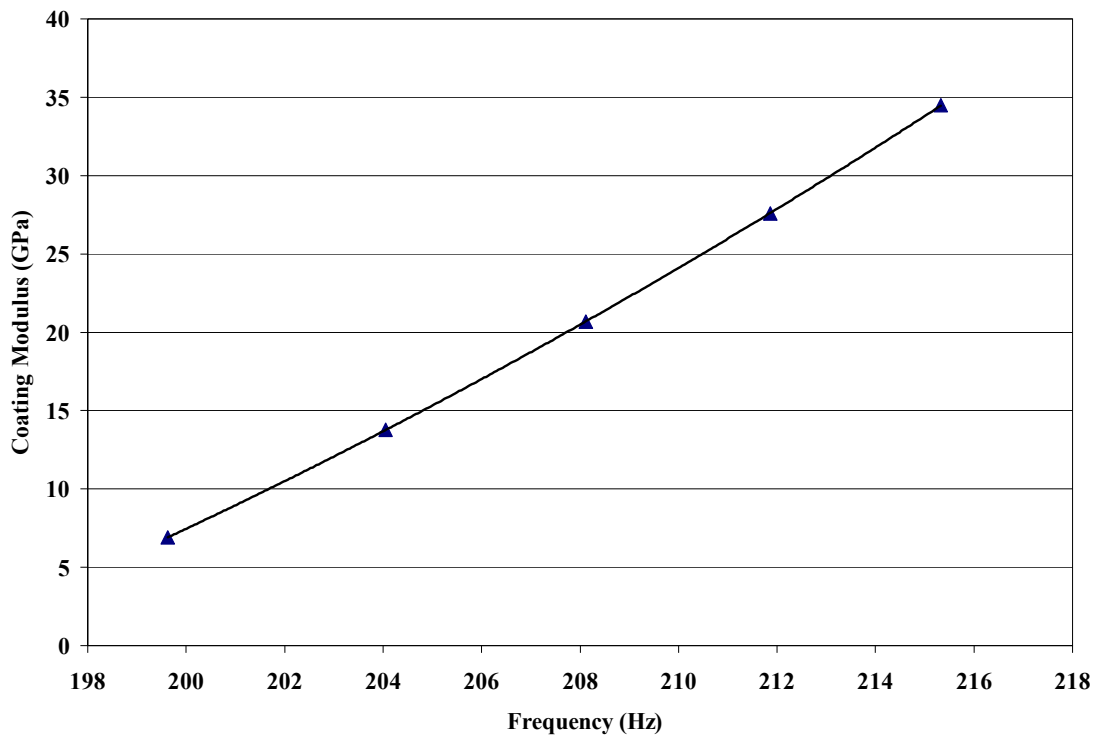


Figure 97: YSZ Storage Modulus Relationship to Frequency

The next relationship in Figure 98 relates coating modulus to mode shape.

Visually the graph makes sense in the fact that as the material stiffens through increased storage modulus the beam deflects less. The relationship is given for both materials.

$$\text{YSZ: } X(L/2) = -5\text{E-}06E_c^2 + 0.0011E_c - 0.5452 \quad (18)$$

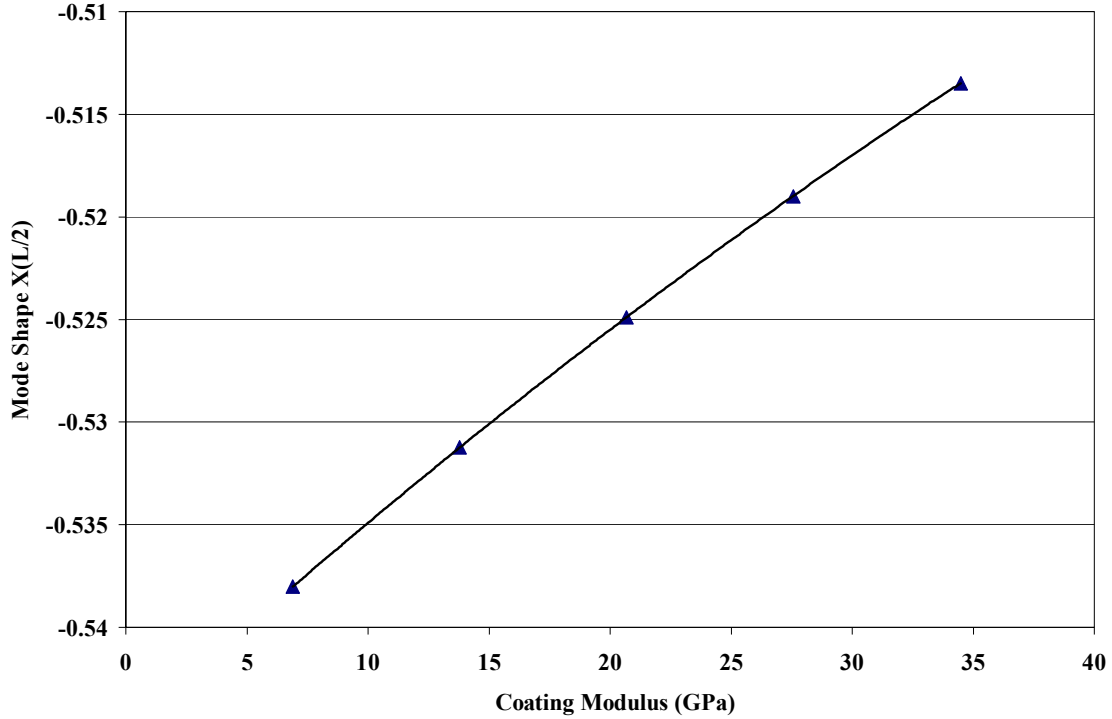


Figure 98: YSZ Mode Shape Relationship to Coating Storage Modulus

The next equation generated is the relation between coating modulus and normalized reference strain. As previously stated the reference strain is located at the coating/beam interface. The strain at this point is a normalized value which will be related to actual strain in a subsequent section. The equations generated by the points in Figure 99 are:

$$\text{YSZ: } \tilde{\epsilon}(L/2) = 2\text{E-}07E_c^2 - 5\text{E-}05E_c + 0.0087 \quad (19)$$

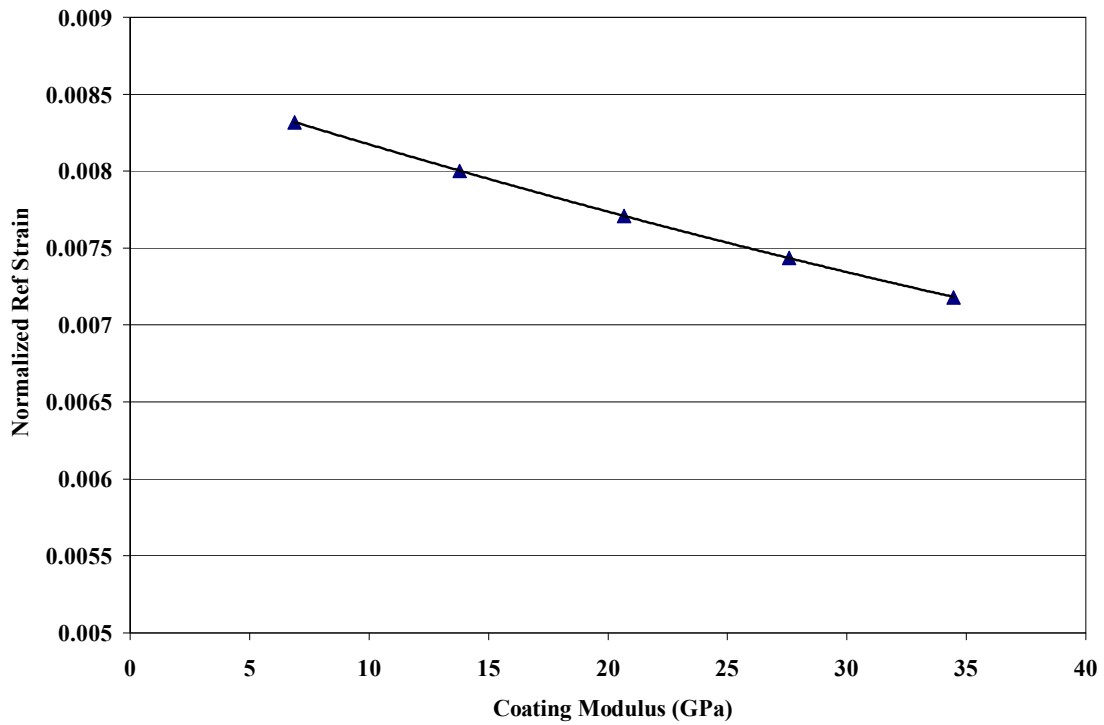


Figure 99: YSZ Normalized Reference Strain Relation to Coating Storage Modulus

The final relationship generated by the finite element analysis is the relation between strain energy ratio (SER) and coating modulus. This ratio is the value that relates strain energy in the coating alone to the strain energy in the coating and beam system. These equations relate SER to coating modulus.

$$\text{YSZ: SER} = -6\text{E-}05E_c^2 + 0.0065E_c + 0.0049 \quad (20)$$

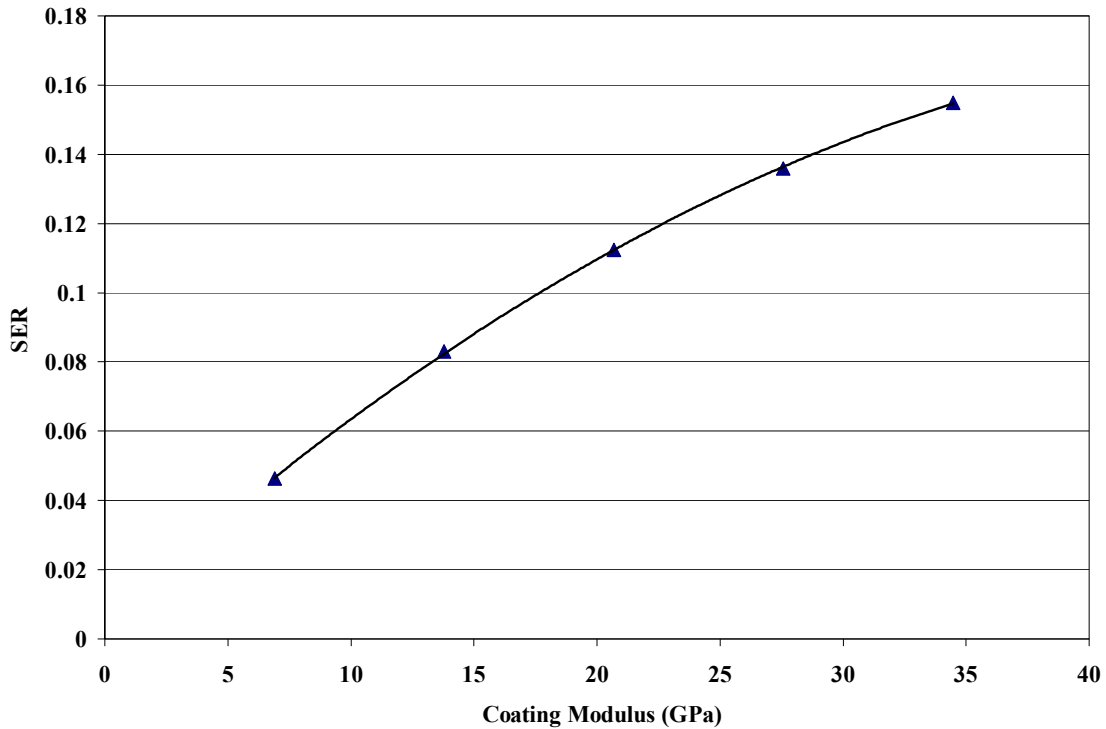


Figure 100: YSZ Strain Energy Ratio Relation to Coating Storage Modulus

Apply Experimental Data to Finite Element Model.

The next step in generating material properties is inserting experimental data into the equations produced through the curve fitting. This step applied the data generated by the input sweeps in the lab to the equations for the three beams with either mag spinel or YSZ as a coating. The following curves were generated using the data collected for a YSZ-bond coat beam.

The first curve in Figure 101 shows the relationship between measured velocity and coating modulus. It appears from this graph that the material has yet to achieve its maximum response. Had this happened the graph would have approached,

asymptotically, a particular coating modulus value. In future research it is recommended that the beam be tested at higher strain amplitudes. This would ensure that the coating would be sufficiently loaded and exhibit its' material properties to the fullest.

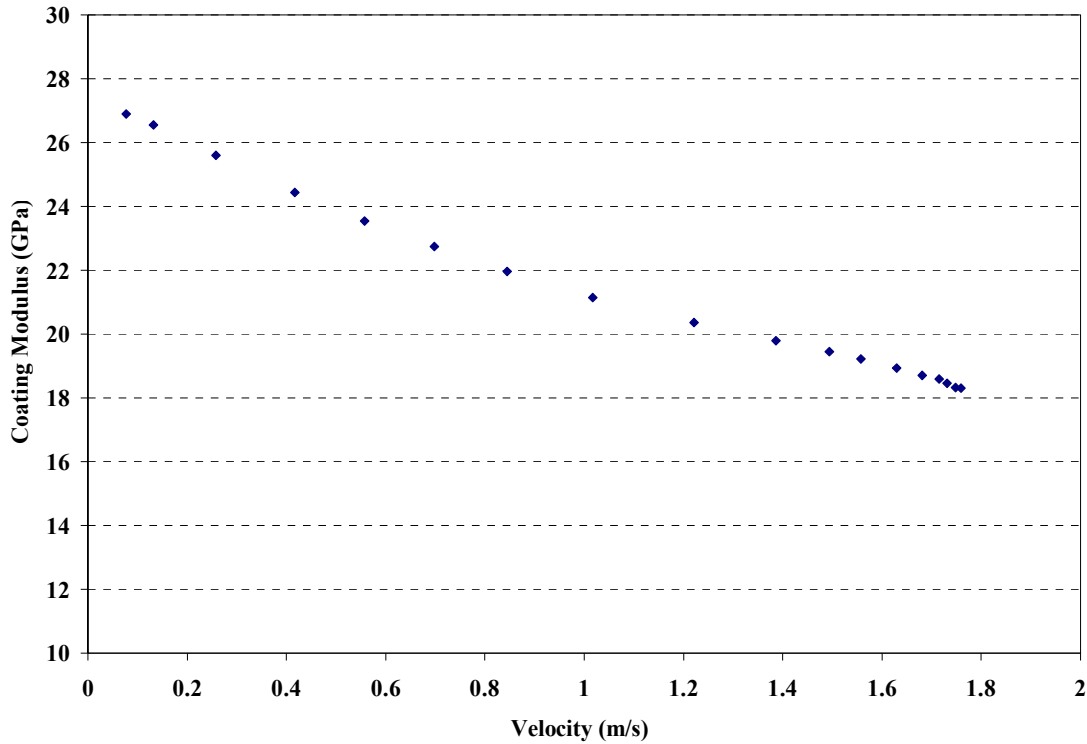


Figure 101: YSZ Coating Modulus vs. Beam Measured Velocity at L/2

The next relationship generated is between the recorded velocity at the center of the beam and the strain energy ratio. This figure shows that as the response increases the strain energy ratio decreases. This could be due to the strain energy in the coating decreasing, the strain energy in the beam increasing or the strain energy in the beam increasing faster in the beam than in the coating.

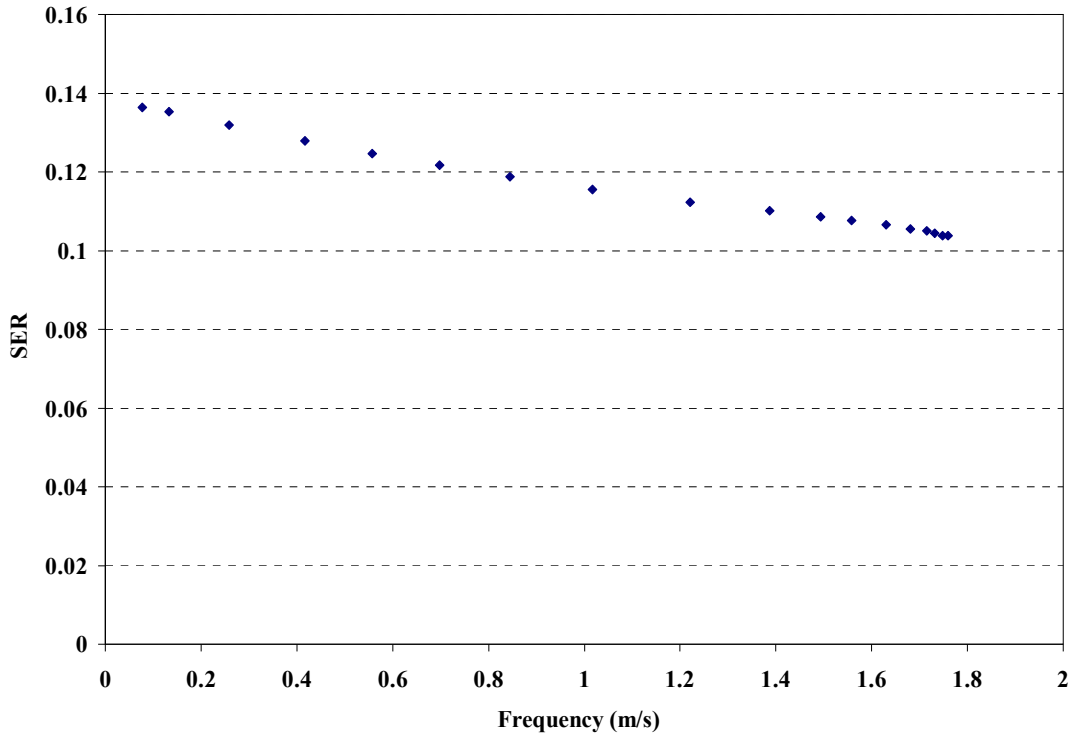


Figure 102: YSZ Strain Energy Ratio vs. Measured Velocity at L/2

The next relationship is between the loss factor, η , of the coating alone versus response velocity at the center of the beam. The value was determined using the equation:

$$\eta_{coat} = \frac{\eta_{sys}(SER+1) - \eta_{bare}}{SER} \quad (9)$$

It should be noted that this equation uses values calculated through pure experimental methods (η_{sys} and η_{bare}) and FE modeling methods (SER).

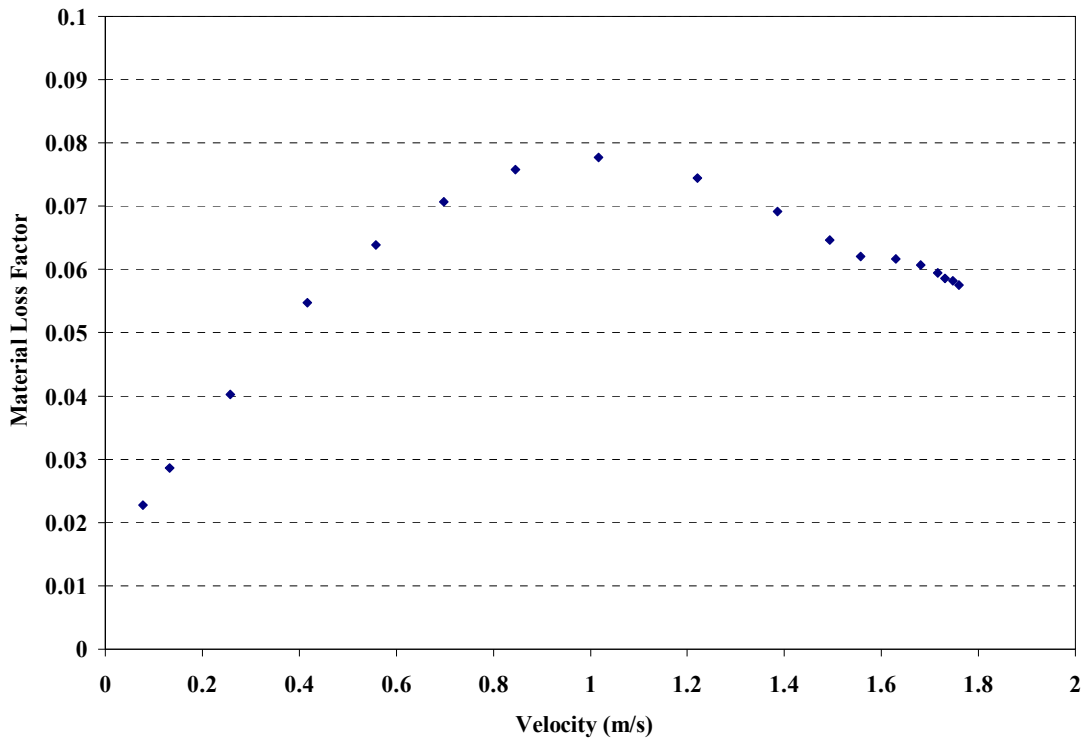


Figure 103: YSZ Coating Loss Factor in Response to Response Amplitude at L/2

The relationship presented in Figure 104 shows how the mode shape increases with increasing beam response at the center of the beam. This relationship will lead to a scaling factor which will be used to generate a relationship between normalized strain and actual strain.

Figure 105 shows the scaling factor that will relate the normalized reference strain to the actual strain used to show how the beam material properties vary with strain. This value was generated by using the relationship between the FE modeled mode shape and the calculated displacement.

$$\delta = \frac{V}{\omega} \tag{5}$$

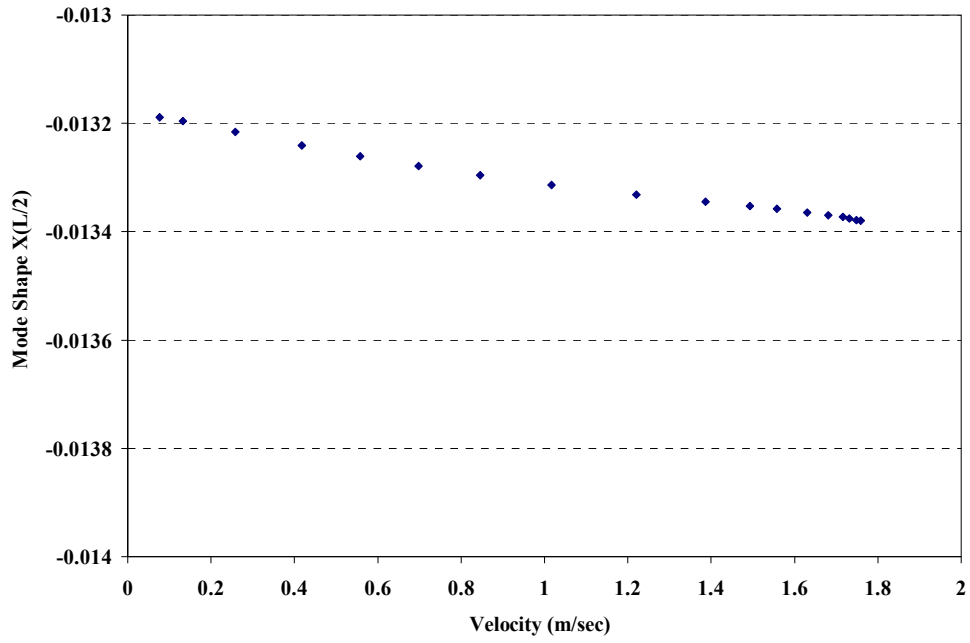


Figure 104: YSZ Mode Shape Response to Beam Response at L/2

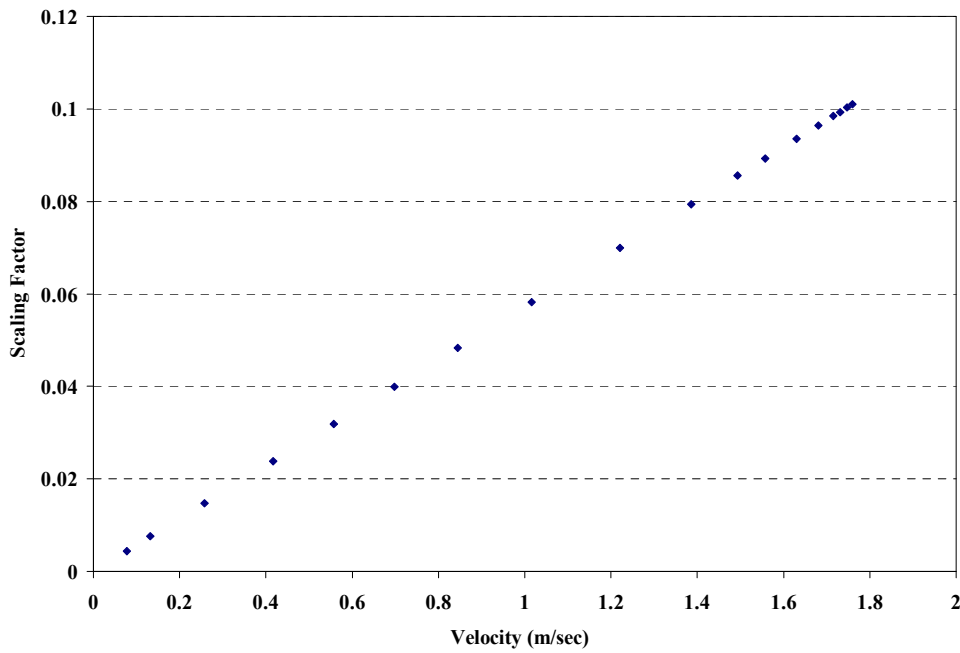


Figure 105: YSZ Scaling Factor

Figure 106 and Figure 107 show how the strain response of the beam increases as the beam responds to input with high velocities. Figure 107 is the final piece of the puzzle needed to relate the values of coating modulus, loss factor and loss modulus to physical strain. Now that each of the relationships has been generated the material properties of the coatings can be examined.

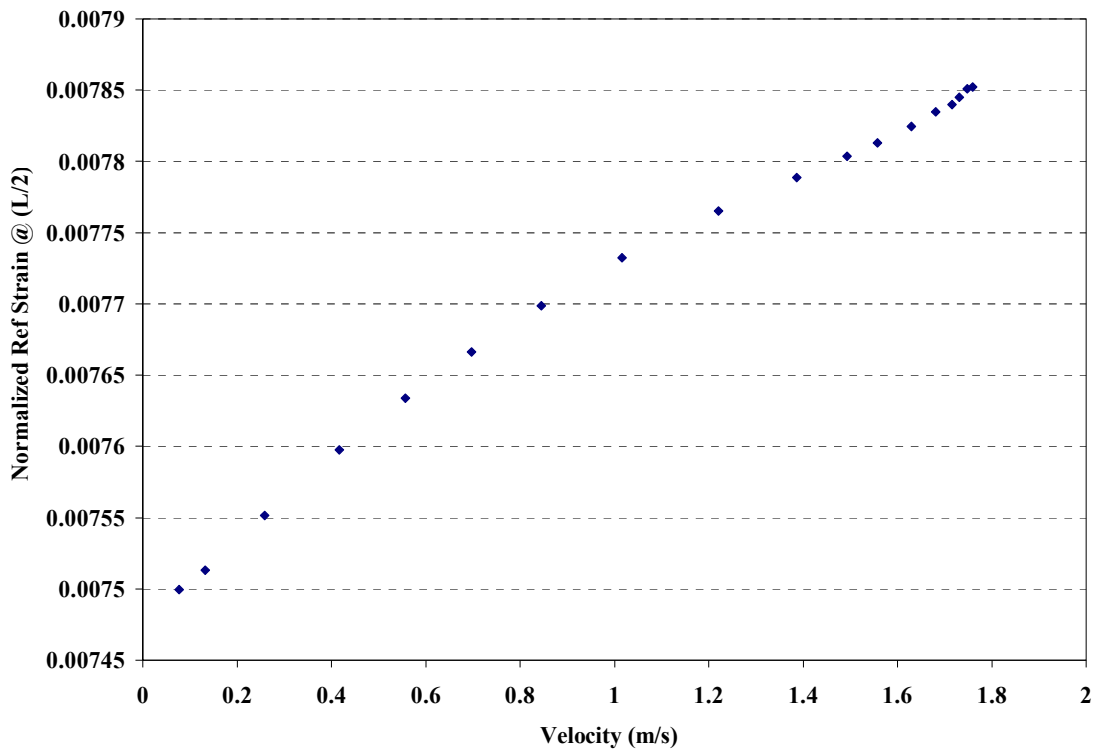


Figure 106: YSZ Normalized Reference Strain Response to L/2 Measured Velocity

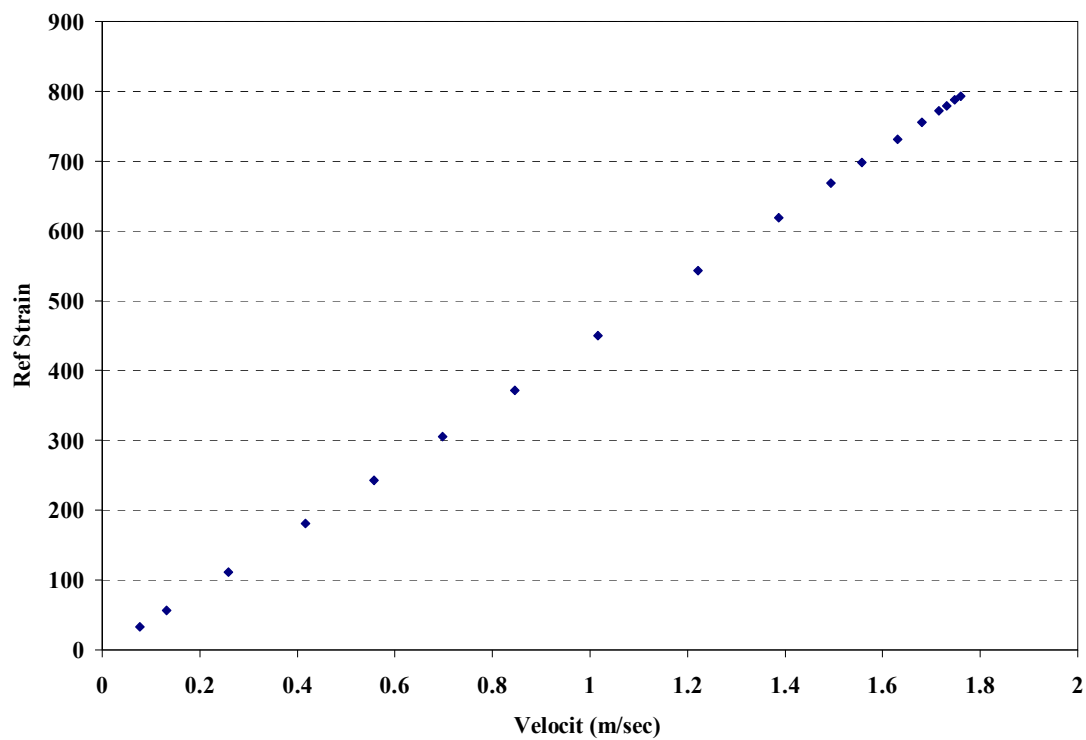


Figure 107: YSZ Reference Strain Response to L/2 Measured Velocity

Bibliography

- Allen, K. S. *Evaluation Techniques for Determining Damping Mechanisms on Titanium Plates*. MS Thesis, AFIT/GAE/ENY/05-M01. Graduate School of Engineering and Management, Air Force Institute of Technology (AU), Wright-Patterson AFB OH, March 2005 (ADA436467).
- Bajan, R., Froning, M., Reynolds, R., and Ruggiero, P. "The Art and Craft of Applying Thermal Barrier Coatings to Improve Life Expectancy," *Power Engineering*, 112(3): 64 (March 2008).
- Blackwell, C. M. *The Evaluation of the Damping Characteristics of a Hard Coating on Titanium*. MS Thesis, AFIT/GAE/ENY/04-M03. Graduate School of Engineering and Management, Air Force Institute of Technology (AU), Wright-Patterson AFB OH, March 2004 (ADA422952).
- Blackwell, C., Palazotto, A., George, T. J., and Cross, C. J. "The Evaluation of the Damping Characteristics of A Hard Coating on Titanium," *Shock & Vibration*, 14(1): 37-51 (2007).
- Carter, T. J. "Common Failures in Gas Turbine Blades," *Engineering Failure Analysis*, 12(2): 237-247 (2005).
- Coasack, T., Pawlowski, L., Schneiderbanger, S., and Sturlese, S. "Thermal Barrier Coatings on Turbine Blades by Plasma Spraying with Improved Cooling," *Journal of Engineering for Gas Turbines and Power*, 116(1): 272-276 (1994).
- Cowles, B. A. "High Cycle Fatigue in Aircraft Gas Turbines - An Industry Perspective," *International Journal of Fracture*, 80(2-3): 147-163 (1996).
- Cross, K. R., Lull, W. R., Newman, R. L., and Cavanagh J. R. "Potential of Graded Coatings in Vibration Damping," *Journal of Aircraft*, 10(11): 689-691 (1973).
- Garrison, B. et al. "High Cycle Fatigue (HCF) Science and Technology Program 2000 Annual Report." AFRL-PR-WP-TR-2001-2010, Wright Patterson Air Force Base, OH, 2001.
- Grady, J. E. "Fundamentals of High-Cycle Fatigue," *Machine Design*, 71(18): 86 (1999).

- Hoover, T. M. *An Electromagnetic Tool for Damping and Fatigue Analysis*. MS Thesis, AFIT/FSS/ENY/04-M04. Graduate School of Engineering and Management, Air Force Institute of Technology (AU), Wright-Patterson AFB OH, March 2004 (ADA426593).
- Inman, D. J. *Engineering Vibration 2nd Edition*. Upper Saddle River, NJ: Prentice Hall, 2001.
- Ivancic, F. T. *The Effect of A Hard Coating On the Damping and Fatigue Life of Titanium*. MS Thesis, AFIT/GAE/ENY/03-12. Graduate School of Engineering and Management, Air Force Institute of Technology (AU), Wright-Patterson AFB OH, March 2003 (ADA412854).
- Ivancic, F., and Palazotto, A. "Experimental Considerations for Determining the Damping Coefficients of Hard Coatings," *Journal of Aerospace Engineering*, 18(1): 8-17 (2005).
- Kroupa, F., & Plesek, J. "Nonlinear Elastic Behavior In Compression of Thermally Sprayed Materials," *Materials Science and Engineering A*, 328(1-2): 1-7 (2002).
- Lauwagie, T., Lambrinou, K., Patsias, S., Heylen, W., & Vleugels, J. "Resonant-Based Identification of the Elastic Properties of Layered Materials: Application to Air-Plasma Sprayed Thermal Barrier Coatings," *NDT & E International*, 41(2): 88-97 (2008).
- Lee, D. W. *Evaluation of Factors Contributing to Damping of Coated and Uncoated Titanium Plates*. MS Thesis AFIT/GAE/ENY/06-M06. Graduate School of Engineering and Management, Air Force Institute of Technology (AU), Wright-Patterson AFB OH, March 2006 (ADA449409).
- Limarga, A. M., Duong, T. L., Gregori, G., and Clarke, D. R. "High-Temperature Vibration Damping of Thermal Barrier Coating Materials," *Surface & Coatings Technology*, 202(4-7): 693-697 (2007).
- MatWeb Material Property Data*. Retrieved May 20, 2008, from <http://www.matweb.com/search/DataSheet.aspx?MatID=19320>
- Patsias, S., Tassini, N., and Stanway, R. "Hard Ceramic Coatings: An Experimental Study On A Novel Damping Treatment," *Smart Structures and Materials 2004, Damping and Isolation*, 5386(1): 174-84 (2004).
- Pawlowski, L., Didier, L., and Fauchais, P. "Structure-Thermal Properties-Relationship in Plasma Sprayed Zirconia Coatings," *Journal of Vacuum Science and Technology A: Vacuum, Surfaces, and Films*, 3(6): 2494-2500 (1985).

- Reed, Shad. A. *Development of Experimental, Analytical, and Numerical Approximations Appropriate for Nonlinear Damping Coatings*. Air Force Institute of Technology (AU), Wright-Patterson AFB OH, March 2007.
- Runyon, B. D., George, T., Cross, C., Drew, P., and Jones, K. "Automated Identification of Damping Material Properties," *6th AIAA Non-Deterministic Approaches Forum; 5th AIAA Gossamer Spacecraft Forum*. 4162-4169. 2004.
- Shipman, M., Patsias, S. "Hard Damping Coatings: Internal Friction as the Damping Mechanism," *8th National Turbine Engine High Cycle Fatigue (HCF) Conference*. Monterey, CA: (2003).
- Strangman, T. E. "Thermal Barrier Coatings for Turbine Airfoils," *Thin Solid Films*, 127(1-2): 93-105 (1985).
- Tassini, N., Lambrinou, K., Mircea, I., Bartsch, M., Patsias, S., and Van der Biest, O. "Study of the Amplitude-Dependent Mechanical Behaviour of Yttria-Stabilised Zirconia Thermal Barrier Coatings," *Journal of the European Ceramic Society*, 27(2-3): 1487-1491 (2007).
- Tassini, N., Lambrinou, K., Mircea, I., Patsias, S., Van Der Biest, O., and Stanway, R. "Comparison of the Damping and Stiffness Properties of 8wt% Yttria Stabilised Zirconia Ceramic Coating Deposited by the APS and EB-PVD Techniques," *Smart Structures and Materials 2005 - Damping and Isolation*, 5760: 109-117 (2005).
- Torvik, P. J. "Damping of Layered Materials," AIAA-1989-1422, 1989.
- Torvik, P. J. "Analysis of Free-Layer Damping Coatings," *Key Engineering Materials*, 333: 195-214 (2007).
- Torvik, P. J., Patsias, S., and Tomlinson, G. R. "Characterising the Damping Behaviour of Hard Coatings: Comparisons from Two Methodologies," *6th National Turbine Engine High Cycle Fatigue (HCF) Conference*. Jacksonville, FL: (2001).
- VibrationVIEW*(2007). (7.0.5 HFE ed.). Janison, MI: Vibration Research Corporation.

REPORT DOCUMENTATION PAGE			<i>Form Approved</i> OMB No. 0704-0188		
The public reporting burden for this collection of information is estimated to average 1 hour per response, including the time for reviewing instructions, searching existing data sources, gathering and maintaining the data needed, and completing and reviewing the collection of information. Send comments regarding this burden estimate or any other aspect of this collection of information, including suggestions for reducing this burden to Department of Defense, Washington Headquarters Services, Directorate for Information Operations and Reports (0704-0188), 1215 Jefferson Davis Highway, Suite 1204, Arlington, VA 22202-4302. Respondents should be aware that notwithstanding any other provision of law, no person shall be subject to any penalty for failing to comply with a collection of information if it does not display a currently valid OMB control number. PLEASE DO NOT RETURN YOUR FORM TO THE ABOVE ADDRESS.					
1. REPORT DATE (DD-MM-YYYY)		2. REPORT TYPE		3. DATES COVERED (From — To)	
19-06-2008		Master's Thesis		October 2006 — June 2008	
4. TITLE AND SUBTITLE Vibration Analysis of Commercial Thermal Barrier Coatings			5a. CONTRACT NUMBER		
			5b. GRANT NUMBER		
			5c. PROGRAM ELEMENT NUMBER		
6. AUTHOR(S) Pearson, Lindell E, Capt, USAF			5d. PROJECT NUMBER JON 08-216		
			5e. TASK NUMBER		
			5f. WORK UNIT NUMBER		
7. PERFORMING ORGANIZATION NAME(S) AND ADDRESS(ES) Air Force Institute of Technology Graduate School of Engineering and Management (AFIT/EN) 2950 Hobson Way WPAFB OH 45433-7765			8. PERFORMING ORGANIZATION REPORT NUMBER AFIT/GAE/ENY/08-J05		
			9. SPONSORING / MONITORING AGENCY NAME(S) AND ADDRESS(ES) Dr. Tommy George, AFRL/RZTS Building 252 Room 20 Wright-Patterson Air Force Base, Dayton, OH 45433-7251 986-5531		
			11. SPONSOR/MONITOR'S REPORT NUMBER(S)		
12. DISTRIBUTION / AVAILABILITY STATEMENT APPROVED FOR PUBLIC RELEASE; DISTRIBUTION UNLIMITED					
13. SUPPLEMENTARY NOTES					
14. ABSTRACT Thermal barrier coatings (TBCs) are currently used in turbine engine components to protect substrate material from exposure to high temperature and corrosion. These coatings have the potential to reduce stress in critical engine parts which could increase the life cycle of these parts. The fact that these coatings are already qualified for use in turbine engines makes it worth investigating their damping properties. The problem with TBCs is that they are difficult to characterize as they display nonlinear properties. This research utilizes an experimental and finite element procedure to characterize these coatings. A scanning electron microscope (SEM) was employed to observe the microstructure contribution to the damping properties. This program utilizes a testing method which employs a test setup that attempts to eliminate any external factors which may add any unwanted damping. The major contributions of this research are: a comparison of the material properties of two different TBCs, magnesium aluminate spinel and yttria stabilized zirconia; the confirmation that sweep rate does not cause data recorded in the log decrement method to coincide with data recorded with the half-power bandwidth method; and SEM images that confirm the damping properties of plasma sprayed TBCs are directly related to the microcrack structure of a coating.					
15. SUBJECT TERMS Vibration, Scanning Electron Microscopy, Ceramic Coatings, Plasma Spraying, Nonlinear Systems					
16. SECURITY CLASSIFICATION OF:			17. LIMITATION OF ABSTRACT	18. NUMBER OF PAGES	19a. NAME OF RESPONSIBLE PERSON
a. REPORT	b. ABSTRACT	c. THIS PAGE			Dr. Anthony Palazotto, ENY
U	U	U	UU	171	19b. TELEPHONE NUMBER (Include Area Code) (937) 255-3636 x4599 Anthony.palazotto@afit.edu